

**A MECHANISTIC-EMPIRICAL MODEL FOR PREDICTING TOP-DOWN
CRACKING IN ASPHALT PAVEMENTS**

A Dissertation

by

MENG LING

Submitted to the Office of Graduate and Professional Studies of
Texas A&M University
in partial fulfillment of the requirements for the degree of

DOCTOR OF PHILOSOPHY

Chair of Committee,	Robert L. Lytton
Committee Members,	Dallas N. Little
	Jon A. Epps
	Theofanis Strouboulis
Head of Department,	Robin Autenrieth

August 2017

Major Subject: Civil Engineering

Copyright 2017 Meng Ling

ABSTRACT

Top-down cracking (TDC) is a major distress mode in asphalt pavements. It initiates from or near the pavement surface then propagates downward through the asphalt layer and is usually observed as the form of longitudinal cracking in the pavement wheelpath. Due to its complexity, few mechanical-based systematic models are available to accurately evaluate the TDC performance and the efforts for the calibration and validation using a large number of field data are missing. To fill these research gaps and improve the understanding of TDC, the main objective of this study is to develop a calibrated and validated mechanistic-empirical model to characterize TDC in asphalt pavement layers.

Based on literature review, important factors contributed to the initiation and propagation of TDC are identified. One is non-uniform oxidative aging of the asphalt binders. The surface of the asphalt layer becomes stiffer and more brittle after field aging so that the crack is more prone to initiate at the pavement surface. Direct tension test is selected to analysis the modulus gradient of the field-aged asphalt mixtures. The long-term aging property also needs to be well determined. It is known that the long-term aging has a significant impact on the viscoelastic, healing, fracture and thermal properties of the asphalt mixtures. Two aging shift functions for the dynamic modulus are developed to quantify the effects of the long-term aging and non-uniform aging of in-situ asphalt pavements, respectively.

A TDC initiation model is developed using continuum damage and fracture mechanics with field observations including local traffic, material properties, pavement structures and TDC initiation time. A three dimensional finite element model (FEM) and artificial neural network (ANN) models are developed to calculate J -integral (energy release rate) in the crack propagation phase. A preliminary endurance limit model is proposed based on the viscoelastic Griffith crack initiation criterion. A total of 80% and 20% of pavement sections are randomly selected for the calibration and validation purposes, respectively. Finally, this TDC model is coded in C# computer language as a stand-alone program to predict the initiation time and fatigue life of TDC. It can also be utilized as a subroutine in the AASHTOware Pavement Mechanistic-Empirical (ME) Design.

DEDICATION

To my parents for their love, support and encouragement

ACKNOWLEDGEMENTS

I would like to express my deepest gratitude to my advisor and committee chair, Dr. Robert L. Lytton, for his constant support, guidance, knowledge, patient and encouragement throughout my graduate study. Dr. Lytton is such a great advisor, without him, I would never have realized my academic potential. I also want to thank Dr. Bjorn Birgisson and committee members for their guidance and support of this research.

Special thanks to all of the Research Team members and Researchers from Texas A&M Transportation Institute who helped me and shared their knowledge, friendship and encouragement with me. Thanks also go to my friends and the Civil Engineering Department faculty and staff for making my time at Texas A&M University a great experience. Finally, thanks to my parents for their encouragement, knowledge, patience and love.

CONTRIBUTORS AND FUNDING SOURCES

Contributors

Part 1, faculty committee recognition

This work was supervised by a dissertation committee consisting of Professors Robert Lytton, Dallas Little, Jon Epps of the Department of Civil Engineering and Professor Theofanis Strouboulis of the Department of Aerospace Engineering.

Part 2, collaborator contributions

The work for the dissertation was completed by the author, in collaboration with Drs. Xue Luo and Sheng Hu of the Texas A&M Transportation Institute and Dr. Fan Gu of the National Center for Asphalt Technology under the advisement of Dr. Robert Lytton of the Department of Civil Engineering.

Funding Sources

This work was made possible by the National Cooperative Highway Research Program (NCHRP) under Project Number 01-52. Its contents are solely the responsibility of the author and do not necessarily represent the official views of the Transportation Research Board.

NOMENCLATURE

AASHTO	American Association of State Highway and Transportation Officials
BUC	Bottom-Up Cracking
DPSE	Dissipated Pseudo Strain Energy
FWD	Falling Weight Deflectometer
LTPP	Long-Term Pavement Performance
MEPDG	Mechanistic-Empirical Pavement Design Guide
NCHRP	National Cooperative Highway Research Program
NMAS	Nominal Maximum Aggregate Size
TDC	Top-Down Cracking
TxDOT	Texas Department of Transportation
X-ray CT	X-ray Computed Tomography

TABLE OF CONTENTS

	Page
ABSTRACT	ii
DEDICATION	iv
ACKNOWLEDGEMENTS	v
CONTRIBUTORS AND FUNDING SOURCES.....	vi
NOMENCLATURE.....	vii
TABLE OF CONTENTS	viii
LIST OF FIGURES.....	xii
LIST OF TABLES	xvi
1. INTRODUCTION	1
1.1 Background of Top-Down Cracking.....	1
1.2 Problem in Characterization of TDC in Asphalt Pavements.....	5
1.3 Research Objectives	9
1.4 Dissertation Outline.....	10
2. AN INVERSE APPROACH TO DETERMINE COMPLEX MODULUS GRADIENT OF FIELD-AGED ASPHALT MIXTURES.....	12
2.1 Overview	12
2.2 Introduction	13
2.3 Direct Tension Test to Measure Modulus Gradient	15
2.3.1 Asphalt Field Cores and LMLC Mixtures.....	15
2.3.2 Direct Tension Test	18
2.3.3 Mechanical Responses of Field Cores and LMLC Mixtures	19

2.4	Derivations of Complex Modulus Gradient	25
2.4.1	Inverse Application of Viscoelastic-Elastic Correspondence Principle	25
2.4.2	Determination of Modulus Gradient Parameters	28
2.4.3	Determination of Complex Modulus Using Approximated n and k	31
2.4.4	Determination of Complex Modulus Using Complex n and k	36
2.4.5	Determination of Relaxation Modulus, Reference Modulus and Modulus Gradient	37
2.5	Conclusions	42
3.	TIME-TEMPERATURE-AGING-DEPTH SHIFT FUNCTIONS FOR DYNAMIC MODULUS MASTER CURVES OF ASPHALT MIXTURES	43
3.1	Overview	43
3.2	Introduction	44
3.3	Laboratory Testing Method and Results	47
3.3.1	Material and Mix Design.....	47
3.3.2	Direct Tension Test	48
3.3.3	Tensile Creep Test.....	51
3.3.4	Test Results	51
3.4	Construction of Dynamic Modulus Master Curve for LMLC Mixtures	53
3.4.1	Determination of Aging Shift Function	56
3.4.2	Vertical Shift and Rotation.....	57
3.4.3	Determination of Horizontal Aging Shift Factor	60
3.4.4	Application of Aging Shift Function.....	63
3.5	Construction of Dynamic Modulus Master Curve of Field Cores	65
3.5.1	Implementation of Aging Shift Function	66
3.5.2	Determination of Horizontal Depth Shift Function.....	69
3.6	Conclusions	72

4.	NUMERICAL MODELING AND ARTIFICIAL NEURAL NETWORK FOR PREDICTING J-INTEGRAL OF TOP-DOWN CRACKING IN ASPHALT PAVEMENT.....	74
4.1	Overview	74
4.2	Introduction	75
4.3	Three-Dimensional Finite Element Modeling of TDC	78
4.3.1	Material Properties of Pavement System	79
4.3.2	Tire-Pavement Contact Stresses.....	80
4.3.3	Pavement Structure, Mesh and Boundary Conditions	84
4.3.4	Numerical Simulation Results.....	87
4.4	Artificial Neural Network Modeling Of J-Integral	90
4.4.1	Background and Preparation of ANN	90
4.4.2	Development and Algorithm of ANN.....	91
4.5	Conclusions	97
5.	DEVELOPMENT OF A CALIBTATED AND VALIDATED MECHANISTIC- EMPERICAL TOP-DOWN CRACKING MODEL.....	99
5.1	Background	99
5.2	LTPP Data Collection	99
5.2.1	Pavement Material and Structure Data.....	101
5.2.2	Characterization of Traffic Loads	102
5.2.3	Characterization of Field Distress Data	113
5.3	Materials Properties of Pavement Layers.....	116
5.3.1	Asphalt Layer	116
5.3.2	Base and Subgrade Layers	119
5.4	Modeling of Crack Initiation and Propagation of TDC	120
5.4.1	TDC Initiation Model.....	120
5.4.2	TDC Propagation Model	126
5.4.3	Thermal-induced Damage Model.....	127
5.4.4	Calibration and Validation of TDC Propagation Model	130
5.5	Endurance Limit Prediction of Asphalt Pavement Layers	131
5.6	Black Space Diagram for Asphalt Mixtures	139

5.7	Development of C# Computer-Aided Program for TDC.....	145
6.	SUMMARIES, CONCLUSIONS AND RECOMMENDATIONS	155
6.1	Summaries and Conclusions	155
6.2	Recommendations	158
	REFERENCES.....	160
	APPENDIX A	167
	APPENDIX B.....	172
	APPENDIX C.....	175

LIST OF FIGURES

	Page
Figure 1.1 Typical Top-Down Crack in Field Core (after Pavement Interactive 2012)	2
Figure 2.1 Field Core Specimen Preparation	17
Figure 2.2 Field Core Specimen and Setup of Direct Tension Test: (a) Specimen with LVDTs, (b) Specimen in the MTS.....	18
Figure 2.3 Three Repeated Test Results at 10°C, (a) Load in Three Repeated Tests, (b) Top and Bottom Strains in Three Repeated Tests.....	19
Figure 2.4 Monotonic Loads in Direct Tension Test: (a) Loads at Different Temperatures, (b) Loads at Different Aging Times.....	21
Figure 2.5 Measured Vertical and Horizontal Strains at Top of Field Core Specimen ...	22
Figure 2.6 Measured Vertical Strains at Top, Center, and Bottom of Tested Specimen: (a) Strain at Different Depths of Field Core Specimen, (b) Strain of Laboratory Fabricated Specimen, (c) Strain at Different Aging Times of Field Core Specimen.....	23
Figure 2.7 Illustration of Non-Uniform Distributions of Stress, Strain, and Modulus in Field Core Specimen.....	24
Figure 2.8 Calculated Dynamic Modulus of a Field Core Specimen at Three Temperatures.....	36
Figure 2.9 Dynamic Modulus Master Curve of a Field Core Specimen.....	38
Figure 2.10 Relaxation Modulus Determined from the Dynamic Modulus Master Curve	39
Figure 2.11 Measured Strain at the Bottom of a Field Core Specimen and Associated Pseudo Strains at Different Iterations	41
Figure 2.12 Modulus Gradients of 8 and 22 Months Aged Field Specimens at Three Temperatures and 0.1 Hz	41

Figure 3.1 Preparation of Test Specimen: (a) Original Field Core, (b) Cut and Trimmed Specimen	49
Figure 3.2 Specimen Gluing Jig.....	50
Figure 3.3 Dynamic Modulus at Different Conditions: (a) Different Depths, (b) Different Aging Times, (c) Different Temperatures	52
Figure 3.4 Dynamic Modulus Master Curve: (a) 4% Air Void Content, (b) 7% Air Void Content.....	55
Figure 3.5 Vertical Shift and Rotation Process: (a) Fitted Aging Parameters, (b) Modified and Original 6 months Master Curves, (c) Original and Modified Master Curves	59
Figure 3.6 Final Aging Dynamic Modulus Master Curve	62
Figure 3.7 Modified Master Curves and Original Master Curve	64
Figure 3.8 Final Single Master Curve after Shift.....	65
Figure 3.9 Bottom Dynamic Modulus Master Curve for HMA Field Cores	66
Figure 3.10 Development of Aging Master Curve for Field Mixtures: (a) Aging Parameter Ratios for FHMA, (b) Horizontal Shift Factors Versus Aging Time, (c) Bottom Aging Master Curve of Field Asphalt Mixtures, (d) Aging Master Curves for Top, Center and Bottom.....	67
Figure 3.11 Application of Depth Shift Function to Top and Center: (a) Vertical Shift and Rotation, (b) Horizontal Depth Shift.....	71
Figure 4.1 Modulus Gradient Curves in Asphalt Layers: (a) Aging, (b) Temperature....	80
Figure 4.2 Simplified Patterns of 3D Vertical, Longitudinal and Transverse Contact Stresses.....	81
Figure 4.3 Three Components of Tire-Pavement Contact Stress in ABAQUS: (a) Vertical Contact Stress, (b) Transverse Contact Stress, (c) Longitudinal Contact Stress, (d) Combination of Contact Stresses	83
Figure 4.4 3D FEM Model and Mesh Details for TDC and Loading: (a) 3D FE Pavement Model, (b) Magnified Mesh View of Crack Front, (c) Meshes in Crack and Loading Areas.....	86

Figure 4.5 J-integral in Pavement Depth with Various Values of n, k and Asphalt Layer Thickness: (a) Different n, (b) Different k, (c) Different Asphalt Layer Thickness	89
Figure 4.6 Structure of Artificial Neural Network	91
Figure 4.7 Measured and Predicted J-integral for Training, Validation, and Overall Datasets for Dual and Single Tire Loadings: (a) Dual Tire Length of 19 mm, (b) Dual Tire Length of 185 mm, (c) Dual Tire Length of 229 mm, (d) Single Tire Length of 64 mm, (e) Single Tire Length of 305 mm, (f) Single Tire Length of 406 mm	94
Figure 5.1 LTPP Sections in Four Climate Zones	100
Figure 5.2 FHWA Vehicle Category Classification (FHWA 2013)	103
Figure 5.3 Single Axle Load Distribution for Category One	106
Figure 5.4 Single Axle Load Distribution for Category Two	106
Figure 5.5 Cumulative Axle Load Distribution vs Tire Length: (a) Category One, (b) Category Two	111
Figure 5.6 Example of Crack Length versus Service Time	116
Figure 5.7 Air Void Distribution in Pavement Depth	118
Figure 5.8 Evolution of Modulus Gradient in Asphalt Layer	119
Figure 5.9 Schematic Plot of Thermal Cracking in FEM	130
Figure 5.10 Concept of Endurance Limit (after Pavement Interactive 2012)	132
Figure 5.11 Stress and Strain versus Time	133
Figure 5.12 Stress-Strain Curve	133
Figure 5.13 Measured Stress versus Pseudo Strain	135
Figure 5.14 Energy Released Zone in Infinite Plate (after Anderson 2005)	137
Figure 5.15 Plastic Zone at the Crack Tip (after Anderson 2005)	137

Figure 5.16 Example of Black Space diagram with Glover-Rowe Parameter (after Bennert 2014).....	140
Figure 5.17 Example of Black Space Diagram with R Curve (after King et al. 2012)..	140
Figure 5.18 Mixture Aging Viscoelastic Properties in Black Space Diagram.....	141
Figure 5.19 Black Space Diagram for Cracking Initiation.....	144
Figure 5.20 Tensile and Compressive Dynamic Modulus	145
Figure 5.21 Interface of Computer Program	146
Figure 5.22 Interface of General Information	147
Figure 5.23 Interface of Traffic Load: (a) AADTT Input, (b) Load Spectra Input.....	148
Figure 5.24 Interface of Weather Station Selection	150
Figure 5.25 Interface of Structure and Material Properties.....	151
Figure 5.26 Interface of Asphalt Material Properties.....	152
Figure 5.27 Monthly Modulus Values for Level One.....	153
Figure 5.28 Typical Modulus Value for Level Two	154

LIST OF TABLES

	Page
Table 2.1 Field Cores and Laboratory Fabricated Mixtures Specimens Tested in Direct Tension Test.....	17
Table 2.2 Results of Calculations of Modulus Gradient of a Field Core Specimen (8 Months Aged at 30°C) from Direct Tension Test	31
Table 3.1 Calculated CAM Model Parameters	55
Table 3.2 Specimens with Different Aging Conditions	63
Table 3.3 CAM Model Parameters	63
Table 4.1 Regression Analysis of Tire-Pavement Contact Stress.....	82
Table 4.2 Materials and Structures Inputs in the FEM	85
Table 5.1 Characteristics of LTPP Axle Type	104
Table 5.2 Example of Single Axle Load Distribution.....	104
Table 5.3 Categories of Vehicle Classes.....	107
Table 5.4 Load Interval of Traffic loading Types.....	108
Table 5.5 Tire Lengths for Each Traffic Category.....	110
Table 5.6 Distribution of Vehicle Classes.....	112
Table 5.7 Average Number of Axle for Each Vehicle Class	113
Table 5.8 Crack Width to Crack Depth Ratio (Kumara et al. 2004).....	115

1. INTRODUCTION

1.1 Background of Top-Down Cracking

Top-down cracking (TDC) is known as one of the major distress types in asphalt pavements, and it has gained tremendous attention in decades globally (Gerritsen et al. 1987; Matsuno and Nishizawa 1992; Roque et al. 2004). Different from bottom-up cracking (BUC), TDC initiates from or near the pavement surface and then propagates downward through the asphalt layer, which is usually observed as the longitudinal crack in or near the wheelpaths. The TDC in an associated field core is exhibited from different angles of view in Figures 1.1 (a) and (b), respectively (Pavement Interactive 2012).

It is known that the current pavement analysis for the BUC performance is not capable of characterizing the initiation and propagation phases of TDC because of different mechanisms between these two distress modes. For example, the traditional method normally assumes a uniform tire contact stress and a single value of the asphalt layer modulus, then calculates the tensile strain at the bottom of the asphalt layer to predict the initiation of BUC and the corresponding fatigue life. However, this theory cannot be applied to explain the mechanisms of TDC. Even though the TDC has been studied for decades, there are few systematic models that have been developed and no general agreement has been reached due to its complexity mainly from the material, climate, traffic and structure factors.



(a)



(b)

Figure 1.1 Typical Top-Down Crack in Field Core (after Pavement Interactive 2012)

It has been shown that TDC is mainly affected by several factors from the previous research studies. A complex state of high tensile or shear stresses induced by the traffic loading at the edge of or within the tire patch are acknowledged as one important factor (Ozer et al. 2011; Wang et al. 2013). Specifically, when a moving traffic load is applied on the pavement surface, the contact stress can be decomposed into a vertical stress, transverse stress and longitudinal stress, and they are non-uniformly distributed. The modulus gradient in the asphalt layer due to oxidative aging is another factor. After the field aging, the surface of asphalt layer has a higher modulus but a lower fracture energy and relaxation property. Accordingly, it becomes more brittle and susceptible to surface cracking. The effect of aging on the crack initiation is also discussed in the endurance limit

calculation, which can be clearly illustrated in the black space diagram. The aging effect is widely accepted as one of the key factors (Pellinen et al. 2004; Roque et al. 2010). In addition, the distribution of air void content in the asphalt layer normally follows a C-shape curve, this indicates that the highest air void content is at the surface of the pavement. The air voids are the initial damage of the asphalt mixtures, which means more possibility that the crack initiates at the surface of the asphalt layer. On the other hand, it is reported that in high temperature areas with high pavement surface temperatures, the modulus of the asphalt layers even increase within the pavement depth (Archilla 2015). The author believes that the inverse modulus gradient also contributes to the initiation of TDC since the tensile and shear strains at the pavement surface increase as the temperature increases. The thermal stress is recognized as another important factor to the surface cracks. In addition, material properties in other pavement layers and the pavement structure are also considered as vital factors (Baladi et al. 2003; Svasdisant et al. 2002). It indicates that the thicknesses of asphalt and base layers and the moduli of base and subgrade layers are the dominant structural and material factors.

In summary, the essential factors for the initiation and propagation of TDC in asphalt layers are as follows:

- Materials: Mixture Composition, Modulus Variation, Air Void Distribution, Healing Properties, Fracture Properties, Thermal Properties.
- Structure: Layer Thickness, Stabilized/Unstabilized Base Course.
- Traffic: Load Mechanism, Load Magnitude and Distribution, Load Spectrum.
- Environment: Temperature Gradient, Oxidative Aging, Thermal Stress.

It is clear that a single factor is not capable of characterizing the TDC. Therefore, multiple corresponding sub-models are developed and it is desirable to consider the combinations and interactions of these factors simultaneously in determining the initiation and propagation of TDC in the pavement structure level and finally forms a systematic TDC model.

In the current version of the AASHTOware Pavement Mechanistic-Empirical (ME) Design, a transfer function was proposed to predict the initiation and fatigue life of TDC, which is similar to the one used to predict the BUC performance. The fatigue life is estimated to be a function of surface tensile strain and the modulus of the asphalt layer with three coefficients (K_1 , K_2 and K_3). In the NCHRP Project 01-42A, the dissipated creep strain energy (DCSE) model and viscoelastic continuum damage (VECD) model were developed to analyze the initiation and propagation phases of TDC, respectively. However, it should be mentioned that the models developed in the NCHRP 01-42A is not well calibrated using the field data. Meanwhile, there are some other potential issues needed to be addressed. For example, this model did not take into account the field aging process of asphalt mixtures, including the non-uniform field aging and long-term field aging. Only the Global Aging System (GAS) model and some empirical equations relating the aged binder viscosity to the change of modulus were used to simulate the oxidative aging effect on the dynamic modulus of field-aged asphalt mixtures. Traffic was characterized using the equivalent single axle loads (ESALs), but the load spectra and non-uniform contact stress were not taken into account. The program was also not compatible with the current format of the AASHTOware Pavement ME Design. The

location of TDC was assumed to be at a distance away from the wheelpath, which seems inconsistent with the field observations, especially for the asphalt pavements with relatively thick asphalt surface layers. Meanwhile, the endurance limit of the asphalt mixtures was not well determined, which is an important concept in the long lasting or perpetual pavement, especially in evaluating the fracture resistance of the asphalt mixtures with aging and low temperature.

As a result, there is a need to develop an effective mechanistic-empirical model to predict the initiation and propagation of TDC, and it should be well calibrated and validated by the field performance for different climatic zones and pavement structures. Furthermore, the model developed in this study should be able to be incorporated into the AASHTOware pavement ME design.

1.2 Problem in Characterization of TDC in Asphalt Pavements

It is well-known that aging is one of the environmental factors that significantly changes the properties of asphalt mixtures and pavement performance. For asphalt pavements, there are two aging stages called the short-term aging and long-term aging (Mirza and Witczak 1995). The short-term aging of asphalt mixtures occurs during the procedures of mixing, compaction and lay down. In this stage, the aging effect can be assumed to be identical from the surface to the bottom of the asphalt layer since the chemical reaction between oxygen and asphalt binders is almost uniform. After construction, the oxygen in the atmosphere first reacts with the surface then slowly diffuses inside the asphalt layer through the connected air voids. Therefore, the aging rate

at the pavement surface is higher than that at other deeper layers, and it becomes even severer for an asphalt pavement with a higher air void content. Hence, unlike the short-term aging, the long-term field aging induces the surface of the pavement stiff faster than other asphalt layer depths. As a result, the modulus gradient in the asphalt pavement is developed, which is an important characteristic of the field asphalt mixtures.

In order to take into account the field aging of asphalt mixtures in the pavement design, considerable research efforts have been made to either simulate or analyze the field aging in the laboratory, in the binder level and mixture level, or extract the binders using the chemical solvent from the field cores then determine the complex shear modulus and phase angle of the aged binders. One of the popular methods is the AASHTO R30 aging procedure (AASHTO 2006). However, it has been questioned to be too moderate, which cannot be used to reflect the actual field aging. Meanwhile, in order to simulate aging in a rational way, it is suggested that for different types of asphalt mixtures such as the mixtures with unmodified and modified binders, different aging protocols need to be developed to reach the same aging level. In addition, the complicated non-uniform aging of asphalt mixtures is even more difficult to be simulated. In the binder extraction method, the viscosity is determined from the extracted aged binders at different pavement depths of the field cores, so the viscosity gradient with the pavement depth and aging time can be obtained. However, there is one main problem with this method: some important effects such as the air void distribution, aggregate gradation, binder absorption, and aggregate-binder interaction on the modulus of the asphalt mixtures are ignored.

Therefore, it is desired to obtain the material properties of the field cores in the intact state. It is known that conducting mechanical tests on the field cores remains difficult mainly due to the geometry compared to the LMLC mixtures specimens. The typical issue is the required dimension (100 mm in diameter and 150 mm in height) for a specimen in the dynamic modulus test. Compared to the laboratory specimen, the thickness of field cores is normally insufficient to be used in the standard dynamic modulus test. To overcome this issue, recent studies determine that the thickness for both of the rectangular and cylindrical field core specimens can be as thin as 26 mm for the dynamic modulus test and fatigue test. The test results are almost identical to the specimens with a standard dimension using the Asphalt Mixture Performance Tester (AMPT) if attention is paid to the nominal maximum aggregate size (NMAS) to ensure the size of the small specimen is still a representative volume (Kutay et al. 2009). This valuable finding confirms that it is theoretically possible to accurately analyze those with small specimen geometries such as the field cores. In the previous studies, the small tested specimens are sliced from different depths of one cylindrical field core, which are used to determine the non-uniform modulus distribution within the pavement depth. The widely-used uniaxial tension-compression test is then conducted at different temperatures and frequencies to obtain the dynamic modulus master curve of each slice using the AMPT. However, it should be mentioned that aging is most severe in the top surface especially the top 13 mm (NCHRP 2004; Farrar et al. 2006). The methods mentioned above are actually to measure the average modulus of each slice, which may not be able to capture the most severe gradient feature at top 13 mm.

The long-term aging is also another important aging characteristic of asphalt mixtures. One widely used method to quantify the long-term aging is to conduct the aging simulation tests on asphalt mixtures first, and then use the mechanical tests such as relaxation modulus and dynamic modulus tests to evaluate the change of viscoelastic properties of the mixtures at different aging periods. However, at the current stage, a single master curve could not be constructed to include the effects of both loading time and aging time. The available methods including the aging time are to use a master curve equation, for example, using the sigmoidal model to construct the relaxation modulus or dynamic modulus master curve at each aging time. However, it should be mentioned that the coefficients of the model at different ages are empirically related to the aging times in this method, and they do not have the physical significance, the implementation of this method is also limited. As a result, it is important to develop an aging model with aging shift factors to facilitate the construction the dynamic modulus master curve including the effects of temperature, loading time and aging time, which can also be used to predict the dynamic modulus master curve of the asphalt mixtures after long-term aging.

The TDC initiation time is one important index for the pavement performance. In the “crack initiation” phase, it should be emphasized that cracks already initiate at the first loading cycle. The air voids are the initial damage in the asphalt mixtures. Multiple micro-cracks initiated from the air voids are then coalesce into a visible crack (macro-crack). The size of micro-cracks increase and the number of cracks decreases after a number of loading cycles. The process continues until a visible crack is developed. For an asphalt

pavement, the crack initiation period is defined as the duration between the construction time and the first observed time of a longitudinal wheelpath cracking.

In both of the NCHRP Projects 1-42A and 1-37A, calibration and validation were conducted with limited field performance data, and it is not ready or intended for immediate use in the AASHTOware Pavement ME Design. In order to be incorporated in the Pavement ME Design, the forms of traffic, weather, pavement structure and layers material properties should be identical to those in the Pavement ME Design. Meanwhile, the pavement data such as the longitudinal cracking lengths at different severity levels, pavement structure, layers property, and traffic data are needed to be collected for the purposes of calibration and validation. During the calibration and validation process, a user-oriented computational software needs to be developed to be incorporated in the AASHTOware pavement ME design.

1.3 Research Objectives

The targets of this dissertation are to address the aforementioned shortcomings and develop a calibrated and validated mechanistic-empirical model for characterizing TDC in asphalt pavement layers. Another purpose is to help pavement engineers and practitioners better understand the mechanisms of TDC and further mitigate this type of distress. The focus of this dissertation mainly includes:

- Develop an efficient test protocol for determining the aging viscoelastic properties of field-aged mixtures such as complex modulus and complex Poisson's ratio;

- Develop a novel method to evaluate and predict the non-uniform aging and long-term aging viscoelastic properties of the laboratory-aged and field-aged asphalt mixtures;
- Develop FEM and ANN models to estimate the fracture parameter of TDC including the effects of different material properties of pavement layers, pavement structures, crack depths, and traffic loading levels; and
- Develop a calibrated and validated mechanistic-empirical model to predict the initiation and propagation of TDC in the asphalt pavements, based on the LTPP data, continuum damage and fracture mechanics approach. A new model is also proposed to determine the endurance limit of the asphalt mixtures and define the “crack initiation line” in the black space diagram.

1.4 Dissertation Outline

This dissertation is organized as follows:

Chapter 1 is an introduction of the background, problem statement, research objectives and dissertation outline.

Chapter 2 first introduces the current issues in determining the viscoelastic properties of the field-aged asphalt mixtures. A new method is then proposed using a mechanical approach to analyze the measured data and then compute the complex modulus gradient and Poisson’ ratio of the field-aged mixtures.

Based on the results from Chapter 2, two aging shift functions are developed in Chapter 3 to characterize the aging viscoelastic properties of asphalt mixtures, which are

used to predict the dynamic modulus master curves of asphalt layer after field aging including long-term aging and non-uniform aging.

Chapter 4 details the FEM and ANN models to predict the fracture parameter J -integral of the asphalt mixtures with various aging and temperature gradients, material properties, pavement structures, crack depths, and traffic levels.

A calibrated and validated mechanistic-empirical model is developed and presented in Chapter 5. In order to develop and calibrate the TDC initiation and propagation models, LTPP data are collected for a numerous pavement sections from different climatic zones. With the aid of the fracture mechanics, numerical models, ANN models and LTPP data, the generalized TDC prediction model is developed, calibrated and validated, which is capable of modeling both the initiation and propagation phases of TDC in asphalt pavements. Furthermore, a new endurance limit model is proposed then utilized in the black space diagram to rank the fracture resistance of asphalt mixtures with aging and low temperature, which helps facilitate in determining the initiation of TDC in asphalt pavements with the two environmental effects.

Chapter 6 summarizes the findings and conclusions of this dissertation. Recommendations for future studies are also presented in Chapter 6.

Appendixes A, B and C are attached at the end of the dissertation.

2. AN INVERSE APPROACH TO DETERMINE COMPLEX MODULUS GRADIENT OF FIELD-AGED ASPHALT MIXTURES*

2.1 Overview

This chapter develops a new mechanical-based method to determine the complex modulus and modulus gradient of field-aged asphalt mixtures using the direct tension test. Due to the non-uniform aging nature of the field cores, the mechanical responses must be measured at different depths. Meanwhile, the monotonic load is not applied at the neutral axis of the field core specimen due to the modulus gradient, the tensile part of the strain is used and should be separated from the measurement because of the eccentric loading. The modulus gradient parameters, the location of the neutral axis, and the stress distribution are first obtained using the elastic formulas for a series of loading times. Then the complex modulus is determined using the Laplace transform and the elastic-viscoelastic correspondence principle. An inverse approach and iteration are then proposed by using the pseudo strain to accurately calculate the modulus gradient parameters after the relaxation modulus and reference modulus are determined.

The dynamic modulus of asphalt mixtures is a material property and one of the most important inputs in the Pavement ME Design (AASHTO 2008a). It is also used as an indicator for either the level of aging or damage of asphalt mixtures. Due to its importance, the dynamic modulus has been widely used and well determined for the

* Reprinted with permission from Springer: "An inverse approach to determine complex modulus gradient of field-aged asphalt mixtures." By Meng Ling, Xue Luo, Fan Gu, and Robert L. Lytton. *Materials and Structures*, 50(2), 2017.

laboratory-mixed-laboratory-compacted (LMLC) asphalt mixtures. In general, the modulus of the unaged LMLC asphalt mixtures is affected by some factors such as binder type and content, aggregate type and gradation, and mix design. These factors can be well controlled in the laboratory and the field construction. However, when considering the field-aged asphalt mixtures, the effects of field aging process and non-uniform air void distribution cannot be ignored. On the other hand, the properties of field-aged asphalt mixtures provide valuable information regarding the pavement condition since they can be used to make maintenance decisions and performance predictions.

In general, the field-aged asphalt mixtures become stiffer after a long-term aging period, which is similar with the LMLC mixtures under the long-term aging in the laboratory. In addition to the long-term aging, there is another unique aging feature for the field cores: non-uniform aging in the pavement depth. It is known that the surface of the asphalt layer suffers from the solar radiation and oxidative aging severer than deeper layers, as the oxygen diffuse slowly through the interconnected air voids into the pavement structure from the surface of the pavement. Thus less carbonyl area is formed at deeper layers due to the less volume of oxygen and contact area. As a result, the modulus at the surface is higher than the other layers due to the non-uniform aging effect, and finally a modulus gradient is developed.

2.2 Introduction

As a result, it is preferred to obtain the material properties of the field cores directly. It is known that conducting the mechanical tests on the field cores remains difficult mainly due to the geometry compared to the LMLC mixtures specimens. The

typical issue is the required dimension for a cylindrical specimen. The thickness of field cores normally ranges from 26 mm to 100 mm and even smaller for the overlays, which is insufficient to be used in the standard dynamic modulus test. To overcome this issue, recent studies determine that the thickness for rectangular and cylindrical field core specimens can be as thin as 26 mm for both dynamic modulus test and damage test, and the test results are in the same ranges with those for the standard dimension specimen (Park and Kim 2013). This valuable conclusion provides a guide for dealing with those with small specimen geometries such as field cores. In these studies, the tested specimens are obtained from different depths of one original field core, which are used to reflect the modulus distribution along the pavement depth. The traditional uniaxial tension-compression test is then conducted at different temperatures and frequencies to obtain the dynamic modulus master curves of field cores at different depths. However, the average modulus is measured especially for the top surface of the asphalt layer.

Under this circumstance, this chapter presents a new mechanical method to determine the complex modulus and modulus gradient of field cores using the direct tension test. The direct tension test is adopted because of the three key advantages: 1) it is simple to conduct and only takes less than 1 minute for a given temperature; 2) it causes no damage to the specimen if the strain limitation is carefully controlled; and 3) the tensile modulus is determined instead of compressive modulus. It has been shown that the tensile modulus and compressive modulus of asphalt mixtures are different in both the magnitudes and phase angles (Luo et al. 2013). However, most tests are conducted in the compression mode (AASHTO 2008a) and flexion mode (NF EN 2004). The tensile

modulus is necessary, especially for the characterization of various types of cracking in the asphalt pavements. In this chapter, an inverse approach is proposed to accurately determine the complex modulus and modulus gradient at different temperatures using the elastic theory, pseudo strain concept and elastic-viscoelastic correspondence principle.

This chapter is organized as follows. The next section describes the information and preparation for both field core specimens and LMLC specimens. The test protocol to determine the complex modulus and modulus gradient is also discussed. The following section provides detailed derivations and results of the complex modulus and modulus gradient using the inverse approach. The last section summarizes the findings.

2.3 Direct Tension Test to Measure Modulus Gradient

The test protocol to measure the complex modulus and modulus gradient is elaborated in this section, which include:

- 1) The materials for testing, containing asphalt field cores and LMLC mixtures;
- 2) The configuration and procedure of the direct tension test with a nondestructive monotonically increasing load; and
- 3) The characteristics of mechanical responses of field cores as well as their comparisons with those of LMLC mixtures.

2.3.1 Asphalt Field Cores and LMLC Mixtures

The asphalt field cores include one type of hot mix asphalt (HMA). They are collected from a field project in FM 973 near the Austin Bergstrom airport in Texas. The field asphalt mixtures are fabricated with a PG 70-22 asphalt binder and Texas limestone

aggregates. The binder content is 5.2%, the NMAS is 10 mm. The aggregate gradation can be found in Appendix A. The cores are taken at the center of two lanes of a HMA section at 8 months and 22 months after construction. It is reasonable to assume that the collected cores are not damaged by traffic within this aging period when they are in the field.

In order to demonstrate the features of field cores, laboratory HMA specimens are also fabricated. The parallel tests are performed between the field and LMLC specimens to demonstrate the differences in the measured data. Two air void contents for the laboratory specimens are chosen. The tested LMLC specimens are obtained only from the center of the compacted cylinder samples for the purpose of having uniform air void distributions through their thicknesses.

All of the original cylinder field cores and LMLC mixtures samples are cut and trimmed into rectangular specimens 102 mm long and 76 mm wide. The thickness of the rectangular specimen varies from 38 to 51 mm dependent on the thickness of the original field core. The thickness of the LMLC specimens is 38 mm. Then the steel studs are glued on the top, center and bottom of the specimens for placing linear variable differential transformers (LVDTs). The rectangular field core specimen preparation is shown in Figure 2.1. The air void content, thickness and aging time of each field and LMLC specimen are given in Table 2.1.

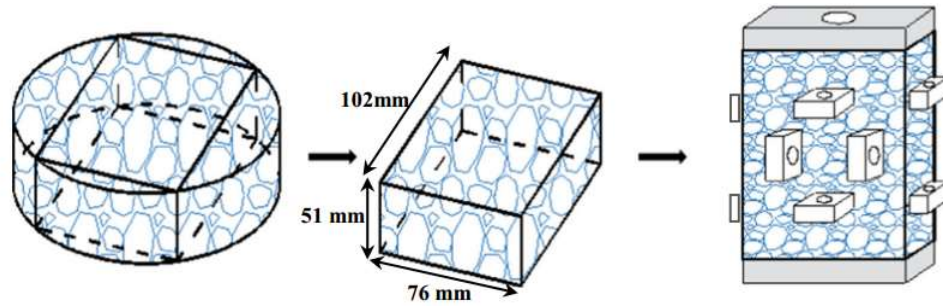


Figure 2.1 Field Core Specimen Preparation

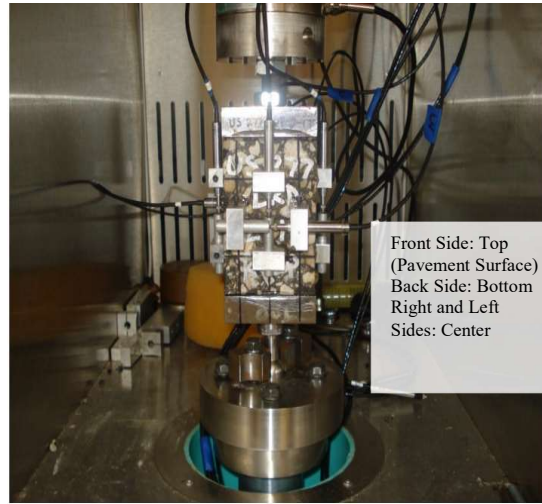
After being prepared in the laboratory, each rectangular specimen is fixed with six LVDTs, as shown in Figure 2.2(a). The two vertical LVDTs are used to measure the vertical deformations of the top and bottom of the specimen, respectively; another pair attached on the two sides is used to measure the vertical deformations of the center of the specimen. The two horizontal LVDTs are used to measure the lateral deformations of the top and bottom, respectively. This lateral deformation is used to determine the Poisson's ratio of field cores, which will be discussed in a following chapter. The gauge length is 50.8 mm for each LVDT.

Table 2.1 Field Cores and Laboratory Fabricated Mixtures Specimens Tested in Direct Tension Test

Material Type	Air Void Content (%)	Field Aging Time (month)	Thickness (mm)
HMA Field Cores	6.6	8	38
	5.8	8	51
	5.5	22	51
	5.3	22	38
LMLC HMA	6.3	N/A	38
	5.2	N/A	38



(a)



(b)

Figure 2.2 Field Core Specimen and Setup of Direct Tension Test: (a) Specimen with LVDTs, (b) Specimen in the MTS

2.3.2 Direct Tension Test

The direct tension test is conducted using the Material Test System (MTS) shown in Figure 2.2(b). A nondestructive monotonically increasing load is applied on the rectangular specimens at 10°C, 20°C and 30°C at a ramp rate of 0.020 mm/min, respectively. This MTS is an electrohydraulic servo machine. It includes a load cell, a temperature chamber, and is connected to a desktop for reading, saving and analyzing the test results including the load and strains. The MTS is also equipped of ball joints. To keep the specimens intact, the maximum tensile strain is set below 100 microstrains as suggested in the literature (Levenberg and Uzan 2004). This type of LVDT can measure 100 microstrains accurately. It takes approximately 2 hours to change the temperature of the specimens from one to another, and it takes approximately 8 hours to finish the entire set of the tests for three temperatures. A new set of specimens are put in the temperature

chamber overnight to reach the temperature equilibrium and recover the temperature loss due to opening the chamber for unloading and removing the previous specimens.

The direct tension tests conducted on the tested specimens at each temperature are repeated three times in order to avoid the undesired test errors and confirm that the specimens are undamaged during testing. Otherwise, the data cannot be used for analysis. Note that a rest period of 15 minutes between the two tests is needed to recover the viscoelastic strains after one test. The three repeated test results are shown in Figure 2.3, which indicates that a rest period of 15 minutes is enough and the repeatability is satisfied.

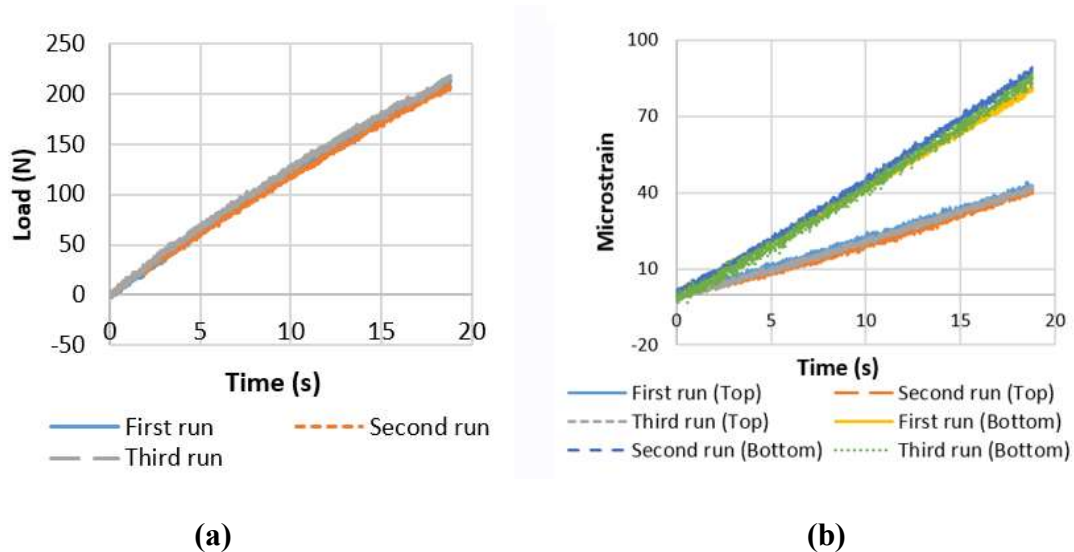


Figure 2.3 Three Repeated Test Results at 10°C, (a) Load in Three Repeated Tests, (b) Top and Bottom Strains in Three Repeated Tests

2.3.3 Mechanical Responses of Field Cores and LMLC Mixtures

The mechanical responses of the field cores and LMLC specimens are discussed herein shown in Figures 2.4 to 2.6. Figure 2.4(a) shows the measured loads applied on the

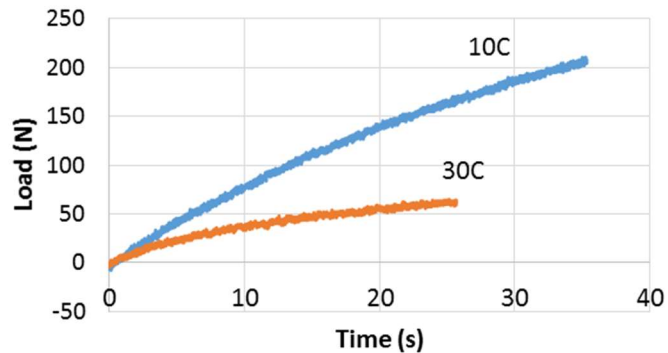
field core specimen when the test temperatures are 10°C and 30°C, respectively. It can be seen that as the temperature increases, the load-time curve becomes smaller and more curved, and the duration of the test is shorter. This observation indicates that the use of time-temperature superposition and thermorheologically simple material can be applied to the field-aged specimens. Figure 2.4(b) presents the applied load when the aging times are 8 and 22 months, respectively, it shows when the aging time is longer, the field core specimens become stiffer.

Figure 2.5 presents the measured vertical and horizontal strains of the field core specimen calculated from the readings of the deformation of one vertical and one horizontal LVDTs attached at the top. The vertical deformations are recorded by the four vertical LVDTs attached at the top, center and bottom, whereas the horizontal deformations are recorded by the two horizontal LVDTs attached on the top and bottom. Note that the vertical strains at the center of the specimen are calculated by averaging the readings from the two LVDTs attached on the two center sides. It is shown that as the tensile load increases, the vertical strain increases whereas the horizontal strain decreases.

Figures 2.6(a) and 2.6(b) compare the induced vertical strains obtained from the corresponding vertical deformation data for the field core specimen and LMLC specimen, respectively. Under the similar loading, the measured vertical strains in the field and laboratory specimens are obviously different. The three measured vertical strains in the field core specimen in Figure 2.6(a) have different magnitudes at the three locations, which are closely related to the modulus at each depth. However, the three measured strains for the LMLC specimen are almost identical from Figure 2.6(b). It is known that

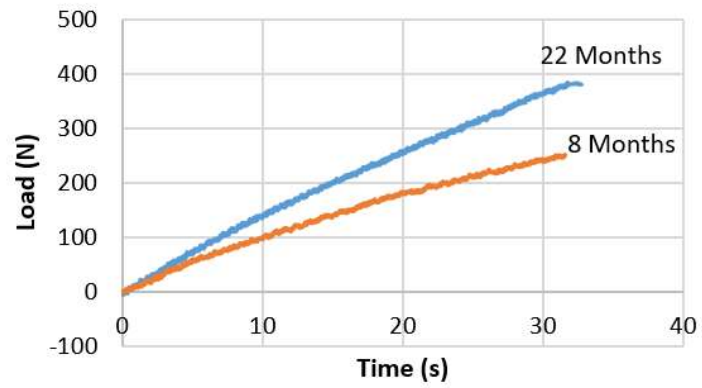
the LMLC specimen has an almost uniform modulus across the thickness. Therefore, the difference between three measured strains of the LMLC specimen is minimal. The measured strains at the top, center and bottom for the field core specimens are different, which is due to the non-uniform modulus distribution in the field cores. In general, the strain at the top is smallest and the strain at the bottom is largest, which reflects the modulus distribution. Figure 2.6(c) illustrates that the strain is smaller and increases slower for the field specimen with a longer aging time, which shows the long-term aging effect on the mechanical response.

Due to the existence of the modulus gradient, the monotonic load applied at the center of the field core specimen is actually located different from the neutral axis as shown in Figure 2.7. It is expected that the neutral axis is closer to the stiffer side than to the softer side. This eccentricity induces a bending moment and corresponding bending strains at these three locations during the testing. Therefore, the measured strains at the top, center and bottom include two parts: the tensile strain and bending strain. The discussions regarding the eccentric loading are detailed in the next section.



(a)

Figure 2.4 Monotonic Loads in Direct Tension Test: (a) Loads at Different Temperatures, (b) Loads at Different Aging Times



(b)

Figure 2.4 Continued

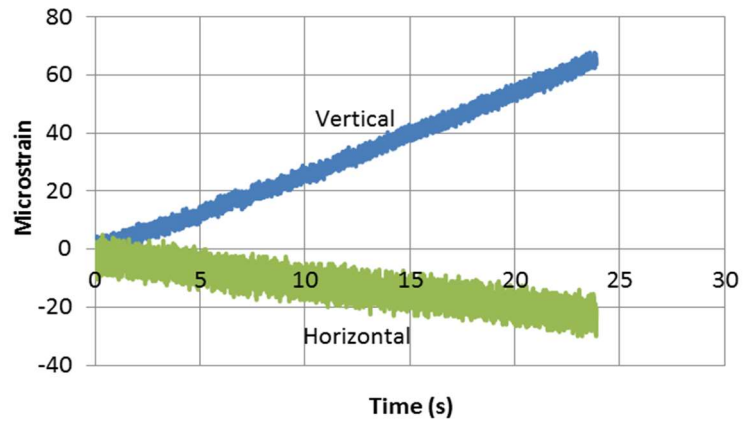
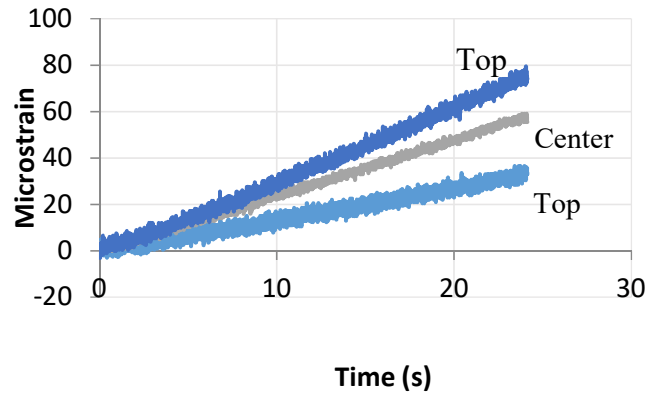
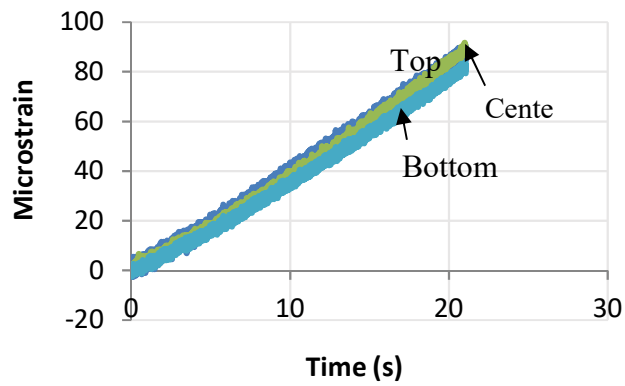


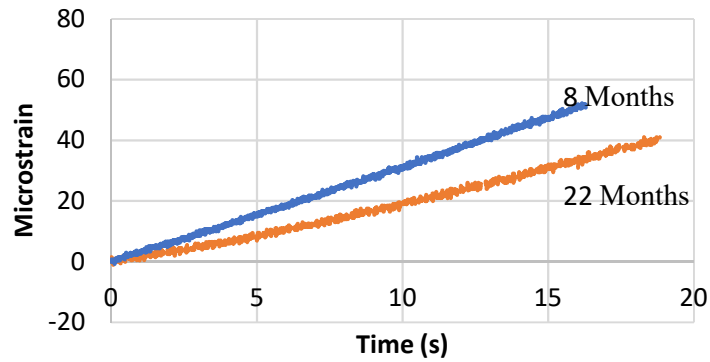
Figure 2.5 Measured Vertical and Horizontal Strains at Top of Field Core Specimen



(a)



(b)



(c)

Figure 2.6 Measured Vertical Strains at Top, Center, and Bottom of Tested Specimen: (a) Strain at Different Depths of Field Core Specimen, (b) Strain of Laboratory Fabricated Specimen, (c) Strain at Different Aging Times of Field Core Specimen

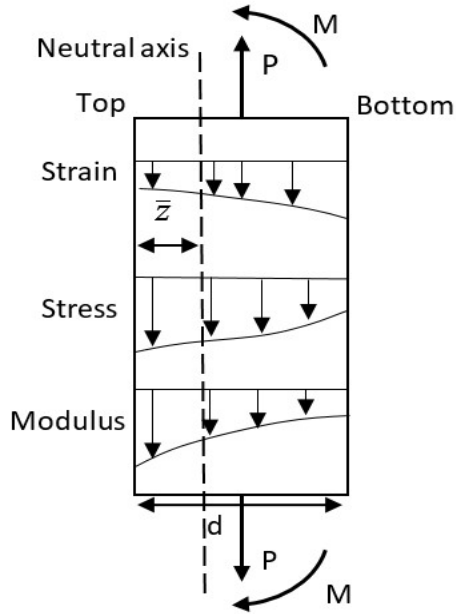


Figure 2.7 Illustration of Non-Uniform Distributions of Stress, Strain, and Modulus in Field Core Specimen

In the previous study, the modulus gradient is obtained and verified based on the strain amplitude. As proposed in the previous study, the modulus gradient of a field core specimen at a specific loading frequency and temperature is modeled by Equations 2.1 and 2.2:

$$E(z) = E_d + (E_0 - E_d) \left(\frac{d-z}{d} \right)^n \quad (2.1)$$

$$k = \frac{E_0}{E_d} \quad (2.2)$$

where $E(z)$ is the dynamic modulus in pavement depth z at a specific loading frequency and temperature; E_d and E_0 are the dynamic moduli at the top and bottom at the same loading condition, respectively; d is the thickness of the field core specimen; n is the model

parameter, which presents the shape of the stiffness gradient; and k is the ratio of the modulus at the top to the modulus at the bottom. When z equals to $\frac{d}{2}$, the center modulus E_c is obtained.

2.4 Derivations of Complex Modulus Gradient

The objective of this section is to determine the complex modulus based on the unique characteristics of field cores mentioned above. More specifically, there are two main subjects that have to be addressed:

- 1) How to determine the parameters of the modulus gradient of a field core specimen;
and
- 2) How to convert the measured data and parameters of modulus gradient to its corresponding viscoelastic property: complex modulus.

2.4.1 Inverse Application of Viscoelastic-Elastic Correspondence Principle

As stated above, the stress, strain, and modulus of an asphalt field core are non-uniformly distributed as schematically shown in Figure 2.7. This adds significant difficulty in the viscoelastic analysis of field core specimens. The solution to this problem is to introduce the viscoelastic-elastic correspondence principle (Schapery 1984), so a viscoelastic problem can be inferred from a reference elastic problem. For an undamaged viscoelastic material, there is a linear relationship between the stress and the pseudo strain:

$$\sigma(t) = E_R \varepsilon^R(t) \quad (2.3)$$

where $\sigma(t)$ is the stress in the undamaged viscoelastic material, or called viscoelastic stress; $\varepsilon^R(t)$ is the pseudo strain; and E_R is the reference modulus, which can be assigned as the Young's modulus (Zhang et al. 2012). The pseudo strain is defined as

$$\varepsilon^R(t) = \frac{1}{E_R} \int_0^t E(t-\xi) \frac{d\varepsilon(\xi)}{d\xi} d\xi \quad (2.4)$$

where $E(t)$ is the relaxation modulus of the material; $\varepsilon(\xi)$ is the strain history; ξ is a time between 0 and t ; t is the loading time. The relaxation modulus for a short loading time like the one in the direct tension test above can be defined by:

$$E(t) = E_\infty + E_1 e^{-\frac{t}{\kappa}} \quad (2.5)$$

where E_∞ is the long term relaxation modulus; E_1 is the relaxation modulus coefficient; and κ is the relaxation time.

Once the dynamic modulus of a viscoelastic material is known from the measured load and strain, the relaxation modulus can be calculated from the dynamic modulus-relaxation modulus relationship. Then the reference modulus and pseudo strain can be obtained from Equations 2.3 to 5. The reason why the pseudo strain needs to be determined and used other than the measured strain is that it is not appropriate to use the measured strain which is the viscoelastic strain in the elastic theory (i.e., bending theory) to solve for the modulus gradient parameters n and k . In this chapter, due to the complexities of stress and strain in the field core specimen, an inverse analysis with an iteration process is proposed to determine the pseudo strain and the gradient parameters. More specifically, it contains the following steps:

- I. In the first iteration:

- 1) Use the measured tensile strain of an undamaged field core specimen as the seed value for the pseudo strain. In other words, temporarily, there is an elastic relationship between the measured stress and the measured strain;
 - 2) Utilize the elastic theory along with the measured load/strains to determine the modulus gradient parameters. The values of n and k are determined and checked for their dependence on loading time and frequency;
 - 3) Convert the functions of the measured load/strains and modulus gradient parameters using the Laplace transform to calculate the corresponding viscoelastic property: complex modulus;
 - 4) Calculate the relaxation modulus then the reference modulus using the calculated complex modulus; and
 - 5) Calculate the pseudo strain by the reference modulus.
- II. In the second iteration: replace the measured strain with the calculated pseudo strain as the seed value after the first iteration and repeat steps 2 to 5.
- III. In the following iterations (normally 3 to 5):
- 1) Replace the pseudo strain in the previous iteration with the newest one and repeat steps 2 to 5; and
 - 2) Stop the iteration when the pseudo strain is stable. Then the modulus gradient parameters converge, the complex modulus and pseudo strain will not change.

In the following subsections, the major steps are elaborated in sequence and the final equations of the complex moduli of different depths of the field cores are presented.

2.4.2 Determination of Modulus Gradient Parameters

Using the pseudo strain to determine the modulus gradient parameters contains three steps discussed below.

Step 1. Decomposition of vertical strains in field core specimens

As indicated above, there is an eccentricity between the location of the load and neutral axis in the field core specimens. As a result, the vertical pseudo strains at top, center and bottom can be decomposed into the tensile portions and bending portions as follows:

$$\varepsilon_0 = \varepsilon_{0t} - \varepsilon_{0b} = \frac{aP}{AE_0} - \frac{M\bar{Z}}{IE_0} \quad (2.6)$$

$$\varepsilon_c = \varepsilon_{ct} + \varepsilon_{cb} = \frac{bP}{AE_c} + \frac{M\left(\frac{d}{2} - \bar{Z}\right)}{IE_c} \quad (2.7)$$

$$\varepsilon_d = \varepsilon_{dt} + \varepsilon_{db} = \frac{cP}{AE_d} + \frac{M(d - \bar{Z})}{IE_d} \quad (2.8)$$

where ε_0 , ε_c , ε_d are the vertical pseudo strains at top, center and bottom of the specimen, respectively; ε_{0t} , ε_{ct} and ε_{dt} are the tensile portions of the vertical pseudo strains at top, center and bottom, respectively; ε_{0b} , ε_{cb} and ε_{db} are the bending portions of the vertical pseudo strains at top, center and bottom, respectively; P is the magnitude of the load; and a , b , and c are the coefficients to account for the non-uniform distribution of the stress in the field core specimen; A is the loading area; M is the induced moment $\left[M = P\left(\frac{d}{2} - \bar{z}\right) \right]$; \bar{Z} is the distance from the neutral axis to the top, $\frac{d}{2} - \bar{Z}$ and $d - \bar{Z}$ are the distances from the neutral axis to the center and from the neutral axis to the bottom,

respectively; E_0 , E_c and E_d are the modulus at top, center and bottom, respectively; and I is the moment of inertia. Note that the bending strain at the top is negative, so it is subtracted from the strain at the top as in Equation 2.6. At the other two locations, the bending strains are positive.

Step 2. Formulation of value and location of the load in field core specimens

Assume that the distribution of the tensile portion of the pseudo strain is:

$$\varepsilon_t(z) = \varepsilon_{0t} + \frac{\varepsilon_{dt} - \varepsilon_{0t}}{d} z \quad (2.9)$$

The modulus has a distribution defined in Equation 2.1. Then the magnitude of the load is calculated by the integral of the tensile stress as follows:

$$P = m \int_{z=0}^{z=d} \varepsilon_t(z) E(z) dz = A \left\{ \varepsilon_{0t} \left[\frac{1}{2} + \frac{k-1}{n+2} \right] + \varepsilon_{dt} \left[\frac{1}{2} + \frac{k-1}{(n+1)(n+2)} \right] \right\} \times E_d \quad (2.10)$$

where m and d are the width and thickness of the field core specimen, respectively; and A is the cross sectional area ($A = md$). The location of the neutral axis relative to the top of the specimen is determined by Equation 2.11:

$$\begin{aligned} \bar{Z} &= \frac{1}{P} \int_{z=0}^{z=d} mz \varepsilon_t(z) E(z) dz \\ &= \frac{d \left\{ \varepsilon_{0t} \left[\frac{1}{6} + \frac{(k-1)(n+5)}{(n+1)(n+2)(n+3)} \right] + \varepsilon_{dt} \left[\frac{1}{3} - \frac{2(k-1)}{(n+1)(n+2)(n+3)} \right] \right\}}{\varepsilon_{0t} \left[\frac{1}{2} + \frac{k-1}{n+2} \right] + \varepsilon_{dt} \left[\frac{1}{2} + \frac{k-1}{(n+1)(n+2)} \right]} \end{aligned} \quad (2.11)$$

For the case of the LMLC specimen, the pseudo strains are the same at different locations and k equals to 1. Thus \bar{Z} reduces in $\frac{d}{2}$ in Equation 2.11, which is the centerline of the

specimen. However, for a field specimen, \bar{Z} is always smaller than $\frac{d}{2}$ given that k is larger than 1.

Step 3. Solve for n and k in the modulus gradient model

Select the values of the pseudo strain and load at different loading times (in this case from 5s to 35s) of the direct tension test, which are given in Table 2.2. For every second of the loading time, substitute the measured values into Equations 2.6 to 2.11 and solve for a , b , c , n , and k . The results of a field core specimen are also given in Table 2.2. For the first iteration, the values of the pseudo strains are equal to the tensile strains measured from the direct tension test, which are used as the seed values. In the following iterations, these strains are the pseudo strains calculated from the previous iteration after determining the complex modulus and relaxation modulus detailed in the following subsection. The changes of the values of a , b , c , n , and k become small from the second iteration to the third one. Therefore, it is regarded that the results converge at the third iteration. The details regarding the determinations of iterations and pseudo strains will be discussed in the next section.

It should be noted that the exponent n and the ratio k are the material properties since they are the two parameters in the modulus gradient equation and must be included in the application of the correspondence principle which transforms an elastic equation into the Laplace transform of a viscoelastic equation. With each iteration, both n and k are determined to be time-dependent, as seen in Table 2.2, which shows their final converged values. They both increase slightly with loading time and decrease slightly with frequency.

Table 2.2 Results of Calculations of Modulus Gradient of a Field Core Specimen (8 Months Aged at 30°C) from Direct Tension Test

Iteration	Loading Time (s)	Pseudo Strain ($\mu\epsilon$)	Load (N)	a	b	c	n	k	n_0	k_0
1 st	5-15	6.12	30.41	1.26	0.73	0.85	2.96	2.44	2.54	2.16
	16-25	20.42	165.6	1.28	0.72	0.86	3.73	2.82		
	26-35	34.71	268.34	1.30	0.72	0.87	3.89	3.09		
2 nd	5-15	3.67	30.41	1.23	0.70	0.84	2.91	2.40	2.53	2.12
	16-25	12.15	165.6	1.26	0.71	0.85	3.68	2.79		
	26-35	20.3	268.34	1.29	0.71	0.85	3.86	3.06		
3 rd	5-15	3.53	30.41	1.22	0.68	0.82	2.90	2.39	2.52	2.11
	16-25	11.79	165.6	1.25	0.70	0.84	3.67	2.76		
	26-35	19.15	268.34	1.27	0.70	0.84	3.85	3.05		

2.4.3 Determination of Complex Modulus Using Approximated n and k

After obtaining the modulus gradient parameters, the next step is to convert the elastic property to the corresponding viscoelastic property using the Laplace transform. The procedure is given below in sequence.

In the direct tension test, the measured load and tensile portions of the strains versus time of a field core specimen are modeled as follows:

- Monotonic tensile load $P(t)$:

$$P(t) = a_p(1 - e^{-b_p t}) \quad (2.12)$$

- Tensile portions of the strains at the top and bottom of the field core specimen:

$$\epsilon_{0t}(t) = a_0(1 - e^{-b_0 t}) \quad (2.13)$$

$$\epsilon_{dt}(t) = a_d(1 - e^{-b_d t}) \quad (2.14)$$

- Modulus gradient parameters n and k :

$$n = n_0 e^{b_n t} \quad (2.15)$$

$$k = k_0 e^{b_k t} \quad (2.16)$$

where a_p and b_p are the fitting parameters for the load; a_0 and b_0 are the fitting parameters for the tensile portion of strain at the top; a_d and b_d are the fitting parameters for the tensile portion of the strain at the bottom; and n_0 , k_0 , b_n and b_k are the fitting parameters for the modulus gradient parameters n and k .

Using the Laplace transform, the elastic forms in Equations 2.12 to 2.16 can be rewritten as viscoelastic solutions in the Laplace domain by an s-multiplied Laplace transform (Carson-transform), which are shown in Equations 2.17 to 2.21:

$$\bar{P}(s) = \frac{a_p b_p}{s(s + b_p)} \quad (2.17)$$

$$\bar{\varepsilon}_{0r}(s) = \frac{a_0 b_0}{s(s + b_0)} \quad (2.18)$$

$$\bar{\varepsilon}_{dt}(s) = \frac{a_d b_d}{s(s + b_d)} \quad (2.19)$$

$$s\bar{n}(s) = \frac{n_0 s}{s - b_n} \quad (2.20)$$

$$s\bar{k}(s) = \frac{k_0 s}{s - b_k} \quad (2.21)$$

where s is the variable in the Laplace domain; $\bar{P}(s)$, $\bar{\varepsilon}_{0r}(s)$, $\bar{\varepsilon}_{dt}(s)$, $\bar{n}(s)$, and $\bar{k}(s)$ are the corresponding load, strains, n and k in the Laplace domain. The viscoelastic forms of n and k are shown in Equations 2.22 and 2.23. For small values of b_n and b_k , the values of $s\bar{n}(s)$ and $s\bar{k}(s)$ are closely approximated by the constants n_0 and k_0 , as shown in Equations 2.22 and 2.23.

$$\left[s\bar{n}(s) \right]_{s=i\omega} = \left[\frac{n_0 s}{s - b_n} \right]_{s=i\omega} = \frac{n_0 \omega^2 - n_0 b_n \omega}{b_n^2 + \omega^2} \approx n_0 \quad (2.22)$$

$$\left[s\bar{k}(s) \right]_{s=i\omega} = \left[\frac{k_0 s}{s - b_k} \right]_{s=i\omega} = \frac{k_0 \omega^2 - k_0 b_k \omega}{b_k^2 + \omega^2} \approx k_0 \quad (2.23)$$

To obtain the modulus in the Laplace domain, the Laplace transform is taken on both sides of Equation 2.10 and used to solve for the modulus at the bottom, which gives:

$$\bar{E}_d(s) = \frac{\bar{P}(s)}{sA \left\{ \bar{\varepsilon}_{0t}(s) \left[\frac{1}{2} + \frac{k_0 - 1}{n_0 + 2} \right] + \bar{\varepsilon}_{dt}(s) \left[\frac{1}{2} + \frac{k_0 - 1}{(n_0 + 1)(n_0 + 2)} \right] \right\}} \quad (2.24)$$

where $\bar{E}_d(s)$ is the bottom modulus in the Laplace domain.

The relationship between the complex modulus and relaxation modulus is shown in Equation 2.25 (Findley et al. 1989):

$$E^*(\omega) = i\omega L\{E(t)\}_{s=i\omega} = [s\bar{E}(s)]_{s=i\omega} \quad (2.25)$$

Therefore, the complex modulus at the bottom of the field core specimen can be obtained by substituting Equation 2.24 into Equation 2.25, which is shown by:

$$E_d^*(\omega) = [s\bar{E}_d(s)]_{s=i\omega} = \frac{\bar{P}(s)}{A \left\{ \bar{\varepsilon}_{0t}(s) \left[\frac{1}{2} + \frac{k_0 - 1}{n_0 + 2} \right] + \bar{\varepsilon}_{dt}(s) \left[\frac{1}{2} + \frac{k_0 - 1}{(n_0 + 1)(n_0 + 2)} \right] \right\}_{s=i\omega}} \quad (2.26)$$

The final expression of the complex modulus at the bottom is shown in Equation 2.27 by substituting Equations 2.17 to 2.19, 2.22 and 2.23 into Equation 2.26:

$$E_d^*(\omega) = \frac{(AC + BD) + (AD - BC)i}{A^2 + B^2} \quad (2.27)$$

in which

$$A = \left\{ \begin{array}{l} -\left[\frac{1}{2} + \frac{k_0 - 1}{n_0 + 2} \right] a_0 b_0 + \left[\frac{1}{2} + \frac{k_0 - 1}{(n_0 + 1)(n_0 + 2)} \right] a_d b_d] \omega^2 + \left(\frac{1}{2} + \frac{k_0 - 1}{n_0 + 2} \right) a_0 b_0 b_p b_d \\ + \left[\frac{1}{2} + \frac{k_0 - 1}{(n_0 + 1)(n_0 + 2)} \right] a_d b_d b_p b_d \end{array} \right\} md$$

$$B = \left[\left(\frac{1}{2} + \frac{k_0 - 1}{n_0 + 2} \right) a_0 b_0 (b_p + b_d) + \left[\frac{1}{2} + \frac{k_0 - 1}{(n_0 + 1)(n_0 + 2)} \right] a_d b_d (b_p + b_0) \right] \omega md$$

$$C = a_p b_p (b_0 b_d - \omega^2)$$

$$D = a_p b_p (b_0 + b_d) \omega$$

When the complex modulus at the bottom is determined, the complex modulus at the top in the Laplace domain can be determined as shown in Equation 2.28:

$$s \overline{E}_0(s) = s k_0 \overline{E}_d(s) \quad (2.28)$$

where $\overline{E}_0(s)$ is the corresponding modulus at the top of a field core in the Laplace domain.

The complex modulus at the center of the field core in the Laplace domain is determined by:

$$s \overline{E}_c(s) = s \overline{E}_d(s) \left(1 + \frac{k_0 - 1}{2^{n_0}} \right) \quad (2.29)$$

Similarly, the complex modulus at the top and that at the center can be determined as follows:

$$E_0^*(\omega) = [s k_0 \overline{E}_d(s)]_{s=i\omega} = \frac{k_0 (AC + BD) + k_0 (AD - BC)i}{A^2 + B^2} \quad (2.30)$$

$$E_c^*(\omega) = [s \overline{E}_c(s)]_{s=i\omega} = \frac{\left(1 + \frac{k_0 - 1}{2^{n_0}} \right) (AC + BD) + \left(1 + \frac{k_0 - 1}{2^{n_0}} \right) (AD - BC)i}{A^2 + B^2} \quad (2.31)$$

The complex modulus includes a real part and an imaginary part, and the dynamic modulus is defined as

$$|E^*(\omega)| = \sqrt{E'^2 + E''^2} \quad (2.32)$$

where E' is real or storage modulus component; E'' is imaginary or loss modulus component; $|E^*(\omega)|$ is the magnitude of the complex modulus, or dynamic modulus. The phase angle of the complex modulus is calculated using Equation 2.33, which is also frequency dependent.

$$\varphi_E = \arctan\left(\frac{E''}{E'}\right) \quad (2.33)$$

Note that the range of the frequency for the dynamic modulus depends on the duration of the loading time of the direct tension test. A time-frequency relationship is needed to convert the ranges in the time domain to frequency domain. In this chapter, Equation 2.34 is used to make the approximate inverse Laplace Transform based on the Schapery (1961):

$$f(t) = [s\bar{f}(s)]_{s=\frac{1}{2t}} \quad (2.34)$$

The calculated dynamic modulus versus the associated frequency is shown in Figure 2.8, using the fitting parameters at the three temperatures.

Similar to the complex modulus, the complex Poisson's ratio is also obtained from the direct tension test using the correspondence principle. The derivation of viscoelastic Poisson's ratio is detailed in Appendix B. It is shown that the Poisson's ratio at top and bottom are different, which is also related to the modulus gradient.

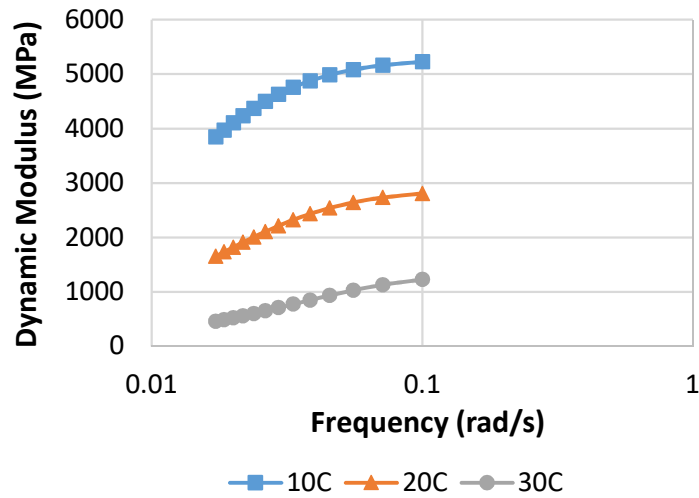


Figure 2.8 Calculated Dynamic Modulus of a Field Core Specimen at Three Temperatures

2.4.4 Determination of Complex Modulus Using Complex n and k

It should be mentioned that the calculations of the complex modulus above are based on the approximated results of Laplace transform of n and k by Equations 2.22 and 2.23. This generates a dynamic modulus gradient, but results in an issue that the phase angles at the top, center, and bottom are the same according to Equations 2.27, 2.30, 2.31, and 2.33. As a matter of fact, the phase angle should also have a gradient along the pavement depth. However, the derivations and computations become too complicated when using the accurate results of Laplace transform of n and k . In this chapter, the approximation method to calculate the complex moduli is adopted. The derivations and expressions of the complex moduli with complex n and k are presented in the Appendix A, which also provides the phase angle gradient accurately.

2.4.5 Determination of Relaxation Modulus, Reference Modulus and Modulus Gradient

After obtaining the initial complex modulus, the corresponding relaxation modulus and reference modulus can be computed. First, the master curve of the dynamic modulus is constructed at a reference temperature of 20°C using the sigmoidal model shown in Equation 2.35.

$$\log |E^*(\omega)| = \delta + \frac{\alpha}{1 + e^{\beta + \gamma \cdot \log(\omega \cdot a_T)}} \quad (2.35)$$

where δ is the value of the lower asymptote, α is the difference between the upper and lower asymptotes, β and γ are shape coefficients, and a_T is the time-temperature shift factor. The Williams-Landel-Ferry (WLF) equation is employed as the shift factor equation:

$$\log a_T = -\frac{C_1(T - T_r)}{C_2 + (T - T_r)} \quad (2.36)$$

where T is the test temperature, T_r is the reference temperature, C_1 and C_2 are the positive fitting parameters. Figure 2.9 shows the master curve constructed by Equations 2.35 and 2.36 for the bottom modulus of a field core specimen.

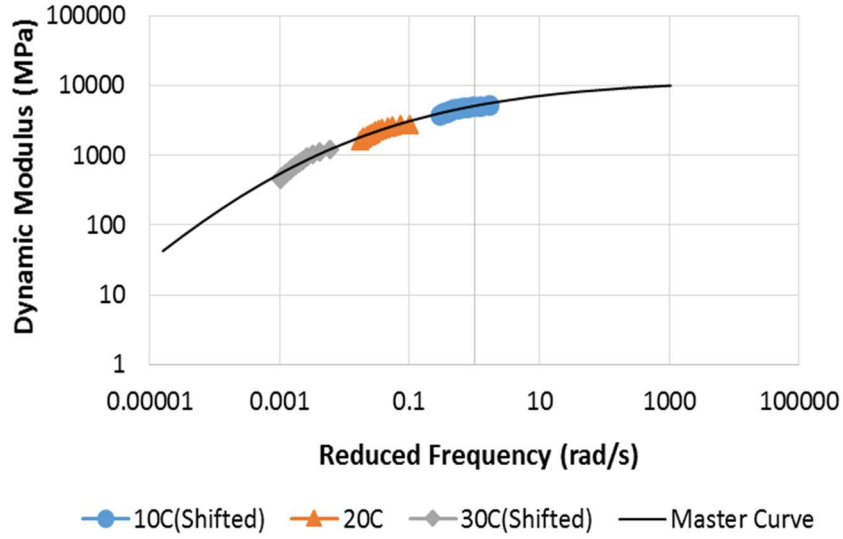


Figure 2.9 Dynamic Modulus Master Curve of a Field Core Specimen

Once the dynamic modulus master curve is determined, the relaxation modulus can also be constructed according to their relationships shown in Equations 2.37 and 2.38. When the relaxation modulus is fitted by the Prony series model:

$$E(t) = E_{\infty} + \sum_{j=1}^M E_j e^{-\frac{t}{\kappa_j}} \quad (2.37)$$

where E_{∞} is the long term relaxation modulus; E_j are the relaxation modulus coefficients; and κ_j are the relaxation times. The dynamic modulus is given by:

$$|E^*(\omega)| = \sqrt{\left(E_{\infty} + \sum_{j=1}^M \frac{\omega^2 k_j^2 E_j}{1 + \omega^2 k_j^2} \right)^2 + \left(\sum_{j=1}^M \frac{\omega k_j E_j}{1 + \omega^2 k_j^2} \right)^2} \quad (2.38)$$

As a result, the fitting parameters for the relaxation modulus can be computed by Equation 2.38 based on the dynamic modulus master curve determined above. The calculation results is given in Figure 2.10.

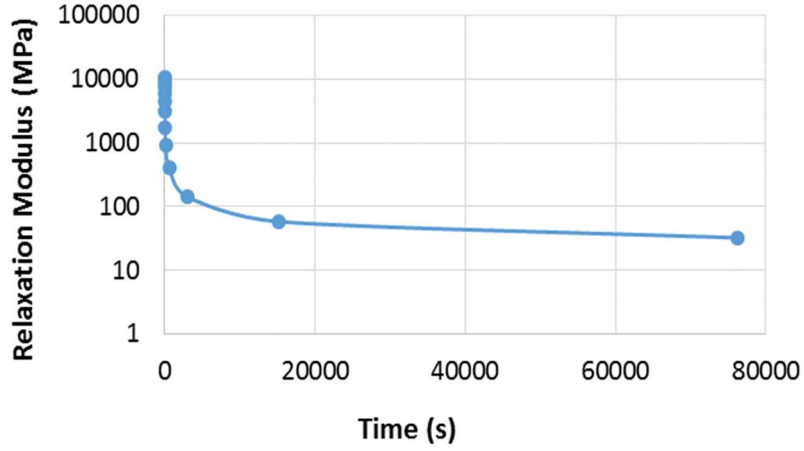


Figure 2.10 Relaxation Modulus Determined from the Dynamic Modulus Master Curve

To facilitate the calculation of the pseudo strain, fit the relaxation modulus determined above by a simpler model like that in Equation 2.5. Substitute Equation 2.5 and the strain history formulated by Equation 2.14 into Equation 2.4, which gives:

$$\varepsilon_d(t) = \frac{1}{E_R} \left[E_\infty a_d (1 - e^{-b_d t}) + \frac{E_1 a_d \kappa}{\frac{1}{b_d} - \kappa} \left(e^{-b_d t} - e^{-\frac{t}{\kappa}} \right) \right] \quad (2.39)$$

where $\varepsilon_d(t)$ is the pseudo strain at the bottom of the field core specimen. Since the Young's modulus of asphalt materials is not easy to determine using Zhang et al. (2012), the representative elastic modulus formulated by Equation 2.40 is used to estimate the reference modulus (Luo et al. 2016).

$$E_R = E_{re} = \frac{1}{2} \left[\left| E^* \right|_{f=\frac{1}{t_p}} + E \left(t = \frac{t_p}{2} \right) \right] \quad (2.40)$$

where E_{re} is the representative elastic modulus; $|E^*|$ is the dynamic modulus; f is the frequency of a load pulse; and t_p is the pulse time of a load. The pulse time of 0.1 s is chosen using Equation 2.40, the reference modulus is calculated with the dynamic modulus master curve and relaxation modulus determined previously. The pseudo strains at 30°C at different iterations and the strain measured from the direct tension test are shown in Figure 2.11. It can be seen that the pseudo strain is smaller than the measured strain, especially for the longer loading time. This phenomenon matches the understanding that the viscous effect is more active when the temperature is higher, which is corresponding to a lower loading frequency or a higher loading time.

Once the relationships of the pseudo strains and time are determined, the measured strains used in the first iteration are replaced by the pseudo strains to recalculate the values of n and k using Equations 2.6 to 2.11. Then the updated values of n and k are inserted into Equations 2.26 to 2.40 to obtain the new dynamic modulus master curve and relaxation modulus again. This procedure is repeated until the convergence requirement of the n and k values are met. In general, the values of n and k become stable within 5 iterations. For instance, in Figure 2.11, the change of the pseudo strain at 30°C is minimal after 3 iterations. Once the convergence is reached, the complex modulus and the modulus gradient parameters can be regarded as the actual material properties. The three complex moduli are determined with the updated n and k using Equations 2.27, 2.30 and 2.31. The modulus gradient is then extracted from the dynamic modulus curves at the three depths and three temperatures for 8 and 22 months aged field core specimens when the loading frequency is 0.1 Hz, which is shown in Figure 2.12.

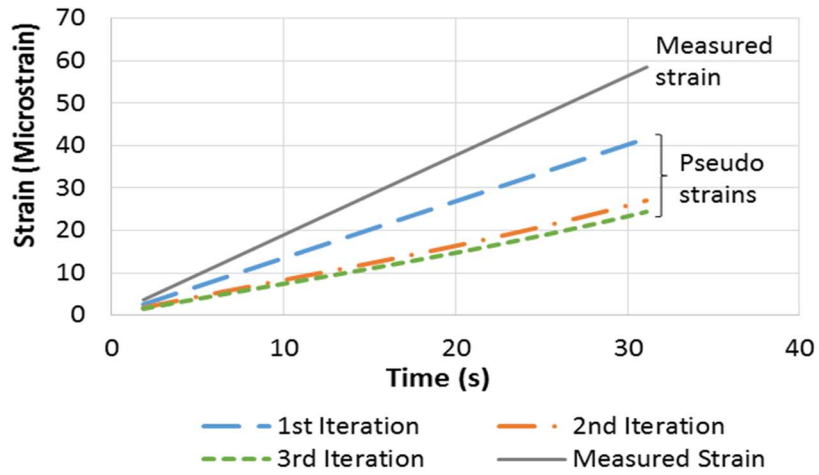


Figure 2.11 Measured Strain at the Bottom of a Field Core Specimen and Associated Pseudo Strains at Different Iterations

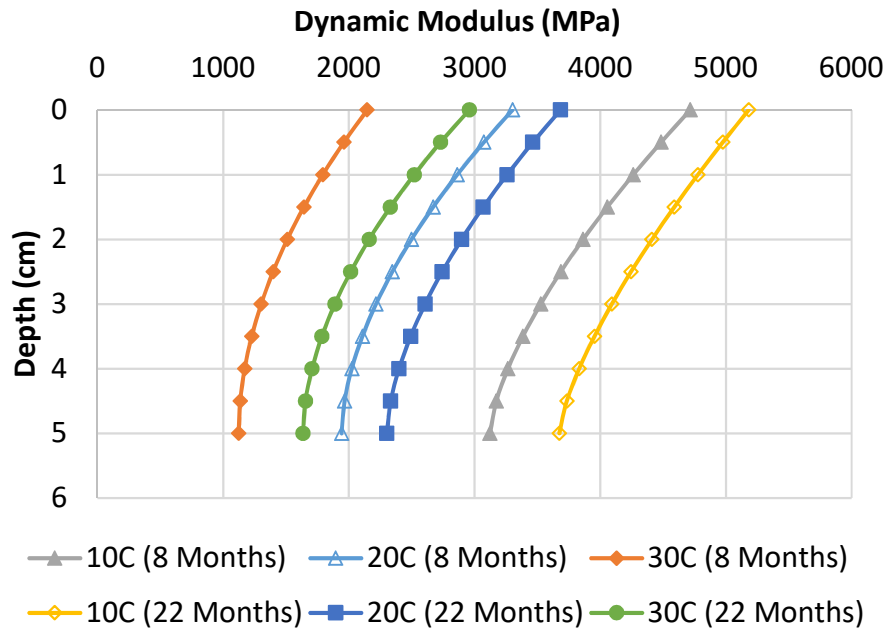


Figure 2.12 Modulus Gradients of 8 and 22 Months Aged Field Specimens at Three Temperatures and 0.1 Hz

2.5 Conclusions

This chapter targets the asphalt field cores and proposes a methodology to determine the complex modulus and modulus gradient using the direct tension test. A total of four HMA field cores at two aging times and two laboratory fabricated mixtures are prepared and tested in this chapter. The major contributions of this chapter are summarized as follows:

- The strains at different depths of the field core specimens are different, which is related to the modulus gradient, however, the strains for the LMLC mixtures are almost identical.
- Due to the nature of the modulus gradient, the strains should be decomposed into tensile and bending portions from the elastic theory. The tensile portion is used and the two aging parameters n and k in the modulus gradient equation for different loading times and the modulus gradient can be obtained.
- Using the Laplace transform and correspondence principle, the elastic forms can be further converted into the viscoelastic forms, which can be used to determine the dynamic modulus.
- An inverse approach with an iteration process for field cores is proposed using the pseudo strain concept. The relaxation modulus and reference modulus are determined to calculate the pseudo strain. Since the measured strain (i.e., viscoelastic strain) is not appropriate to be used in the elastic formulas, pseudo strain should be calculated to determine the accurate results of n and k , and dynamic modulus.

3. TIME-TEMPERATURE-AGING-DEPTH SHIFT FUNCTIONS FOR DYNAMIC MODULUS MASTER CURVES OF ASPHALT MIXTURES

3.1 Overview

Oxidative aging is one of the most important environmental effects on the viscoelastic properties of asphalt mixtures. This chapter aims to characterize the aging viscoelastic properties of the asphalt mixtures such as the dynamic modulus at different aging times and pavement depths, and then develops two aging shift functions to account for the effects of long-term aging and non-uniform aging within the pavement depth. The tensile creep test and direct tension test are conducted on 12 laboratory-mixed-laboratory-compacted (LMLC) mixtures with three laboratory aging times and 16 field-aged asphalt mixtures with four field aging times, respectively. The dynamic modulus of LMLC mixtures are determined from the tensile creep test results, and the elastic-viscoelastic correspondence principle is utilized to obtain the dynamic modulus of field-aged mixtures from the direct tension test. The dynamic modulus master curves for different aging times and pavement depths are then constructed using the modified Christensen-Anderson-Marasteanu (CAM) model. The long-term aging shift function is determined as a function of aging time, activation energy, acceleration aging factor and aging temperature. The depth shift function is determined as a function of pavement depth. With the aid of the two aging shift functions, a single dynamic modulus master curve can be formed after taking into account the effects of temperature, long-term aging and non-uniform aging.

3.2 Introduction

It is well-known that oxidative aging is one of the essential factors that has a significant influence on the viscoelastic properties of asphalt mixtures and performance of asphalt pavements. Generally speaking, aging is a chemical reaction between asphalt binders and oxygen, which causes the formations of polar carbonyl area (CA) and sulfoxides (Bell 1989). During the aging process, the asphalt loses volatile fractions, which leads to the hardening of the binders. For an asphalt pavement, there are usually two stages of aging: one is called short-term aging, and the other is named as long-term aging. The short-term aging occurs during the procedures of mixing, compaction and lay down, thus it is during the construction period. In this stage, the aging effect can be assumed to be identical from the surface to the bottom of the asphalt layer since the chemical reaction between oxygen and binders is uniform. The long-term aging starts after construction. The oxygen in the atmosphere first reacts with the mixtures at the pavement surface then slowly diffuses inside the asphalt layer through the connected air voids, and less chemical reactions are generated in the deeper layers below the surface. Therefore, unlike the short-term aging, it is a non-uniform aging process. The modulus gradient in the asphalt pavement is developed during the long-term aging period, which is an important characteristic of the field-aged mixtures. As a result, the surface of the pavement becomes stiffer and more brittle than the deeper layers, which is more prone to various types of cracking. It is also shown that the long-term aging is mainly affected by aging time and aging temperature.

Due to the pronounced effects of oxidative aging, there are considerable research efforts on the characterization of the aging behavior. The properties of the aged asphalt binders are well determined. One approach is to conduct rheological or physical tests on the binders. The Fourier Transform Infrared Spectroscopy (FTIR) is a popular method to measure the increase of CA. It is an efficient tool to analyze the aging process based on the chemical components. In addition to this approach, the dynamic shear modulus of the asphalt binders aged at different aging times or aging temperatures are measured using the dynamic shear rheometer (DSR) (Masad et al. 2008; Glover et al. 2005). The increase of the shear modulus is used as an indicator of aging level of the asphalt binders. The viscosity can also be obtained, which is further correlated with some empirical relationship to predict the dynamic modulus of asphalt mixtures. Additionally, the Global Aging System (GAS) is a widely-used aging prediction method, which is based on the viscosity gradient obtained from the extracted binders of numerous field cores at different pavement depths in different climate zones of North America. On the mixture level, the mechanical tests such as dynamic modulus test are conducted on the laboratory-mixed-laboratory-compacted (LMLC) asphalt mixtures at different aging times (Daniel et al. 1998; Abu Al-Rub et al. 2013). However, the standard dynamic modulus test method is not applicable to the field-aged asphalt mixtures due to the complications associated with the field conditions such as field core dimension. To overcome this obstacle, an indirect tension test (IDT) method is proposed for determining the dynamic modulus of asphalt field cores. This method ignores a significant characteristic of the field-aged asphalt mixtures, i.e., non-uniform aging in pavement depth. More importantly, at current stage, a single

dynamic modulus master curve cannot be constructed including the effects of temperature and aging for both of the laboratory-aged and field-aged asphalt mixtures, and only the coefficients of the sigmodal model at different ages are empirically related to the aging time.

In order to address the shortcomings of the aforementioned methods, it is preferred to develop a new aging model to evaluate and predict the dynamic modulus master curves of aged asphalt mixtures with taking into account the long-term aging and non-uniform aging. In other words, a single dynamic modulus master curve with the effects of temperature, loading time, long-term aging, and non-uniform aging should be constructed by applying the temperature and aging shift functions. In the studies prior to this work, a mechanical-based analytical method is developed to determine the complex modulus gradient of the field-aged mixtures using the direct tension test (Ling et al. 2017a). The same test protocol is adopted in this chapter to obtain the dynamic modulus at different field aging times and pavement depths of field-aged mixtures. The creep test is conducted on the LMLC mixtures to obtain the tensile dynamic modulus. The results from the two tests are then used to construct the dynamic modulus master curves, then develop, verify and implement the two aging shift functions.

This chapter is organized as follows. The next section first introduces the asphalt mixtures used in this chapter including the field-aged and laboratory-aged mixtures. The two laboratory testing protocols and analysis methods are discussed briefly, then presents the dynamic modulus at different aging conditions. The subsequent section shows the construction of dynamic modulus master curves, the development and application of the

long-term aging shift function for the LMLC mixtures, respectively. The following section discusses the implementation of the aging shift function and the development of depth shift function to account for the non-uniform aging effect in the pavement depth, and the construction of a final single master curve for field-aged mixtures. The summary of findings and conclusions are included in the last section.

3.3 Laboratory Testing Method and Results

3.3.1 Material and Mix Design

The asphalt field cores used in this chapter include one type of hot mix asphalt (HMA) and one type of warm mix asphalt (WMA) treated by a foaming process. The field cores are taken from one HMA section and one WMA section in Austin, Texas. The field-aged mixtures are fabricated with a PG 70-22 asphalt binder and Texas limestone aggregates. The water content is 5% by weight of the binder in the WMA foaming process. The binder content of 5.2%, the NMAS of 9.5 mm, and the aggregate source and gradation are identical for the HMA and WMA. The mix design, aggregate source and gradation are detailed in this technical report (Glover et al. 2014). The thicknesses of the field cores range from 38 to 51 mm. The cores are taken at the center of two lanes of the HMA section and the WMA section at 1 month, 8 months, 14 months and 22 months after construction. It is reasonable to assume that the collected cores are not damaged by traffic within the aging periods when they are in the field.

A PG 67-22 asphalt binder and Texas limestone aggregates are used for the fabrication of the LMLC mixture specimens. The optimum binder content of 4.5% and the aggregate gradation are determined based on Texas Department of Transportation

(TxDOT) Type C gradation and TxDOT specification TEX-204-F, respectively (TxDOT, 2004). Two target air void contents of 4% and 7% are included. The loose mixes are first conditioned in the oven for 4 hours at 135 °C in accordance with AASHTO R 30, then they are compacted using the Superpave gyratory compactor (SGC) into cylindrical specimens with 150 mm in diameter and 175 mm in height. The cylindrical specimens are cored to 100 mm in diameter and 150 mm in height after cooling down to obtain uniform air void distributions in the center of the specimens. After coring, the specimens are conditioned in the environmental room for 0 month, 3 months, and 6 months at 60°C to simulate the long-term aging in the field. There are two replicates tested for each air void content and aging time. Thus, there are 12 laboratory specimens tested in total. It should be noted that the sources of aggregates and binders are different for the field and LMLC mixtures, and the comparison and match between the laboratory aging and field aging are beyond the scope.

3.3.2 Direct Tension Test

The direct tension test is conducted in the MTS machine on the field core specimens. The original cylindrical field core collected from the pavement is shown in Figure 3.1(a). Then the cylindrical cores are cut and trimmed into prismatic shape, which is shown in Figure 3.1(b).

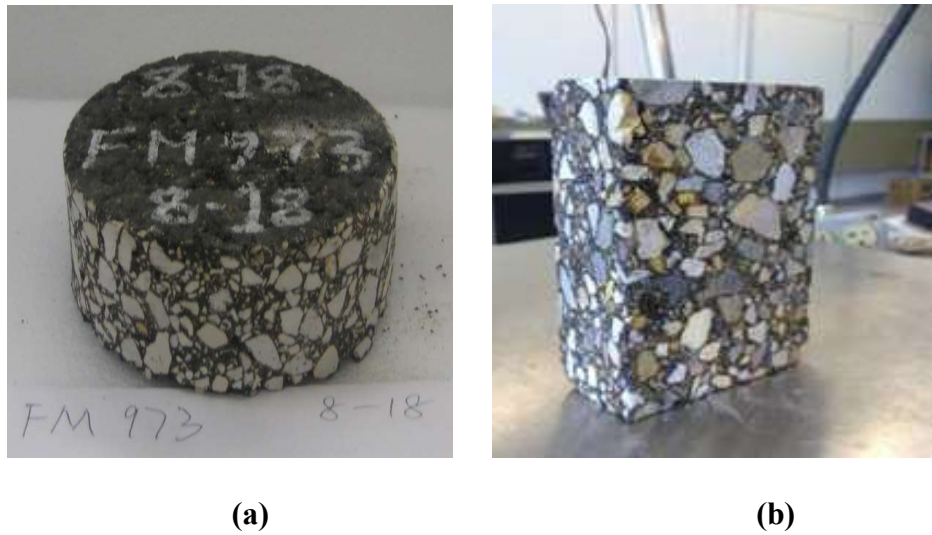


Figure 3.1 Preparation of Test Specimen: (a) Original Field Core, (b) Cut and Trimmed Specimen

The prismatic field core specimens are glued with six linear variable differential transformers (LVDTs). The two vertical LVDTs are used to measure the vertical deformations at the top (i.e., surface of asphalt layer) and bottom (i.e., bottom of asphalt layer) of the specimen, respectively; another pair attached on the two center sides (i.e., center of asphalt layer) is used to measure the vertical deformations at the center of the specimen. The average value of the readings from these two center LVDTs is used to calculate the center strain. The gauge length is 50.8 mm for each LVDT. A monotonically tensile load is applied at the center of the rectangular field core specimens at 10, 20 and 30°C to obtain the strains at top, center and bottom. The maximum strain is 100 micro-strains to keep the specimens undamaged. Figure 3.2 shows the gluing jig to fix the two end caps. More details regarding the specimen preparation and direct tension test protocol are documented in the previous chapter.

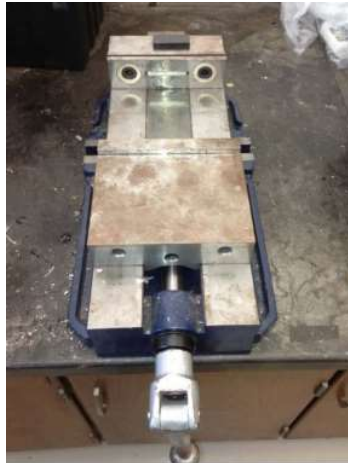


Figure 3.2 Specimen Gluing Jig

It is worth mentioning that the tensile load applied at the centerline of the field-aged specimens induces a bending moment during the testing since the neutral axis of the field core specimens is located different from the centerline. More specifically, it is closer to the top than to the bottom of the field core specimens due to the modulus gradient. The bending/eccentric loading theory is used to solve for the modulus gradient, and the pseudo strains at the top, center and bottom are calculated as the necessary inputs instead of the measured strains. The pseudo strain is used since the bending/eccentric loading theory is an elastic theory, it is not appropriate to use the measured strain (i.e., viscoelastic strain) directly. Meanwhile, an inverse approach is developed to obtain the accurate results of the pseudo strain. Elastic equations are formulated to model the measured load, strains at top, center and bottom as functions of loading time. Then the elastic forms are further converted into viscoelastic forms using the elastic-viscoelastic correspondence principle. The explanations and derivations regarding this analysis approach is not repeated here, which is detailed in Chapter 2. This method mentioned above is used to determine the

dynamic moduli at different aging times, temperatures, and pavement depths, which will be used to construct the dynamic modulus master curve of the field-aged mixtures.

3.3.3 Tensile Creep Test

The tensile creep test is conducted on LMLC mixtures in the MTS at 10, 20 and 30°C with a loading time of 40 s. Three axial LVDTs are mounted on the middle part, with an angular separation of 120° apart from each other. The gauge length is 88.9 mm. The LMLC specimens are conditioned in the environmental chamber for two hours to reach the temperature equilibrium for each test. The Laplace transform is applied to convert the obtained creep compliance to the relaxation modulus. The calculations for determining the relaxation modulus from creep compliance are not repeated here, which can be found in this report (Lytton et al. 1993).

3.3.4 Test Results

Figure 3.3(a) shows the examples of the dynamic modulus at different depths of the field core specimens. At a given frequency, the dynamic modulus at the top of the specimen is largest and the one at the bottom is smallest. In addition, the dynamic modulus at the center is closer to the one at the bottom. This indicates that aging in the top half of the field core is much severer than the bottom half. It also shows that as the frequency increases, the dynamic modulus become larger, which reflects the viscoelasticity of asphalt mixtures.

Figures 3.3(b) and 3.3(c) show the examples of the dynamic modulus of field specimens at different aging times and temperatures. The long-term aged asphalt mixtures

become stiffer and more brittle, which potentially increases the possibility of fatigue cracking and thermal cracking, especially at the surface of the asphalt layer. For different temperatures, the trend of the change agrees with that the modulus becomes smaller at higher temperatures.

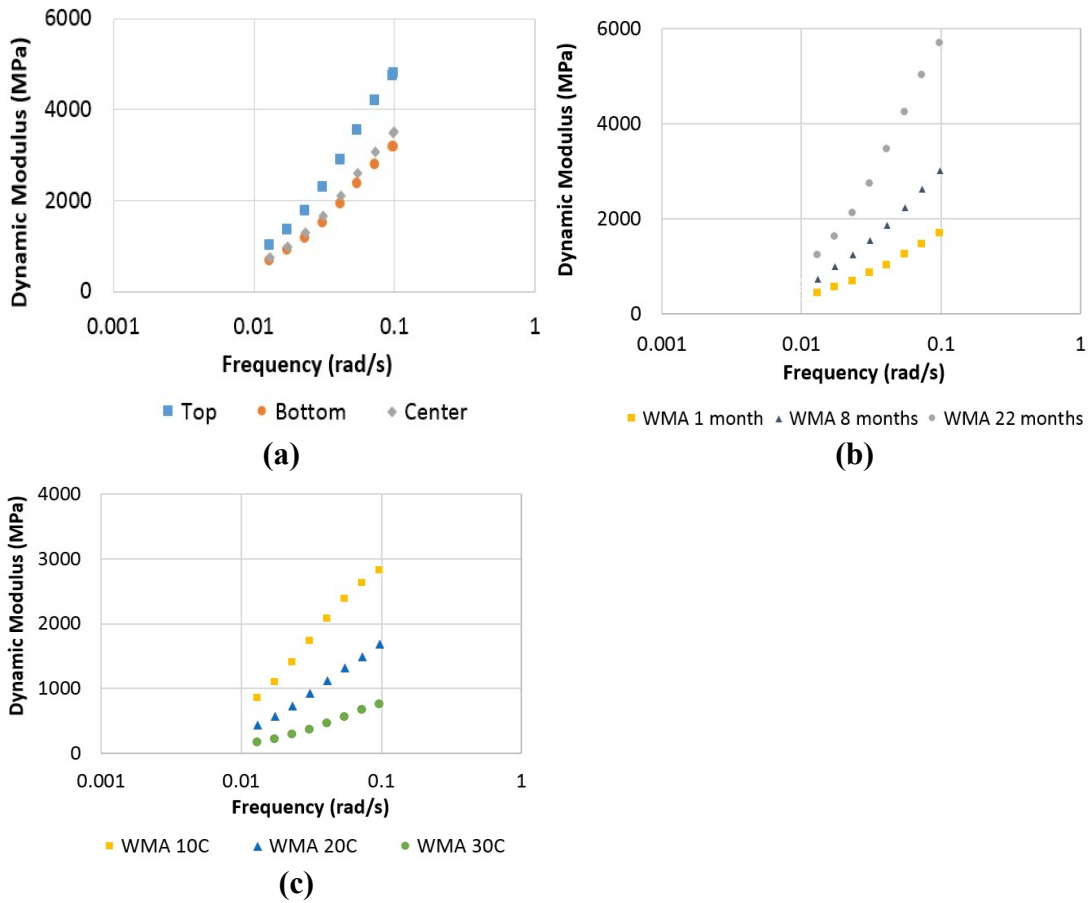


Figure 3.3 Dynamic Modulus at Different Conditions: (a) Different Depths, (b) Different Aging Times, (c) Different Temperatures

3.4 Construction of Dynamic Modulus Master Curve for LMLC Mixtures

Since the dynamic modulus test is not performed directly on the LMLC mixtures, the tensile relaxation modulus of LMLC mixtures is converted to the corresponding dynamic modulus. The Prony series model in Equation 3.1 is used to fit the relaxation modulus data.

$$E(t) = E_{\infty} + \sum_{j=1}^M E_j e^{\left(-\frac{t}{k_j}\right)} \quad (3.1)$$

where $E(t)$ is the relaxation modulus, E_{∞} is the steady state relaxation modulus, E_j and K_j are the relaxation coefficients and times, respectively. M is 11 in this case. After determining E_{∞} in the spring element and all coefficients including the E_j and k_j in 11 Maxwell elements by fitting the data using Equations 3.1 and 3.2. Equation 3.3 are used to calculate the real and imaginary parts of the complex modulus and magnitude of complex modulus (i.e., dynamic modulus), respectively.

$$E'(\omega) = E_{\infty} + \sum_{j=1}^M \frac{\omega^2 k_j^2 E_j}{1 + \omega^2 k_j^2}, \quad E''(\omega) = \sum_{j=1}^M \frac{\omega k_j E_j}{1 + \omega^2 k_j^2} \quad (3.2)$$

$$|E^*(\omega)| = \sqrt{\left(E_{\infty} + \sum_{j=1}^M \frac{\omega^2 k_j^2 E_j}{1 + \omega^2 k_j^2}\right)^2 + \left(\sum_{j=1}^M \frac{\omega k_j E_j}{1 + \omega^2 k_j^2}\right)^2} \quad (3.3)$$

The modified Christensen-Anderson-Marasteanu (CAM) model (Marasteanu and Anderson 1999) is used to construct the dynamic modulus master curve of the asphalt mixtures, as shown in Equation 3.4.

$$|E^*(\omega)| = E_e + \frac{E_g - E_e}{\left[1 + \left(\frac{\omega_c E}{\omega a_T}\right)^{\frac{\log 2}{R_E}}\right]^{\frac{R_E}{\log 2}}} \quad (3.4)$$

where E_g and E_e are the glassy modulus (i.e., modulus at infinite frequency) and equilibrium modulus (i.e., modulus at zero frequency), respectively; ω_{cE} is crossover frequency; $a_T(T)$ is time-temperature shift factor; R_E is rheological index of the asphalt mixtures. The time-temperature shift factor for the CAM model is shown in Equation 3.5 using the William-Landel-Ferry (WLF) equation:

$$a_T = 10^{\frac{-C_1(T-T_R)}{C_2+(T-T_R)}} \quad (3.5)$$

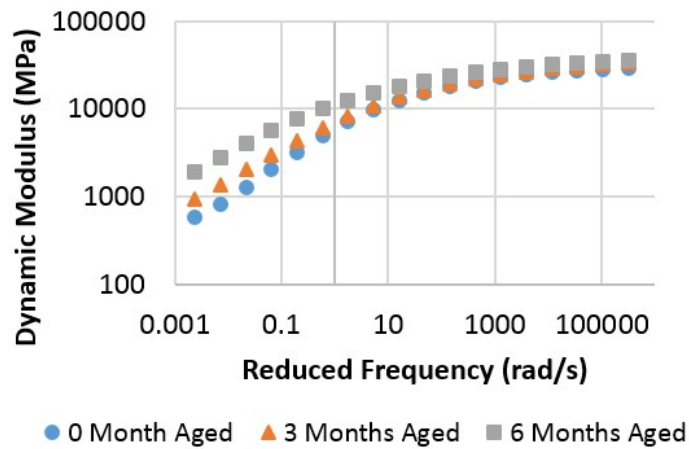
where C_1 and C_2 are the fitting parameters of the WLF equation; T_R is the reference temperature in Kelvin (20°C); T is the test temperature in Kelvin. It is shown that the CAM model is an accurate function to construct the master curves of the dynamic modulus of asphalt mixtures in tension and compression modes of the LMLC specimens (Lytton et al. 2017 and Luo et al. 2010). It is adopted in this chapter since its parameters have specific physical significance. In the CAM model, the crossover frequency ω_{cE} is the indicator of the overall stiffness of the mixtures, E_e and E_g are the low and high asymptotes of the master curve, respectively; and rheological index R_E is the shape factor of the master curve. In this chapter, the parameters of E_g and ω_{cE} are employed as the aging parameters for the dynamic modulus master curves at different aging periods, which will be discussed in the next section.

Using the method above, the dynamic modulus master curves for the LMLC mixtures are determined. Then the data points are fitted using the CAM model by minimizing the error sum of squares (SSE). The parameters E_g , R_E and ω_{cE} in the CAM

model are determined and shown in Table 3.1 for the tested LMLC mixtures. The master curves for the LMLC mixtures with air void contents of 4 and 7% are shown in Figures 3.4(a) and 3.4(b), respectively.

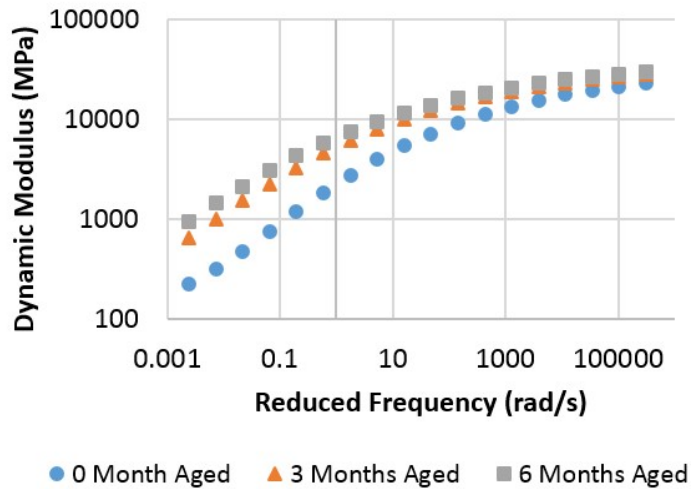
Table 3.1 Calculated CAM Model Parameters

Mixture Type	Glassy Modulus (MPa)	Crossover Frequency (rad/s)	Rheological Index
4% 0 Month	31801	0.109718	1.16520
4% 3 Months	39402	0.010827	1.53283
4% 6 Months	41403	0.000935	1.63738
7% 0 Month	31827	0.084390	1.65467
7% 3 Months	38248	0.002436	1.87641
7% 6 Months	39751	0.000735	1.93958



(a)

Figure 3.4 Dynamic Modulus Master Curve: (a) 4% Air Void Content, (b) 7% Air Void Content



(b)

Figure 3.4 Continued

3.4.1 Determination of Aging Shift Function

After obtaining the dynamic modulus master curves for the LMLC mixtures at different aging times, the determination of the aging shift function is discussed in this section. The aging shift function is defined to quantify the aging level for an asphalt mixture at a specific aging time compared to the same asphalt mixture at an unaged or reference aging level. To efficiently characterize the aging effect on dynamic modulus master curves at different aging times, the aging shift function should be capable of shifting the dynamic modulus master curves at longer aging times to the reference aging time, and eventually form a single dynamic modulus master curve, which includes the aging effect.

After obtaining the dynamic modulus master curves for the LMLC mixtures at different aging times, the determination of the aging shift function is discussed in this

section. The aging shift function is defined to quantify the aging level for an asphalt mixture at a specific aging time compared to the same asphalt mixture at an unaged or reference aging level. To efficiently characterize the aging effect on dynamic modulus master curves at different aging times, the aging shift function should be capable of shifting the dynamic modulus master curves at longer aging times to the reference aging time, and eventually form a single dynamic modulus master curve, which includes the aging effect.

3.4.2 Vertical Shift and Rotation

As can be seen from Table 3.1, the glassy modulus for dynamic modulus master curves at different aging periods is not identical, showing a larger value of the glassy modulus asymptote for the asphalt mixtures at longer aging periods. It indicates that the aging rheological property of asphalt mixtures may be different from that of the asphalt binders, since the glassy modulus for the binders is normally assumed to be identical at different aging times. As a result, a vertical shift is needed to normalize the higher asymptotes at the longer aging periods to that at the reference aging time (i.e., unaged state). As seen from Table 3.1, the glassy modulus at different aging times follows the power function. Therefore, Equation 3.6 is used to determine the vertical shift factor.

$$\left(\frac{E_{gx}}{E_{g0}} \right) = \left(\frac{a_x}{a_0} \right)^{n_E} \quad (3.6)$$

where E_{gx} , E_{g0} are glassy modulus at x months and reference aging time, respectively; a_x , a_0 are the aging time of interest and reference aging time, respectively, unit in months; n_E is the model parameter.

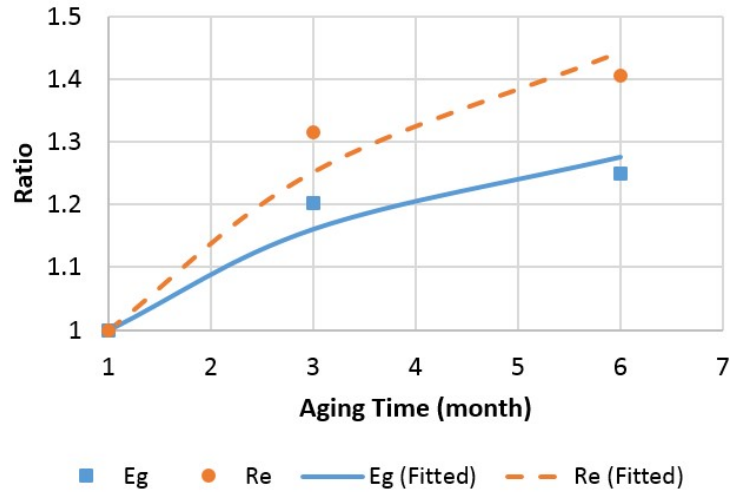
As indicated earlier, the rheological index R_E is the shape factor of the master curve. More specifically, the master curve at a longer aging period normally has a flatter shape, which means a more gradual transition. The rheological index R_E can also be used to determine the relaxation spectrum. In order to form a single master curve, it is important to rotate the master curves at other aging times to be identical to that at the reference aging time before applying the horizontal aging shift factor. It shows that the rheological index of the mixtures increases when the aging time increases, which follows the similar trend as the asphalt binders at longer aging times. The power law equation is used to determine the change of the rheological index for the rotation, as shown in Equation 3.7.

$$\left(\frac{R_{Ex}}{R_{E0}} \right) = \left(\frac{a_x}{a_0} \right)^{n_R} \quad (3.7)$$

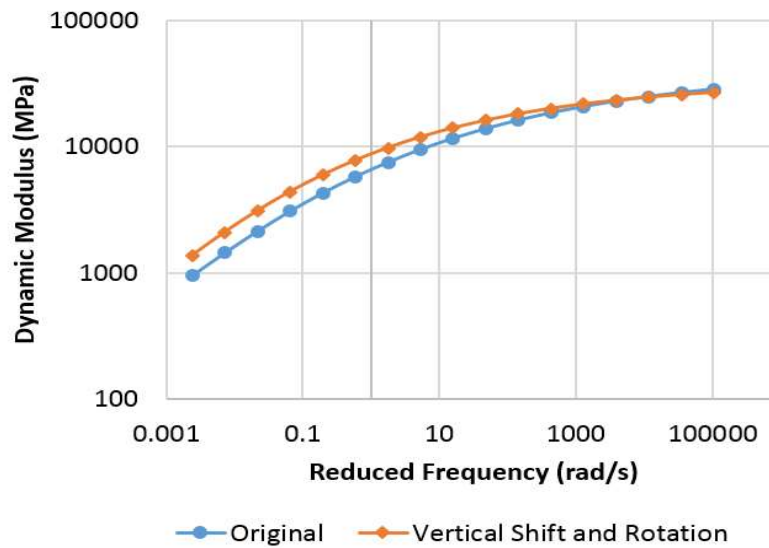
where R_{Ex} and R_{E0} are rheological index at x months and at the reference aging time, respectively; a_x , a_0 are the age of interest, and reference aging time, respectively. n_R is the model parameter.

Examples are given using the constructed dynamic modulus master curves for the LMLC mixtures with 7% air void content. The ratios for both calculated and fitted glassy modulus and rheological index are shown in Figure 3.5(a). Note that a_0 is 1 in the calculation as the unaged state. The vertical shift and rotation are accomplished by using Equations 3.6 and 3.7 to normalize the two aging parameters at other aging times. Figure 3.5(b) shows the modified 6 months aged master curve after applying the vertical shift and rotation to the original 6 months aged modulus curve. As can be seen, the modified master curve and original master curve have different shapes and magnitudes. The vertical shifted

and rotated master curves for the 3 and 6 months aged mixtures and the original master curve for the 0 month aged mixtures are shown in Figure 3.5(c).

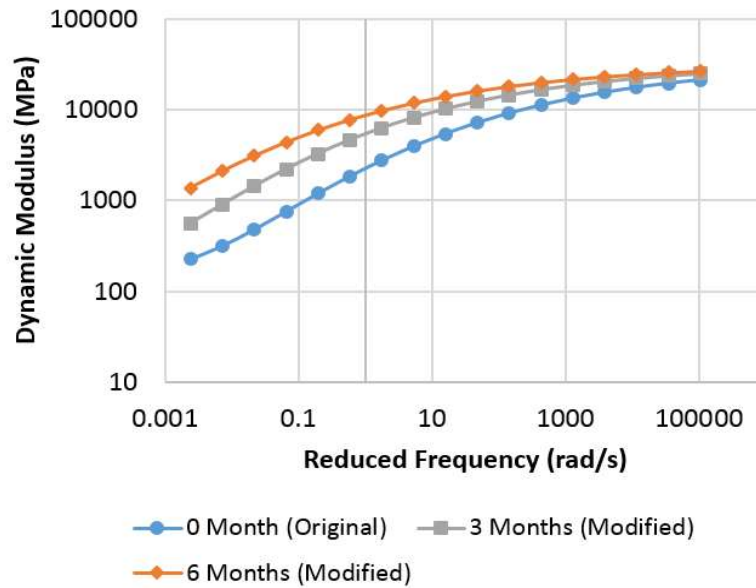


(a)



(b)

Figure 3.5 Vertical Shift and Rotation Process: (a) Fitted Aging Parameters, (b) Modified and Original 6 months Master Curves, (c) Original and Modified Master Curves



(c)

Figure 3.5 Continued

3.4.3 Determination of Horizontal Aging Shift Factor

This section describes how to develop a horizontal aging shift factor to construct a single aging dynamic modulus master curve. With the horizontal aging shift factor, it is possible to shift the modified master curves at longer aging periods horizontally to that at the reference aging time. Attempts are given to use some famous shift equations such as the WLF equation and log-linear equation to develop the shift factor. However, they are not able to shift them into a single master curve as the time-temperature shift. The reason may be that the fundamental principles of oxidative aging and time-temperature superposition are totally different. As shown before, the aging is mainly affected by two

factors: aging time and aging temperature. Therefore, the horizontal aging shift factor is proposed in Equation 3.8:

$$a_A(a, T) = e^{\left[b(a-a_0) - A \frac{E_a}{R} \left(\frac{1}{T} - \frac{1}{T_0} \right) \right]} \quad (3.8)$$

where $a_A(a, T)$ is the horizontal aging shift factor at the aging time a and aging temperature T in Kelvin; a_0 is the initial aging time or unaged time ($a_0 = 0$), A is the acceleration factor to account for the laboratory accelerated aging process due to high aging temperature; E_a is the activation energy, R is the gas constant ($8.314 \times 10^{-3} \text{ kJ mol}^{-1} \text{ K}^{-1}$), T is the average monthly temperature in a field location or the laboratory aging temperature for an aging period a , and T_0 is the initial average monthly temperature in that field location or the reference aging temperature in the laboratory.

As can be seen from Equation 3.8, the horizontal aging shift factor is a function of aging time and aging temperature. The power function is used to account the effect of aging time on the dynamic modulus master curve. The Arrhenius equation is used to determine the oxidative aging rate for the mixtures under various aging temperatures compared to the reference aging temperature. For the LMLC asphalt mixtures tested in this chapter, the aging temperature is unchanged since they are conditioned at the same temperature 60°C .

In the construction of the dynamic modulus aging master curve, the aging reduced frequency f' is determined as

$$f'_{(a,T)} = a_A(a, T) f \quad (3.9)$$

where $f'_{(a,T)}$ is the reduced frequency and f is the previous frequency after the time-temperature shift. Once applying this horizontal aging shift factor, a final single master curve is formed by shifting simultaneously the other two modified master curves of the 3 and 6 months aged mixtures in Figure 3.5(c) horizontally to the right of the master curve of the 0 month aged mixtures. The final aging master curve is formed and shown in Figure 3.6. It indicates that the dynamic modulus master curve for the LMLC mixtures considering both aging time and loading time is constructed as efficiently as the time-temperature master curve, which can be used to predict the master curve of the LMLC mixtures under long-term aging.

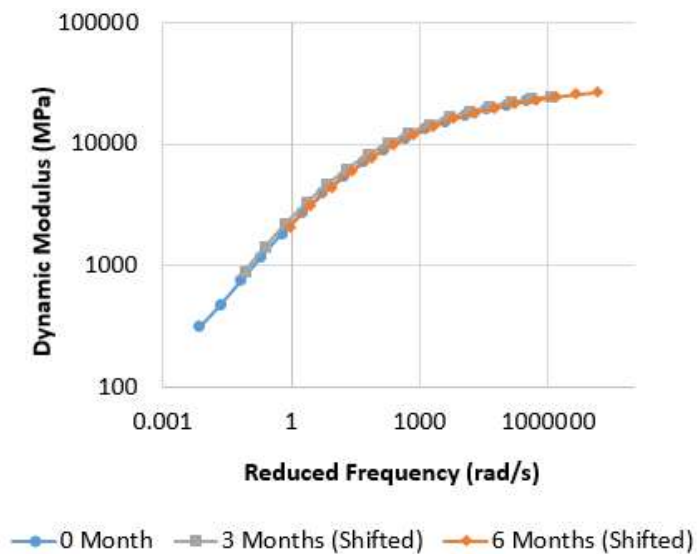


Figure 3.6 Final Aging Dynamic Modulus Master Curve

3.4.4 Application of Aging Shift Function

In order to check whether the aging shift function is applicable to other LMLC test data, the dynamic modulus data is collected from Lolly (2013). Lolly investigated the effect of laboratory accelerated aging and documented the standard dynamic modulus test results performed using AASHTO TP 62 (AASHTO 2006) for different aging temperatures and aging times. In his thesis, the loose mixes were mixed and aged at two aging times and three aging temperatures. Table 3.2 shows the data collected and used in this chapter for different aging conditions. The standard (LT) with 4 hours aging time is selected as the reference aging state.

Table 3.2 Specimens with Different Aging Conditions

Condition	Mixing Temperature	Aging Temperature	Aging Time	Sample Replicates
Standard (LT)	305°F	275°F	4 Hours	3
			8 Hours	3
Elevated (HT)	330°F	300°F	6 Hours	3
			8 Hours	3

The CAM model shown in Equation 3.4 is utilized to construct the dynamic modulus master curves using the dynamic modulus data at five different temperatures and six different frequencies. The parameters ω_{cE} , E_g and R_e can be determined from constructing the master curves, which are presented in Table 3.3.

Table 3.3 CAM Model Parameters

Aging Condition	Glassy Modulus (MPa)	Crossover Frequency (rad/s)	Rheological Index
LT 4h	24010.93	0.0027901	1.623549
LT 8h	39989.86	0.0001513	2.170985

Table 3.3 Continued

Aging Condition	Glassy Modulus (MPa)	Crossover Frequency (rad/s)	Rheological Index
HT 6h	27009.75	0.0001998	2.240798
HT 8h	39429.85	0.0000075	2.405836

Following the same procedures detailed in 3.1.1, the vertical shift and rotation are applied to normalize the high asymptotes and shapes of the master curves at other aging conditions. Figure 3.7 shows the three modified master curves and one original master curve at the reference aging condition.

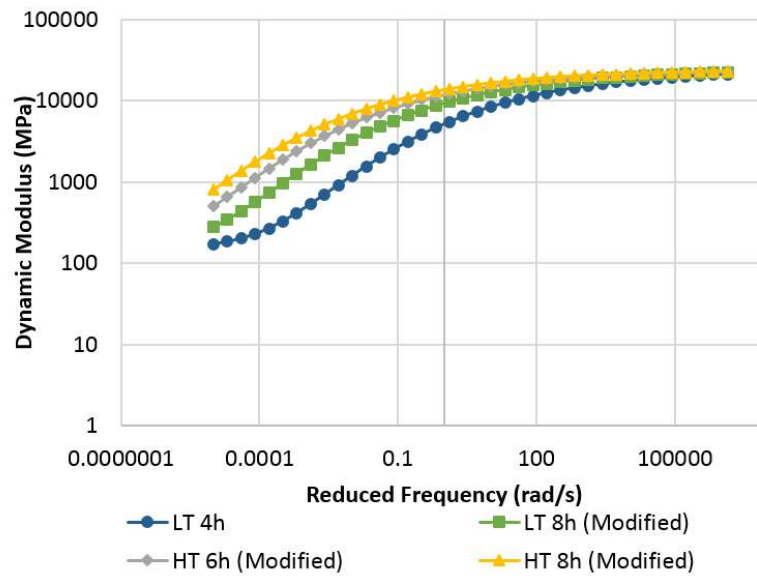


Figure 3.7 Modified Master Curves and Original Master Curve

Then the modified master curves in Figure 3.7 at other aging conditions are horizontally shifted to form a single master curve using Equations 3.8 and 3.9 using the SSE technique. The aging coefficient b (i.e., 0.72), acceleration factor A (i.e., 5.6) and activation energy E_a (i.e., 55 kJ/mol) are then obtained. The determined activation energy

is within the same range as those calculated in (Glover et al. 2014). The final single master curve after the temperature shift and aging shift is shown in Figure 3.8.

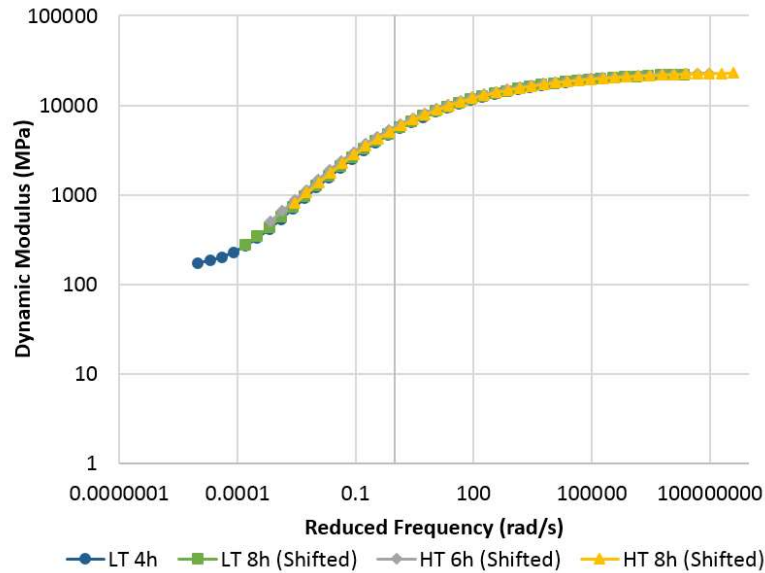


Figure 3.8 Final Single Master Curve after Shift

3.5 Construction of Dynamic Modulus Master Curve of Field Cores

A final dynamic modulus master curve with applying the time-temperature shift and the time-temperature-aging shift is constructed and verified for the LMLC mixtures. In this section, the proposed method is implemented to the field-aged mixtures. Examples are given using the dynamic modulus master curves of HMA. The dynamic modulus master curves of the HMA mixtures at the bottom of the asphalt layer for the four field aging times are shown in Figure 3.9.

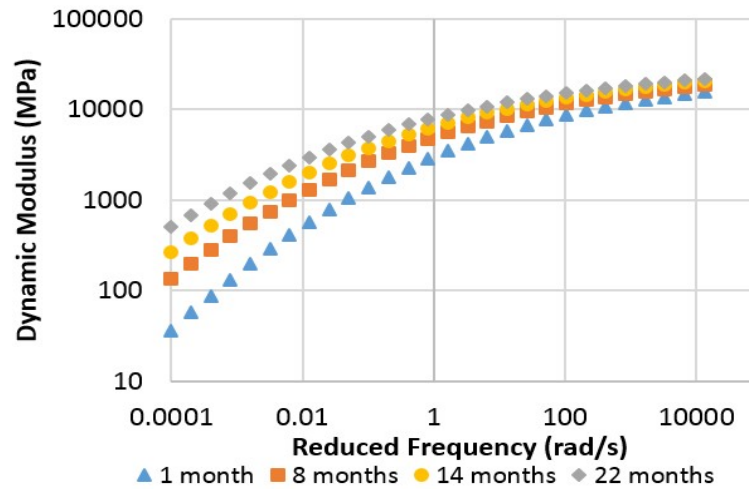


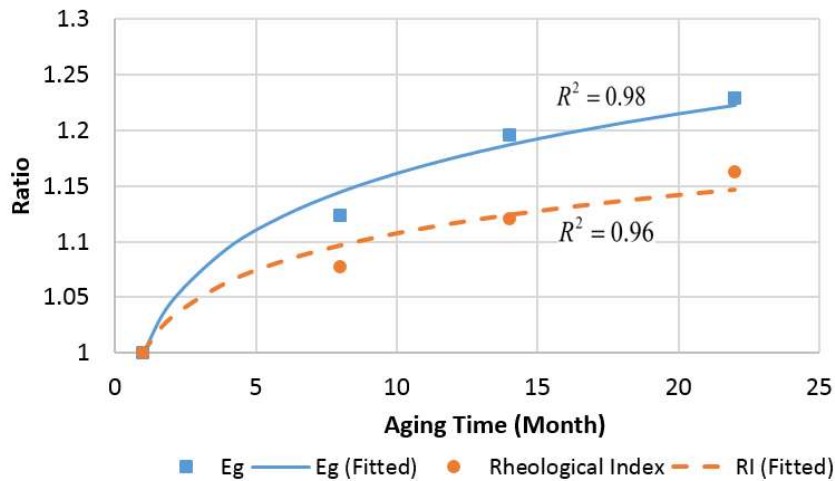
Figure 3.9 Bottom Dynamic Modulus Master Curve for HMA Field Cores

3.5.1 Implementation of Aging Shift Function

In order to construct a final aging master curve, the first step is to determine the aging parameters for field mixtures for the vertical shift and rotation. Figure 3.10(a) illustrates the two ratios of the glassy modulus and rheological index at the bottom of the 8, 14 and 22 months aged mixtures to the values of 1 month aged mixtures and the determination of the exponents for the two functions is defined in Equations 3.6 and 3.7, respectively. The two power curves can be used to predict the glassy modulus and rheological index for the bottom of the HMA mixtures in other aging times outside the ranges of the measurement.

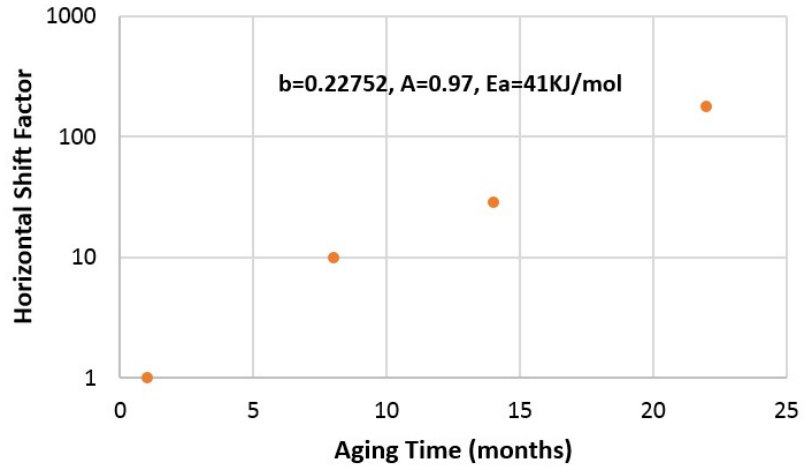
After applying the vertical shift and rotation, the horizontal aging shift factor is determined using Equation 3.8 with known aging times and average field aging temperatures. The corresponding horizontal shift factors for different aging periods are shown in Figure 3.10(b). The power parameters b , acceleration factor A , and the activation

energy E_a in the horizontal shift factor equation are also determined, as shown in Figure 3.10(b). The final aging master curve of the bottom of the asphalt layer is developed after the horizontal shifts of the 8, 14 and 22 months aged master curves, which is presented in Figure 3.10(c). Furthermore, by the same approach, the aging master curves of the top and center of the asphalt layer are obtained after the proposed vertical shift, rotation and horizontal aging shift. The final three aging master curves for the top, center and bottom are shown in Figure 3.10(d).

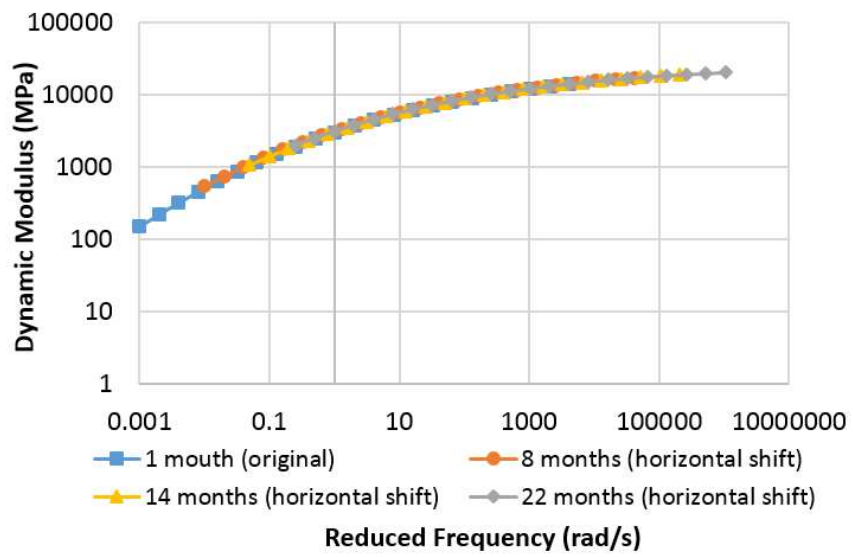


(a)

Figure 3.10 Development of Aging Master Curve for Field Mixtures: (a) Aging Parameter Ratios for FHMA, (b) Horizontal Shift Factors Versus Aging Time, (c) Bottom Aging Master Curve of Field Asphalt Mixtures, (d) Aging Master Curves for Top, Center and Bottom

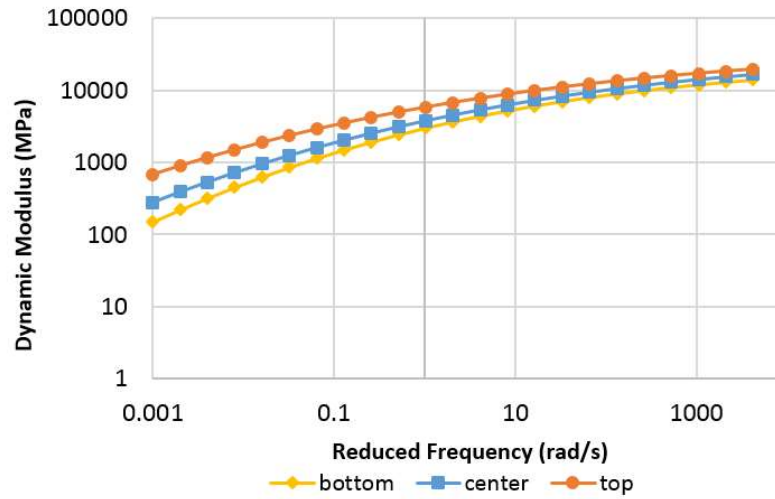


(b)



(c)

Figure 3.10 Continued



(d)

Figure 3.10 Continued

3.5.2 Determination of Horizontal Depth Shift Function

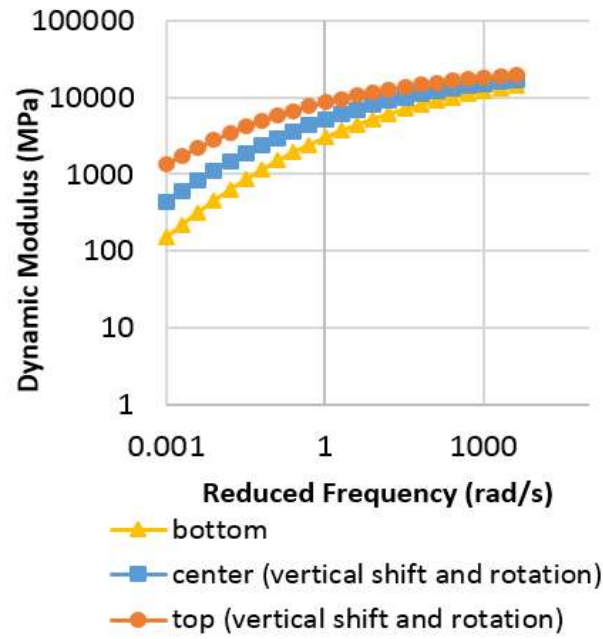
Unlike the LMLC aged mixtures, the dynamic modulus of an asphalt layer also changes with pavement depth for a long-term field aging time due to the non-uniform oxidative aging effect. As shown in Figure 3.10(d), the dynamic modulus master curves at three pavement depths are obviously different. As expected, the magnitude of the master curve at the surface is the largest whereas the master curves for center and bottom of the layer are relatively smaller. In order to take into account this unique aging effect for field-aged mixtures, another shift function is needed to quantify this non-uniform aging. The bottom is selected as the reference pavement depth. Due to the similarities between the non-uniform aging and the long-term aging, it is possible to shift the aging master curves of the surface and center to match that of the bottom. Therefore, a vertical shift and rotation

are needed for this purpose, which can be accomplished using Equations 3.6 and 3.7. Figure 3.11(a) shows the dynamic modulus master curves at the center and top after vertical shift and rotation with the original master curve at the bottom.

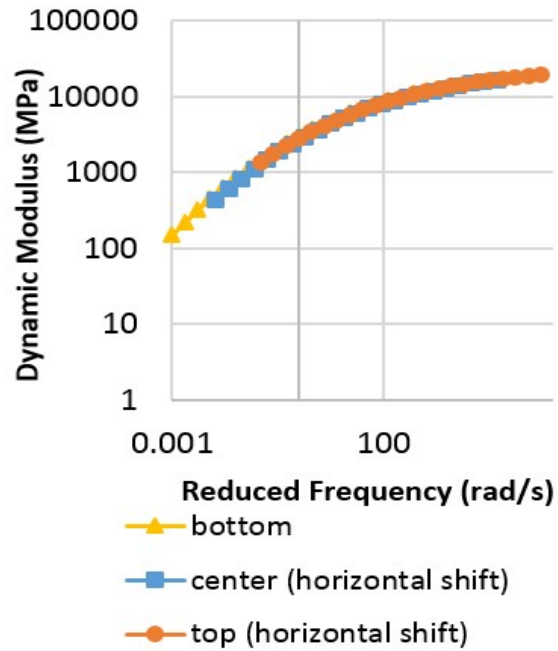
At this stage, the glassy modulus and rheological index for the master curves of top, center and bottom of the layer are identical. A depth shift function is developed to shift the top and center modulus master curves horizontally to the bottom one, which is shown in Equation 3.10:

$$a_d = e^{b_d(d_0-d)} \quad (3.10)$$

where b_d is the fitting parameter for the depth shift function, d and d_0 are the depth of interest and the thickness of the layer, respectively. From shifting the top and center master curves and forming a single master curve using the SSE technique, the value of b_d is determined to be 3.21. The final master curve for the HMA is shown in Figure 3.11(b). After determining the aging shift function and depth shift function, it is possible to predict the dynamic modulus master curve at any depth and any aging time for an asphalt pavement layer. At this point, a final master curve for a field-aged mixture is established after the time-temperature superposition, long-term aging superposition, and non-uniform superposition.



(a)



(b)

Figure 3.11 Application of Depth Shift Function to Top and Center: (a) Vertical Shift and Rotation, (b) Horizontal Depth Shift

3.6 Conclusions

The time-temperature-aging-depth shift functions are developed to characterize the aging viscoelastic properties of asphalt mixtures including the laboratory-aged mixtures and field-aged mixtures. The constructed dynamic modulus master curves at different aging times and pavement depths are used to formulate the two aging shift functions. The following conclusions can be drawn:

- Dynamic modulus master curve is constructed using the modified CAM model. The two CAM model parameters (i.e., glassy modulus and rheological index) are found to be functions of aging time, which are used as the aging parameters;
- In order to construct a single dynamic modulus master curve including the aging effect, vertical shift for changing the glassy modulus and rotation for changing the rheological index at other aging times are necessary before applying the horizontal aging shift factor. This procedure is used to change the higher level of glassy modulus asymptotes and flatter shapes of dynamic modulus master curves of asphalt mixtures due to aging;
- After the determination of the vertical shift and rotation, the modified dynamic modulus master curves at other aging times can be shifted horizontally using the horizontal aging shift factor to the master curve at the reference aging time, which is as effective as the time-temperature shift factor;
- The horizontal aging shift factor is found to be a function of aging time, activation energy, acceleration factor and aging temperature. The aging time effect is modeled as a power law function and the aging temperature effect is determined

based on the Arrhenius equation. The acceleration factor A may be a measure of the laboratory accelerated aging relative to field aging;

- The depth shift factor is developed as a function of pavement depth to account for the non-uniform aging for the field-aged asphalt mixtures. With the aid of the depth shift factor, the dynamic modulus master curve at a given depth can be obtained when the dynamic modulus master curve at the reference depth is known; and
- A final master curve is constructed considering the effects of temperature, long-term aging and non-uniform aging for the field-aged asphalt mixtures. This model can be used for forensic investigation of an *in-situ* asphalt pavement.

It is expected that the asphalt pavement performance can be predicted using the proposed approach. For example, the dynamic modulus master curves at multiple pavement depths and aging times can be calculated and used as the undamaged viscoelastic properties of the asphalt layer in the finite element model to predict the aging effect on the pavement performance. It can also be utilized to evaluate the effect of recycled materials such as Reclaimed Asphalt Pavement (RAP) on the properties of new asphalt mixtures. Due to the limited numbers of LMLC and field core specimens in this chapter, more work should be conducted to account for the different mixture types, climatic regions, asphalt layer thicknesses, and aging times, and to confirm the use of the acceleration factor A .

4. NUMERICAL MODELING AND ARTIFICIAL NEURAL NETWORK FOR PREDICTING J-INTEGRAL OF TOP-DOWN CRACKING IN ASPHALT PAVEMENT[†]

4.1 Overview

Top-down cracking (TDC) is recognized as one of the major distress modes in asphalt pavements. This chapter aims at determining the fracture parameter J -integral of the TDC, which is a critical input to predict the crack growth rate and fatigue life of pavements for this type of distress. Previous research studies demonstrated that the TDC is affected by various factors, including the complex state of high tensile or shear stresses induced by the loading at the edge of or within the tire, material properties such as the modulus gradient in the asphalt layer, moduli of the base and subgrade layers, and pavement structures. In this chapter, the finite element modeling (FEM) is adopted to simulate the propagation of TDC considering different combinations of these essential factors and calculate the J -integral for 194,400 cases. It is shown that the modulus gradient plays an important role in determining the J -integral, and the J -integral is not uniformly distributed within the pavement depth. Based on the database generated from the FEM, six backpropagation Artificial Neural Network (ANN) models including one input layer, two hidden layers and one output layer are developed using the same input variables and output variable as those for the FEM. The R^2 value for each ANN model is more than 0.99,

[†] Reprint with permission from Transportation Research Board of the National Academies: "Numerical Modeling and Artificial Neural Network for Predicting J-Integral of Top-Down Cracking in Asphalt Concrete Pavement." By Meng Ling, Xue Luo, Sheng Hu, Fan Gu and Robert L. Lytton. *Transportation Research Record*, No. 2631, 2017.

which indicates the goodness of fit. After determining the parameters of each ANN model, the J -integral can be predicted for any combinations of the design parameters without reconstructing the FEM.

4.2 Introduction

Top-down cracking (TDC) is recognized as one of the major distress modes in asphalt pavements, and this type of distress has been identified in many countries. Different from the bottom-up cracking (BUC), the TDC initiates from the pavement surface and then propagates downward through the asphalt layer, which is usually observed as the longitudinal crack in or near the wheelpaths (Myers et al. 1998). The traditional pavement analysis for the BUC is not capable of characterizing and predicting the TDC because of different mechanisms between these two distresses. For example, the traditional method normally assumes uniform tire contact stress and a single value of the asphalt layer modulus, then calculates the bottom tensile strain of the asphalt layer to predict the BUC and fatigue life. However, this theory cannot be applied to explain the TDC. Even though the TDC has been studied for decades, there are still few systematic models that have been developed and no general agreement has been reached due to its complexity mainly from the material, climate, traffic and structure factors.

It is known that the TDC is affected by various factors in previous research studies. A complex state of high tensile or shear stress induced by the traffic loading at the edge of or within the tire patch is acknowledged as one important factor. Furthermore, when a tire load is applied on the pavement surface, there are three contact stress components, which are known as vertical stress, transverse stress and longitudinal stress. None of these

stresses are uniformly distributed according to the reported measurements (De Beer et al. 1997). Another crucial factor is the modulus gradient in the asphalt layer. The asphalt layer suffers long-term aging once the pavement is placed, and the stiffness gradient is developed during this period. As a result, the surface of asphalt layer has a higher modulus but normally a lower fracture energy and relaxation property. Accordingly, it becomes more brittle and susceptible to cracking. On the other hand, it is reported that in the high-temperature areas with extreme temperature gradients, the modulus of the asphalt layer even increases with pavement depth. The author concluded that the inverse modulus gradient is also an important factor which contributes to the TDC because of the increasing tensile and shear strains at the surface of the pavement. In addition, the pavement structure and other material properties are also considered as vital factors. This indicates that the thickness of asphalt and base layers and the modulus of base and subgrade layers are the dominant structural factors.

It is clear that a single factor is not capable of characterizing the TDC. Therefore, it is desirable to consider the combinations and interactions of these factors in determining the TDC performance in the asphalt pavement structure. However, conducting a laboratory test is difficult when taking into account all of the variables, such as the thickness of each pavement layer and the modulus gradient. Under this circumstance, the finite element model (FEM) and advanced statistical model become more suitable to predict the propagation of TDC.

The numerical approach is a promising method that has been widely used in evaluating the TDC. In this chapter, the fracture parameter J -integral at the crack tips for

different crack depths, material properties and pavement structures is determined. The J -integral is an energy-based fracture parameter, which is defined as the strain energy release rate. It is similar to the stress intensity factor (SIF), but is not limited to the linear elastic materials and can be experimentally determined (Kuai et al. 2009). Equations 4.1 and 4.2 are normally used to calculate the crack growth rate and J -integral for a fatigue test of asphalt mixtures.

$$\frac{dc}{dN} = A'(J)^{n'} \quad (4.1)$$

$$J = \frac{\partial DSE / \partial N}{\partial CSA / \partial N} \quad (4.2)$$

where

c = crack length;

N = number of loading cycles;

A' and n' = fracture coefficient;

J = J -integral;

DSE = dissipated strain energy for fracture; and

CSA = crack surface area.

On the other hand, the modulus gradient in the asphalt layer induced by aging and temperature is an important factor that was ignored in the previous TDC analyses. In this chapter, the modulus gradient is included. The tire-pavement interactions are simulated based on the previous measurements conducted by De Beer et al. (1997). The effects of different crack depths, modulus for each layer and thickness of the asphalt and base layers are also presented.

In addition to the FEM, the statistical analysis has been proven to be an efficient tool to develop a prediction model in the pavement engineering. The Artificial Neural Network (ANN) is one of the most accurate statistical approaches to predict the material and fracture properties such as the dynamic modulus, the SIF and the distress of asphalt pavements. The reason for choosing the ANN model is that it has some unique advantages including the convenience that the mathematical interacting relationships between various factors do not need to be specified, the capability of learning and training itself from the input and output data, and the high prediction accuracy.

The chapter is organized as follows. The next section demonstrates the three-dimensional (3D) FEM used for determining the J -integral of TDC with the modulus gradient sub-model, loading stresses sub-model, different crack depths and pavement structures. Subsequently, the multilayer backpropagation ANN models are constructed for predicting the J -integral based on the database calculated from the FEM. The last section summarizes the contributions of this chapter.

4.3 Three-Dimensional Finite Element Modeling of TDC

A 3D FEM is developed using the commercial program ABAQUS (2008). A longitudinal TDC is inserted in the middle part of the pavement model to avoid the interference due to the boundary condition. The crack is located in the direction of traffic flow with 1 m long. The J -integral at the crack tips is calculated using different material properties, crack depths and pavement structures, which will be discussed in detail later.

4.3.1 Material Properties of Pavement System

As indicated previously, the modulus gradient plays a key role in the propagation of TDC. Traditionally, in order to consider the modulus gradient, the layered approach is utilized, which is also adopted in the AASHTO design guide. However, it has been shown that the layered analysis is not accurate compared to the continuous gradient analysis and the most significant difference is found at the surface of the asphalt layer (Buttler et al. 2006), which is non-negligible for the analysis of TDC. In this chapter, a user-defined material subroutine (UMAT) is developed using FORTRAN to model the smooth modulus gradient. In the UMAT, the modulus gradient is modeled using Equations 4.3 and 4.4:

$$E(z) = E_d + (E_0 - E_d) \left(\frac{d-z}{d} \right)^n \quad (4.3)$$

$$k = \frac{E_0}{E_d} \quad (4.4)$$

where

$E(z)$ = modulus at depth z ;

E_d = moduli at the bottom of the asphalt layer;

E_0 = moduli at the surface of the asphalt layer;

d = thickness of the asphalt layer;

n = model shape parameter; and

k = ratio of the modulus at the surface to that at the bottom.

Two schematic plots for the typical modulus gradient curves by aging and temperature are shown in Figures 4.1(a) and 1(b), respectively. Figure 4.1(a) shows the modulus gradient for a long-term aging pavement and Figure 4.1(b) demonstrates another

type of modulus gradient for a high air temperature pavement. The viscoelasticity is not considered in the UMAT due to the impractical fact of running a large number of calculations and changing the Prony series parameters of the relaxation modulus in the FEM. However, the temperature dependency and frequency dependency of the asphalt mixtures are taken into account as the surface modulus E_0 and the parameters of n and k can be randomly adjusted in the FEM calculations with the aid of the UMAT.

In terms of the base and subgrade layers, linear elastic properties are assumed for the purpose of simplicity. The details regarding the material properties including the modulus and Poisson's ratio for the three layers will be presented later.

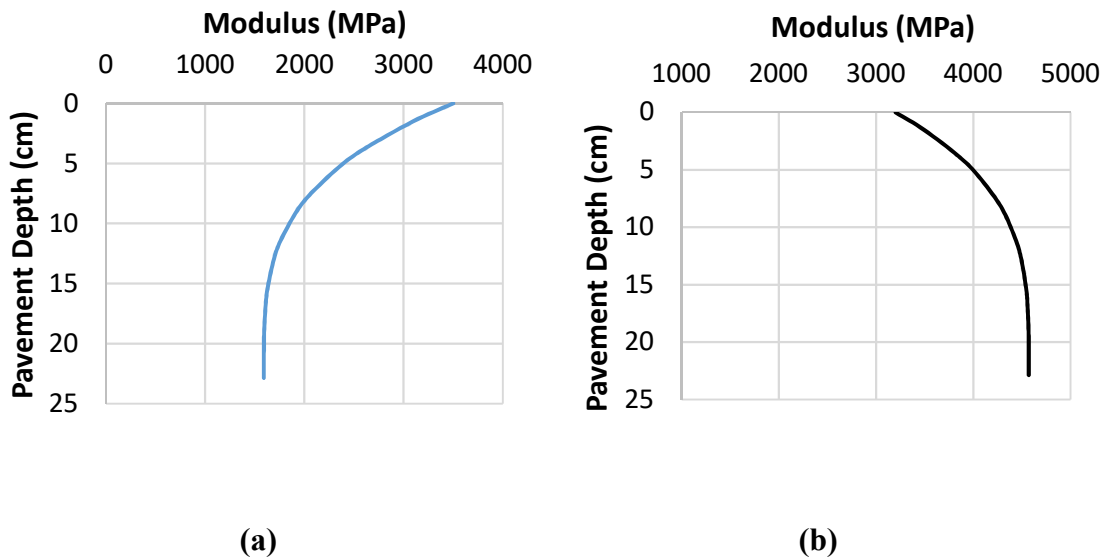


Figure 4.1 Modulus Gradient Curves in Asphalt Layers: (a) Aging, (b) Temperature

4.3.2 Tire-Pavement Contact Stresses

A typical 315/80R22.5 dual tire static loading with a 0.35 m tire spacing is selected. The tire inflation pressure and the constant load on tires are assumed to be 689.5 kPa and

40 kN, respectively. The corresponding contact stresses are decomposed into vertical stress, longitudinal stress and transverse stress, which are non-uniformly distributed. The contact stress patterns of the three types of stresses are shown in Figure 4.2, which are simplified versions of the measurements by De Beer et al. (1997).

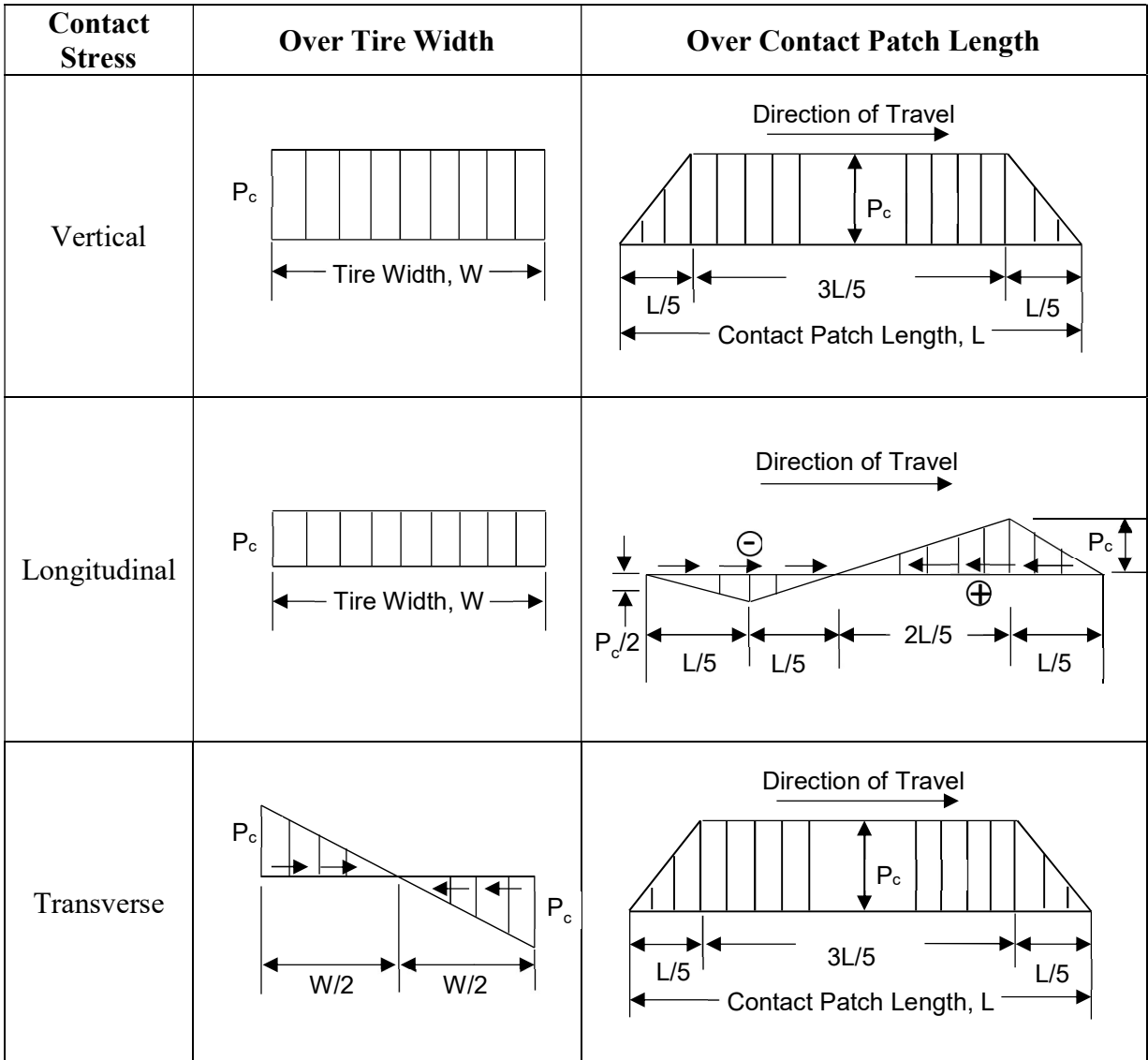


Figure 4.2 Simplified Patterns of 3D Vertical, Longitudinal and Transverse Contact Stresses

The measured maximum contact stress P_c in Figure 4.2 is related to the inflation pressure and tire load through a multiple linear regression analysis, as shown in Equation 4.5.

$$P_C = k_1 + k_2 P_I + k_3 P_L \quad (4.5)$$

where

P_C = maximum contact stress in kPa;

P_I = inflation pressure in kPa;

P_L = tire load in kN; and

k_1, k_2, k_3 = regression coefficients (see Table 4.1).

Table 4.1 Regression Analysis of Tire-Pavement Contact Stress

Tire Type	Data Samples	Contact Stress	Regression Constants and Statistics			
			k_1 (kPa)	k_2	k_3	R^2
315/80R 22.5	89	Vertical	80.4490	0.9021	16.1207	0.92
		Longitudinal	106.2760	0.0129	3.2960	0.84
		Transverse	210.5240	-0.2003	3.0316	0.83

Using Equation 4.5, with the known inflation pressure and tire load, the maximum contact stresses for the vertical, transverse, and longitudinal components are calculated as 1350.7 kPa, 247 kPa, and 193.7 kPa, respectively. The shapes of tire contact areas are assumed to be rectangular rather than circular shapes, according to Lytton et al. (1993). The tire width is 0.315 m, and the tire length is calculated based on Equation 4.6:

$$l = \frac{P_L}{P_I \times w} \quad (4.6)$$

where w is the tire width and l is the tire length. The tire length is determined to be 0.19 m. Based on the calculation results, the three stresses determined in one loading area are shown in Figures 4.3(a) to 4.3(c), respectively. The combination of the three stresses used in the FEM is illustrated in Figure 4.3(d). It should be noted that there are another two lengths for the dual tires loading and another three different lengths of the single tire loading, which are also determined for representing the different inflation pressures.

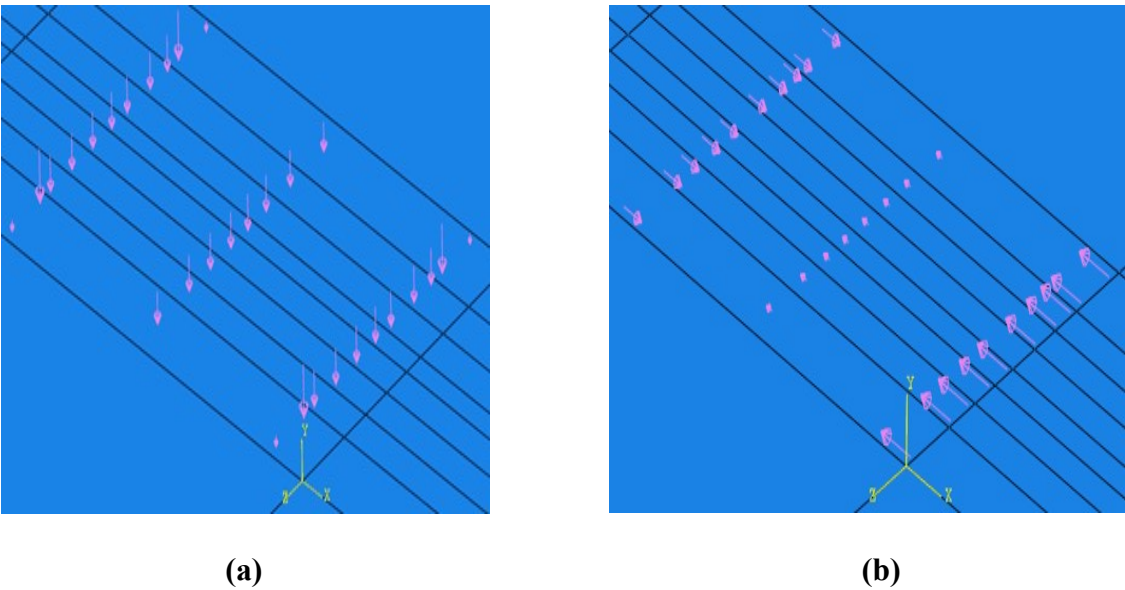


Figure 4.3 Three Components of Tire-Pavement Contact Stress in ABAQUS: (a) Vertical Contact Stress, (b) Transverse Contact Stress, (c) Longitudinal Contact Stress, (d) Combination of Contact Stresses

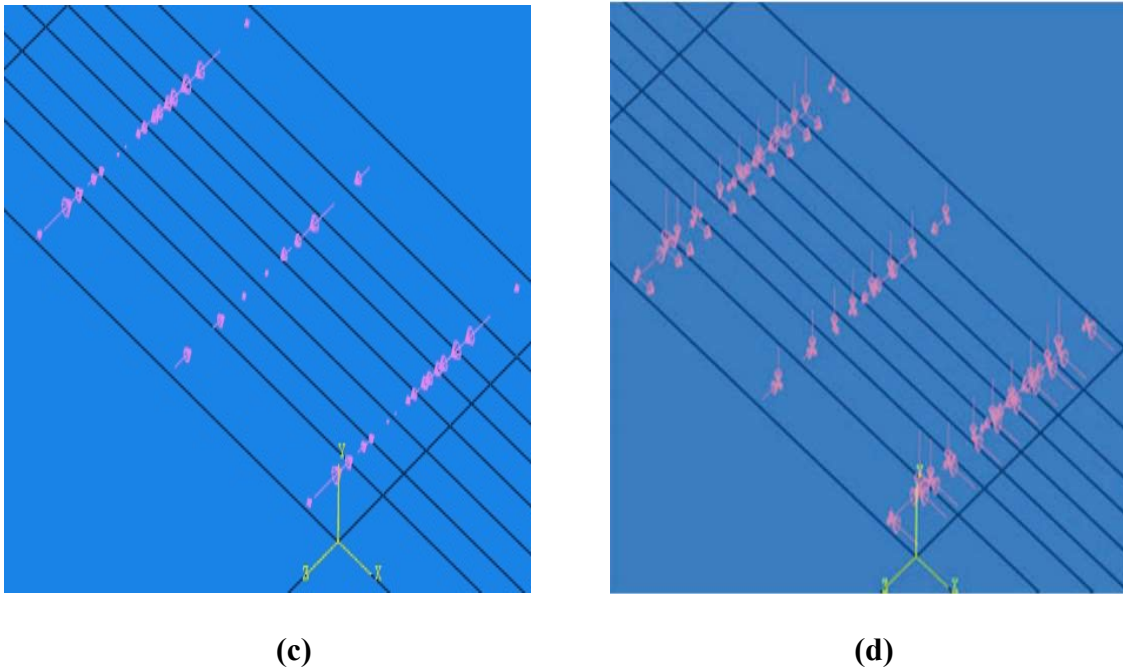


Figure 4.3 Continued

4.3.3 Pavement Structure, Mesh and Boundary Conditions

The length and width of the 3D model are 6 m and 3 m, respectively. The thicknesses of the asphalt and base layers are adjusted for the possible ranges and the purpose of determining the thickness effect on TDC. The boundaries for the four surrounding sides of the 3D model are fixed in the x and z directions and bottom side is fully fixed, and sliding is not allowed between layers.

Different ratios of crack depth to asphalt layer thickness (TDC ratio) are considered in the FEM. Four crack locations relative to the tire loading are analyzed to determine the most critical one. The first location is at the edge of tire but outside of the two load patches, the second one is at the edge of the load between the two load patches, the third one is in the center between the load patches and the fourth location is in the

center of the load. Table 4.2 shows all the inputs including the pavement structures and material properties that are used in the FEM.

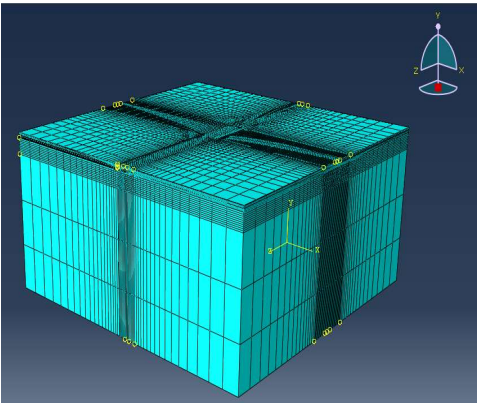
Table 4.2 Materials and Structures Inputs in the FEM

Layer Type	Thickness (mm)	TDC Ratio	TDC Location	Poisson's Ratio	Layer Modulus (MPa)			
					n	k	Surface modulus	
Asphalt Layer	25,75, 125, 200,300, 500	1/10, 3/10, 1/2, 7/10, 9/10	4	0.35	Modulus Gradient	0.5, 2, 5	0.5, 1.2, 2.5	500, 2000, 8000, 30000
Base	150,300, 500	na	na	0.40	Elastic Modulus	150, 300, 600, 7000, 14000		
Subgrade	na	na	na	0.40		30, 150		

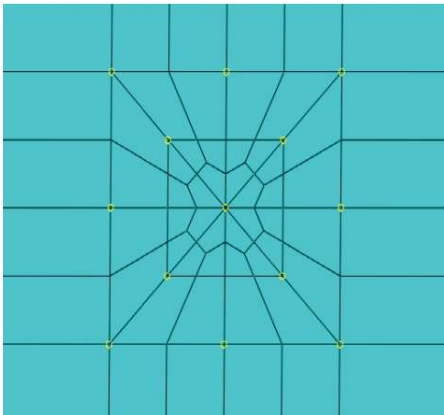
NOTE: na= not applicable.

Figure 4.4(a) shows the 3D FEM model with meshes developed in this chapter. The meshes for the crack and loading area are shown in Figure 4.4(b) with four crack locations, and the meshes for the crack front are magnified and shown in Figure 4.4(c). Eight-node linear brick continuum elements with reduced integration (C3D8R) are used in the model. Fine meshes are used in the vicinity of crack, loading area and asphalt layer whereas coarse meshes are used far away from these areas. To consider the $1/\sqrt{r}$ singularity of the crack tips, 1/4 is used as the midside node parameter, and the degenerate element at crack tips has a single node with a collapsed side element. Sensitivity analysis of the mesh density and size is conducted to ensure both the accuracy and efficiency of the FEM model. A total of 35 nodes are assigned along the crack length; meanwhile, 6

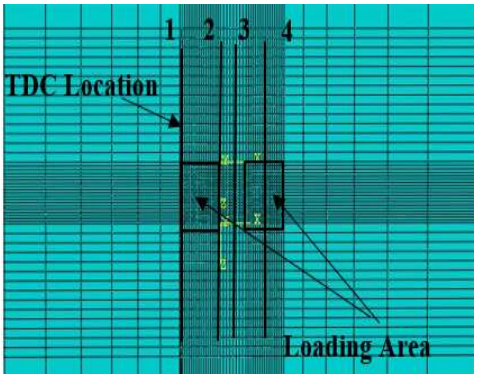
nodes in width and 11 nodes in length are assigned in each of the two rectangular loading areas. The element thickness for the top asphalt layer and the crack area are 15 mm and 2.5 mm, respectively. The area of an element in the crack and loading area is 30 mm × 30 mm and there are gradient changes of the meshes from the crack and loading area to other areas. The corresponding single bias for the other parts are 80 mm to 500 mm beginning from the crack location.



(a)



(b)



(c)

Figure 4.4 3D FEM Model and Mesh Details for TDC and Loading: (a) 3D FE Pavement Model, (b) Magnified Mesh View of Crack Front, (c) Meshes in Crack and Loading Areas

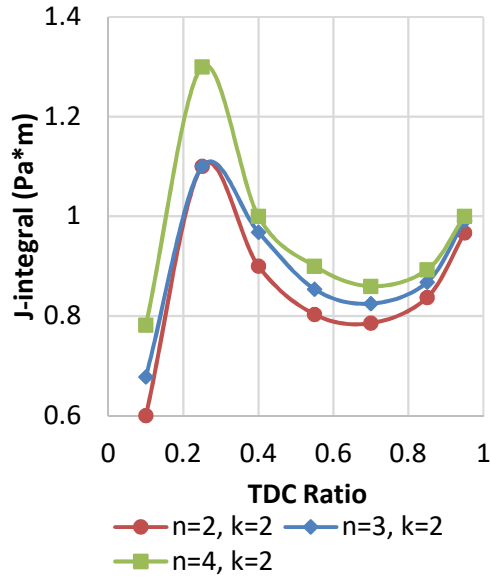
4.3.4 Numerical Simulation Results

The criteria for the most critical location is to identify the highest J -integral value, which is the output of the FEM. The crack location 4 is found to be the most critical one and the J -integral of location 2 has relatively smaller values but is greater than those of locations 1 and 3. This means that when the load is applied on the surface, the crack at the center or at the edge between the two load patterns is more prone to propagate. Therefore, location 4 is chosen as the default location to calculate the maximum J -integral in this chapter.

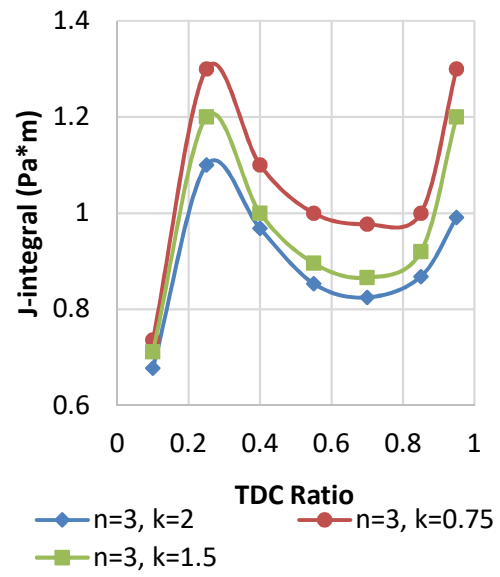
After determining the critical location, the analysis based on the different combinations of pavement materials properties, pavement structures, traffic loading, and crack depths are conducted. Examples of the J -integral within pavement depth are shown in Figures 4.5(a) to 4.5(c) for different modulus gradient parameters of n , k and asphalt layer thickness. The thickness of asphalt layer is 200 mm in Figures 4.5(a) and 4.5(b), and the values for n and k are 3 and 2 in Figure 4.5(c). It can be seen that the J -integral is not uniformly distributed within the asphalt layer. The shape of the J -integral curve is highly dependent on the thickness of asphalt layer and the modulus gradient parameters n and k . As seen in Figure 4.5(a), the J -integral sharply increases from the surface to approximately one third of the layer thickness, which means the crack can propagate easily near the surface. After the peak point, the J -integral decreases, which indicates that more energy is needed to continue to propagate the crack until about two thirds of total thickness is reached. In this part, the crack propagation rate is relatively slow. For the last one third part, the pavement becomes prone to crack again since the J -integral starts to increase.

These simulation results match the field observations of TDC, which indicates that most of the TDCs are observed in the approximately the top one third of the asphalt layer (1). As seen from Figure 4.5(b), a larger value of k results in a smaller J -integral, which is consistent with the definition of the J -integral. For a thicker asphalt layer in Figure 4.5(c), the ratio of crack depth to asphalt layer thickness for the critical crack location is smaller, which means that the critical crack locations are relatively concentrated near the surface of asphalt layers for all the conditions and less related to the thickness of the asphalt layer. It is believed that increasing the thickness of asphalt layer is helpful to reduce the propagations of pavement cracking, however, after the long-term aging period and traffic loading, the surface layer becomes more brittle, and more cracks initiate at the surface rather than at the bottom. It is also found that the shapes of modulus gradient (n and k) within the asphalt layer have a significant effect on the distribution of J -integral and it also confirms that assuming a uniform asphalt layer modulus is not appropriate for accurately predicting the TDC.

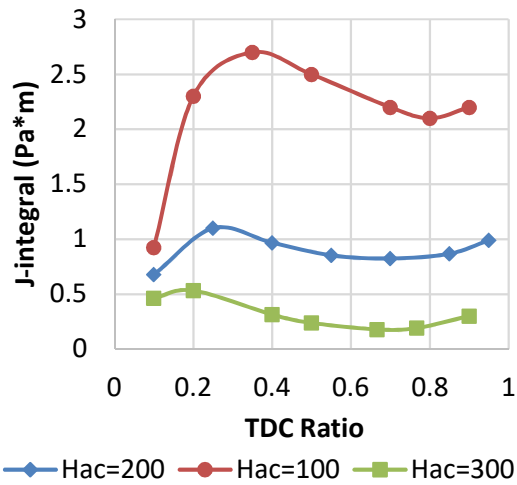
Based on the different combinations of all of the variables in the FEM, there are 194,400 cases needed to be determined. Because of the large number of calculations, the technology from SA-CrackPro is utilized to change the values of all the variables in the FEM model automatically. This method is not reported here, interested readers can consult this reference (Hu et al. 2008). The calculation results for 194,400 cases are obtained, which are used in the ANN modeling for predicting the J -integral at any given pavement depth and pavement condition.



(a)



(b)



(c)

Figure 4.5 J-integral in Pavement Depth with Various Values of n, k and Asphalt Layer Thickness: (a) Different n, (b) Different k, (c) Different Asphalt Layer Thickness

4.4 Artificial Neural Network Modeling Of J-Integral

4.4.1 Background and Preparation of ANN

The second task is to construct the ANN models for accurately predicting the J -integral of TDC. The ANN models are developed using the commercial program MATLAB (1998). The independent variables are the pavement structures (i.e., thickness of asphalt layer H_{ac} and thickness of base layer H_{base}), modulus gradient parameters (i.e., n and k), material properties (i.e., moduli of the surface of asphalt layer E_{ac} , base layer E_{base} and subgrade layer $E_{subgrade}$), the loading conditions (i.e., tire lengths and tire types) and crack depths. The tire lengths and tire types are used to divide the numerical calculation results into different sets. In all, there are 8 variables that are used as the inputs in the ANN model and the J -integral is the output of the ANN model.

In the database, three sets are combined for the single tire loading including three different tire lengths and another three sets are grouped for the dual tires loading of another three tire lengths. For each of the six datasets for the ANN modeling, all of the input variables are normalized to the range of -2 to 2 which are the components in the input layer, and the output variable is normalized to the range of -1 to 1, which is the component in the output layer. The data are randomly divided into a training dataset and a validation dataset before conducting the analysis. The ratio of the training dataset to validation dataset is 4:1. The training dataset is used to develop and train the ANN models and the validation dataset is used to test the statistical accuracy and avoid the overfitting of the ANN models. The architecture of the ANN model used in this chapter is shown in Figure 4.6.

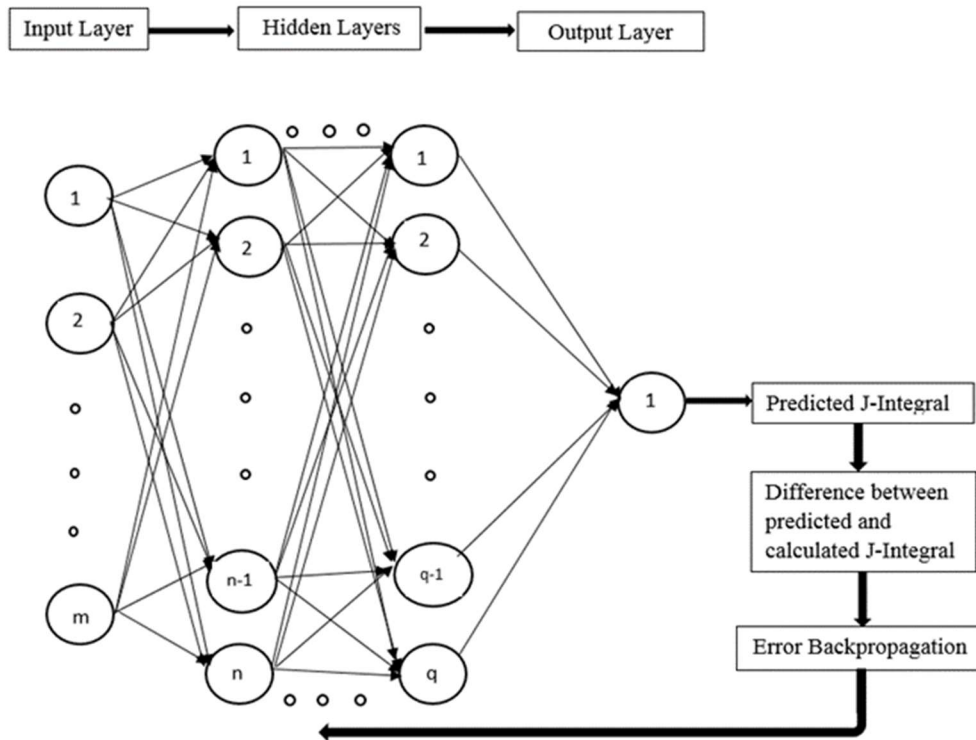


Figure 4.6 Structure of Artificial Neural Network

4.4.2 Development and Algorithm of ANN

In the ANN algorithm, there are no specific rules to determine the types of activation functions for the hidden layers and output layer, the numbers of hidden layers, and the number of neurons in each layer. Based on the literature and required accuracy of the ANN model, a two hidden layers system (1-2-1) is employed. It should be mentioned that for some other cases with much smaller database, the 1-1-1 system is enough to save the computation efforts. The input layer contains the eight independent variables, the two hidden layers include the corresponding weights, bias terms and activation functions, and an output layer includes the output and the corresponding weights and bias terms. The

output of the ANN model is calculated using Equation 4.7. Based on the converged mean square error (MSE) and the computation time compared with different structures and activation functions, a total of 60 neurons are used in each hidden layer. The activation functions for the output layer and two hidden layers are pure linear function and log-sigmoid functions, which are shown in Equations 4.8 to 4.10.

$$J = A_0 \left\{ \sum_{k=1}^q W_k^0 A_{hk} \left[\sum_{k=1}^q W_{jk}^{2h} A_{hj} \left(\sum_{k=1}^q W_{ij}^{1h} P_i + b_j^{1h} \right) + b_k^{2h} \right] + b_0 \right\} \quad (4.7)$$

$$A_0 = x \quad (4.8)$$

$$A_{hj} = \frac{1}{1 + e^{-x}} \quad (4.9)$$

$$A_{hk} = \frac{1}{1 + e^{-x}} \quad (4.10)$$

where i, j and k are the subscripts for the input layer, first hidden layer and second hidden layer, respectively; m, n and q are the numbers of inputs (8), nodes in the first hidden layer (60) and the nodes in the second hidden layer (60), respectively; A_0, A_{hj} and A_{hk} are the activation functions for the output layer (i.e., pure-linear), the first hidden layer (i.e., log-sigmoid); and the second hidden layer (i.e., log-sigmoid); W_{ij}^{1h}, W_{jk}^{2h} and W_k^0 are the weight factors for the first hidden layer, the second hidden layer and the output layer; b_j^{1h}, b_k^{2h} and b_0 are the bias factors for the first hidden layer, second hidden layer and the output layer; P_i is the input variables, J is the output of J -integral.

As a widely used supervised learning algorithm, the backpropagation ANN is chosen in this chapter, which means that once the network is trained the signal will come back to update the initial weights and bias to reduce the calculation errors, as shown in

Figure 4.6. There are several backpropagation algorithms available in MATLAB. After evaluating the convergence of each algorithm, only the Levenberg-Marquardt backpropagation (trainlm function in MATLAB) is suitable to obtain the desired prediction results. The learning function also needs to be determined. In general, different learning functions have similar error performance, but the differences of computation times between the learning functions are relatively large. Based on comprehensive comparisons, the gradient descent weight/bias learning function (learngd function in MATLAB) is employed as the learning function in the ANN model. To ensure the convergence and performance of the ANN model, several other model parameters are also considered in the training. Based on the literature and trial and error, the following parameters including the epochs between displays, learning rate, the maximum number of epochs for training, and the performance goal are determined as 0.05, 0.9, 400, 1e-4, respectively.

A total of six ANN models for different traffic loading conditions are successfully developed based on the above technique. The models are further evaluated using the determination coefficient R^2 . As seen from Figure 4.7, all the R^2 values are above 0.99, indicating the accuracy of the model predictions. Once the ANN models are determined, the important parameters including the normalized inputs and output, weights information and network information are extracted from the ANN models. With these parameters, users can predict the J -integral under any given pavement and loading conditions.

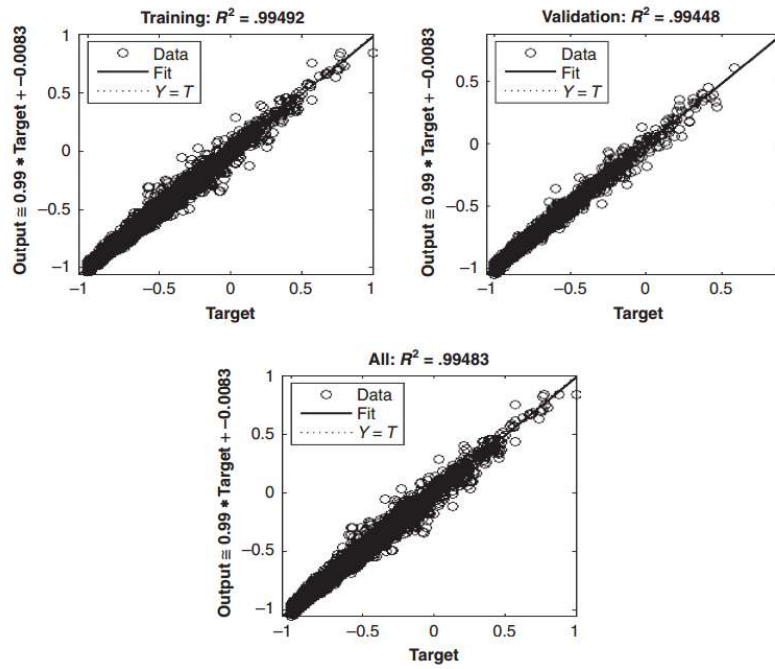
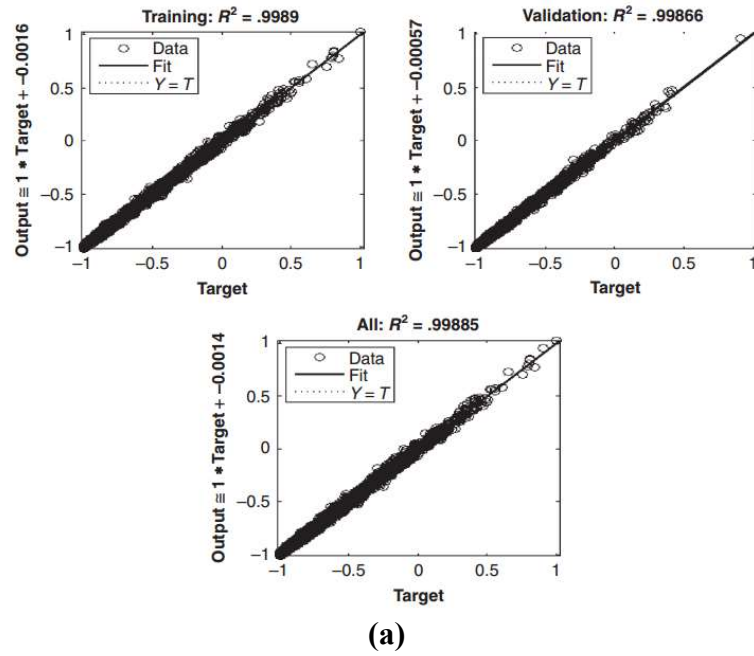
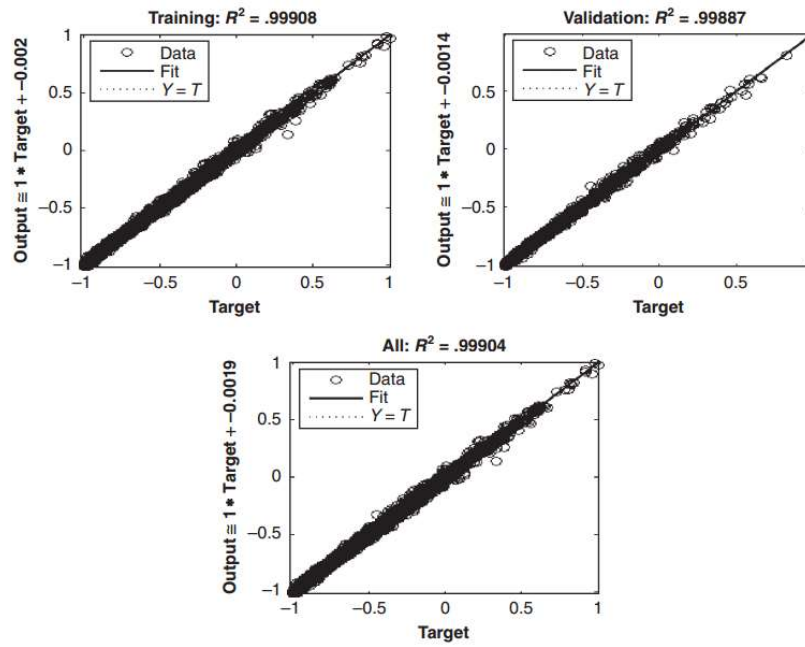
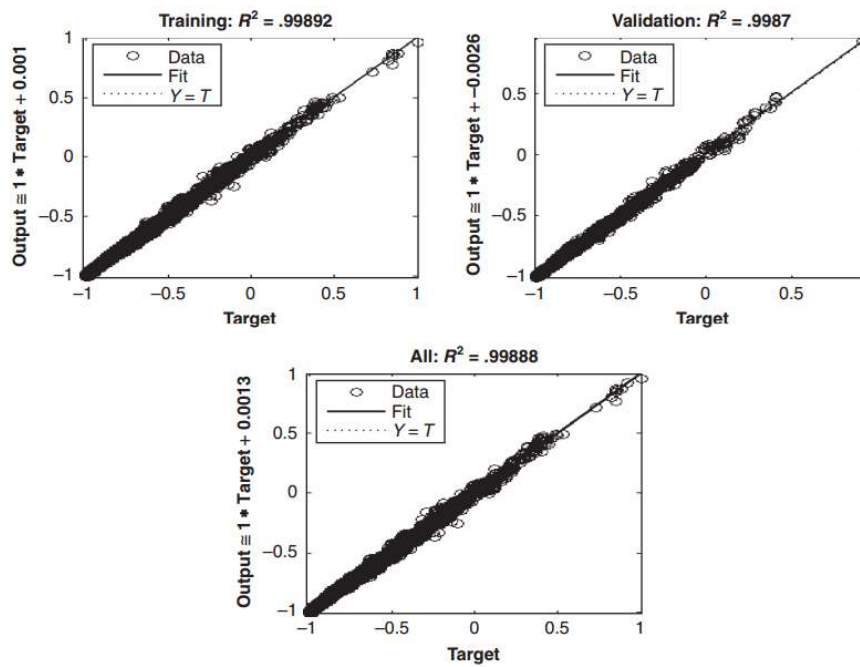


Figure 4.7 Measured and Predicted J-integral for Training, Validation, and Overall Datasets for Dual and Single Tire Loadings: (a) Dual Tire Length of 19 mm, (b) Dual Tire Length of 185 mm, (c) Dual Tire Length of 229 mm, (d) Single Tire Length of 64 mm, (e) Single Tire Length of 305 mm, (f) Single Tire Length of 406 mm

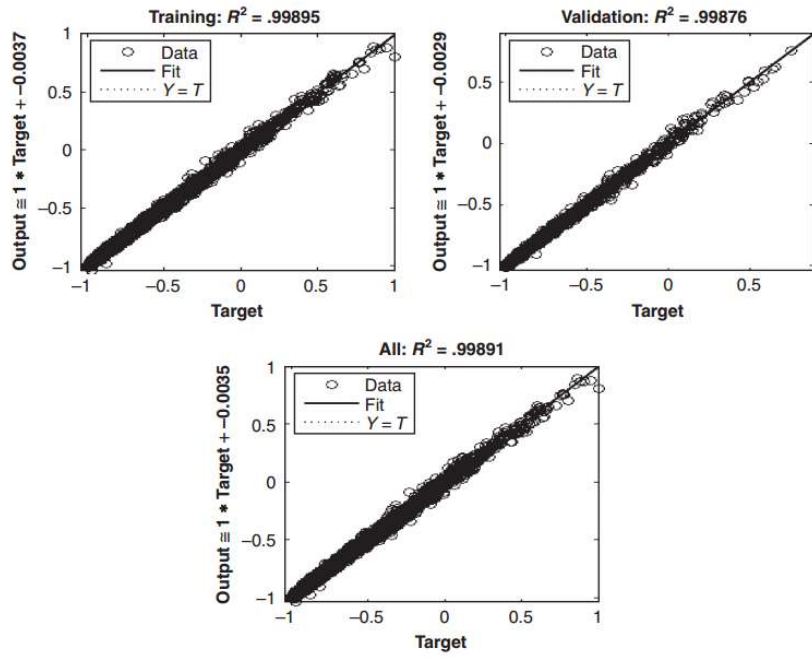


(c)

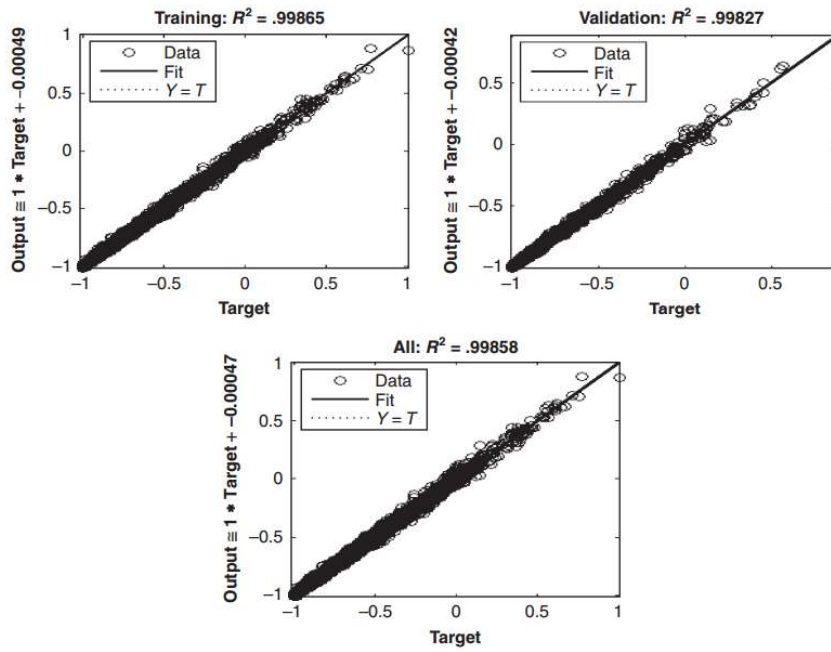


(d)

Figure 4.7 Continued



(e)



(f)

Figure 4.7 Continued

4.5 Conclusions

This chapter presents the constructions of a 3D FEM model and an ANN model for predicting the J -integral of TDC considering the modulus gradient of asphalt layer, different moduli of base and subgrade layers, pavement structures, load patterns, load locations, and crack depths. A total of 194, 400 cases are computed based on the combinations of these factors from the FEM. These results are used as the database for developing the ANN models. The ANN models are designed as the four-layer backpropagation architecture, including one input layer, two hidden layers and one output layer. The input layer consists of eight variables, which are the same as those used in the FEM models and the output layer has one variable J -integral, which is also the output of the FEM. The following contributions and findings are drawn:

- The J -integral is not uniformly distributed within the depth of asphalt layer. Specifically, there is a peak value at approximately one third of the layer thickness, which means that the TDC can propagate fast near the top surface until reaching the peak point;
- A UMAT is developed to characterize the modulus gradient in asphalt layer. The calculation results indicate that the modulus gradient is an important factor contributing to the propagation of the TDC. Meanwhile, the modulus gradient induced by aging and temperature should not be ignored in the pavement analysis;
- The developed ANN models have been proven to be efficient tools and the prediction accuracy is remarkably high. Once the ANN models are developed,

users can input the parameters of the pavement structures and material properties to predict the J -integral without reconstructing the 3D FEM model.

The sensitivity analysis for all of the input parameters is conducted and shown in Appendix C. The predicted J -integral will be used in the Paris' law to determine the crack growth rate of TDC and the fatigue life of the pavements. Meanwhile, with the aid of the data of the longitudinal cracking in the wheelpath from the LTPP database incorporated with the temperature and traffic data, a general TDC model can be determined and calibrated to the observed performance.

5. DEVELOPMENT OF A CALIBRATED AND VALIDATED MECHANISTIC-EMPERICAL TOP-DOWN CRACKING MODEL

5.1 Background

Two types of top-down cracking (TDC) are identified in asphalt pavements, one is the constructed-related TDC, and the other is the load-related TDC. The constructed-related TDC is mainly due to the segregation of aggregate due to poor construction quality (Harmelink et al. 2008). The locations of this TDC type are normally on the outside edges of the two slat conveyors or under the gearbox between the two slat conveyors. The load-related TDC is usually developed in the wheelpath, which is mainly caused by non-uniform contact stress, thermal stress and field aging process. It should be mentioned that in this dissertation, only the load-related longitudinal TDC in the wheelpath is discussed. The objective of this chapter is to develop several sub-models such as the load spectra model, crack initiation model, crack propagation model, thermal stress model and endurance limit model, then assemble other sub-models developed in the previous chapters such as the aging model and ANN model to develop a general TDC prediction model. Moreover, the TDC model is calibrated and validated using the LTPP data.

5.2 LTPP Data Collection

The pavement data is collected from the LTPP database to cover four major climatic zones in the United States. The material properties of different layers (i.e., asphalt layer, base layer, subgrade layer or any other sub-layers), pavement structure, traffic load, and climatic condition of each pavement section are taken into account to develop a

calibrated and validated mechanistic-empirical TDC model. The four climatic zones are known as wet-freeze zone (WF), wet-no freeze zone (WNF), dry-freeze zone (DF), and dry-no freeze zone (DNF). The distribution of the selected LTPP sections shown in Figure 5.1 within the North America that are used to develop, calibrate and validate the TDC model.

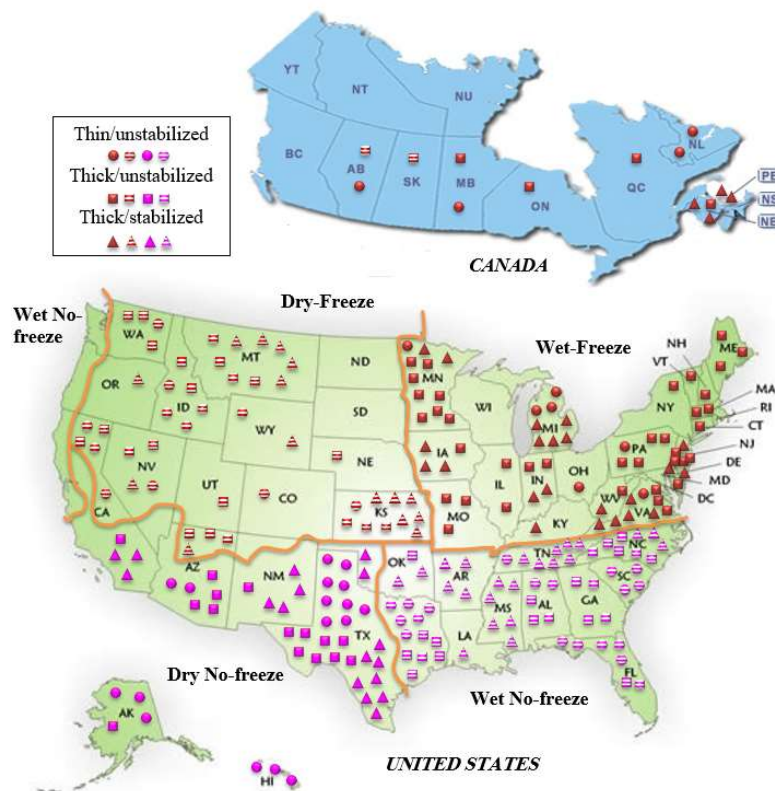


Figure 5.1 LTPP Sections in Four Climate Zones

Specifically, the collected LTPP data should include the following information to ensure the quality of the data: construction time and weather history of each LTPP section; thickness of each layer of the pavement; mixture designs and material properties including the aggregate gradation, binder performance grade, binder content and air void content of

asphalt layer, moduli of base and subgrade layers; traffic loading such as the classification of vehicles and the axle load distribution (load spectrum). Pavement distress data (longitudinal cracking in the wheelpath) for different survey times from traffic opening is also collected for three severity levels defined in the LTPP manual (low, medium and high).

5.2.1 Pavement Material and Structure Data

The pavement structure data consists of the thickness and material property of each layer. The volumetric properties and binder properties are used to predict the unaged material property of asphalt layer. The binder property is characterized using the binder CAM model (glassy modulus G_g , crossover frequency ω_R , rheological index R , temperature T_d , and two parameters C_1 and C_2 in the WLF time-temperature shift function), as well as the binder content. The aggregate gradation is also a necessary input, which includes the percentages of passing 3/4, passing 3/8, passing #4, and passing #200. With the above aggregate and binder properties, two ANN models including the Witczak's 1999 and 2006 models are utilized to estimate the unaged dynamic modulus of the asphalt layers. The asphalt pavement system is categorized into five types, which is on the basis of the thickness of asphalt layer and treatment of base course: thin-unstabilized, thick-stabilized, thick-unstabilized, inter-unstabilized and inter-stabilized. Specifically, the thin-unstabilized structure is defined as the thin asphalt layer (less than 102 mm or 4 inches) on the unstabilized base course, thick-unstabilized structure is defined as the thick asphalt layer (greater than 203 mm or 8 inches) on the unstabilized base course. Thick-stabilized

structure is named as the thick asphalt layer on the stabilized base course. Inter-unstabilized and inter-stabilized layers are defined as the pavement structures with asphalt layer thickness between 102 mm to 203 mm (4 and 8 inches) with the unstabilized and stabilized base, respectively.

5.2.2 Characterization of Traffic Loads

Traffic load is an essential input in the pavement design and analysis. The traffic load including the Weigh-In-Motion (WIM) data and Average Annual Daily Truck Traffic (AADTT) data is collected from LTPP database for each pavement section, if both of types are available. The traffic load is characterized using a load spectrum model for each axle type (single, tandem, tridem and quadrem axle), traffic category, vehicle class (from vehicle classes 4 to 13) and the number of tires (single and dual tires). The traffic load can also be presented using the AADTT with a default traffic load distribution when the WIM data is not available.

In this study, the annual load traffic is modeled in two levels. Level one is based on the WIM data, which can be used to characterize the actual axle load distribution for each tire type and axle type. The AADTT is also available in the LTPP database, which is utilized as the level two for the traffic data modeling. It should be noted that the AADTT is an average number so that it lacks some accurate information such as the actual load distribution (load spectra) of each pavement section is unknown. The estimation of load distribution based on the AADTT will be discussed later. As mentioned before, there are 13 vehicle classes based on the Federal Highway Administration (FHWA) standard. Since

vehicle classes from one to three are regular light passenger vehicle types, only the truck traffic from vehicles classes 4 to 13 are taken into account, which contribute significantly to the initiation and propagation of TDC. The vehicle class and description from 1 to 13 are presented in Figure 5.2.








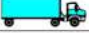





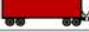




















Class 1 Motorcycles		Class 7 Four or more axle, single unit	
Class 2 Passenger cars		Class 8 Four or less axle, single trailer	
			
			
			
Class 3 Four tire, single unit		Class 9 5-Axle tractor semitrailer	
			
			
Class 4 Buses		Class 10 Six or more axle, single trailer	
			
		Class 11 Five or less axle, multi trailer	
Class 5 Two axle, six tire, single unit		Class 12 Six axle, multi-trailer	
			
		Class 13 Seven or more axle, multi-trailer	
			
			
			

Figure 5.2 FHWA Vehicle Category Classification (FHWA 2013)

The axle load distribution is termed as the distribution of number of loads in an interval of a certain axle load range for a specific vehicle class. The number of loads are measured and recorded from the WIM sensors, and this detailed information is available in the LTPP database for some pavement sections. Furthermore, a total of four different axle types are utilized in this study and the corresponding axle load intervals are different,

which is shown in Table 5.1. The four different axle types are single, tandem, tridem and quad axles, respectively.

Table 5.1 Characteristics of LTPP Axle Type

Axle Type	Minimum Load (lb.)	Maximum Load (lb.)	Load Interval (lb.)
Single Axle	3,000	40,000	1,000
Tandem Axle	6,000	80,000	2,000
Tridem Axle	12,000	102,000	3,000
Quadrem Axle	12,000	102,000	3,000

As can be seen from Table 5.1, each axle loading is composed of vehicle classes 4 to 13. The single axle load of LTPP section 09-0960 is given as an example in Table 5.2 to show the collected axle load distribution. The distributions from vehicle classes 4 to 7 and 8 to 13 are plotted in Figures 5.3 and 5.4, respectively, which are corresponding to categories one and two traffic loading.

Table 5.2 Example of Single Axle Load Distribution

Axle Load (lb.)	Vehicle Class									
	4	5	6	7	8	9	10	11	12	13
3000	0	1671	0	0	246	1563	0	4	0	0
4000	2	17902	5	0	426	5063	2	91	2	0
5000	5	23244	34	0	1205	1057	9	231	41	0
6000	12	20386	78	5	1692	1152	8	201	288	19
7000	220	16958	99	5	2201	761	10	164	90	17
8000	444	23716	447	45	4622	3300	28	268	39	29
9000	288	15541	1284	46	10325	14210	89	407	134	9
10000	592	12803	2414	159	11638	34351	293	803	347	53
11000	960	7429	2262	157	3542	27916	287	350	108	86

Table 5.2 Continued

Axle Load (lb.)	Vehicle Class									
	4	5	6	7	8	9	10	11	12	13
12000	1595	6274	3428	238	3288	22828	266	344	56	104
13000	1360	3538	3510	158	2763	3546	93	242	41	56
14000	2221	3337	5027	195	3077	1033	111	269	52	50
15000	2242	2590	3313	245	1965	723	53	244	42	28
16000	1200	1730	1105	202	1200	733	22	107	18	24
17000	565	1539	485	185	1036	1351	26	97	22	17
18000	163	907	227	159	648	1219	14	62	6	13
19000	94	804	278	115	614	1297	7	40	5	14
20000	54	510	164	133	303	566	2	20	1	11
21000	58	503	91	114	272	372	0	11	0	5
22000	18	326	27	30	118	117	0	9	0	1
23000	9	284	13	16	96	48	0	1	0	3
24000	7	144	4	8	43	11	0	5	0	1
25000	8	104	4	3	44	15	0	0	0	0
26000	7	46	1	3	19	2	0	0	0	0
27000	10	21	0	0	16	1	0	0	0	0
28000	3	10	0	0	8	2	0	0	0	0
29000	10	9	0	0	9	1	0	0	0	0
30000	3	8	1	0	9	3	0	0	0	1
31000	0	5	0	0	0	0	0	0	0	0
32000	3	5	0	0	0	4	0	0	0	0
33000	0	0	0	0	0	2	0	0	0	0
34000	0	0	0	0	0	0	0	0	0	0
35000	0	0	0	0	2	0	0	0	0	0
36000	0	1	0	0	0	0	0	0	0	0
37000	0	0	0	0	0	0	0	0	0	0
38000	0	0	0	0	0	0	0	0	0	0
39000	0	0	0	0	0	0	0	0	0	3
40000	0	0	0	1	5	0	0	0	0	4
Total	12153	162345	24301	2222	51432	123247	1320	3970	1292	548

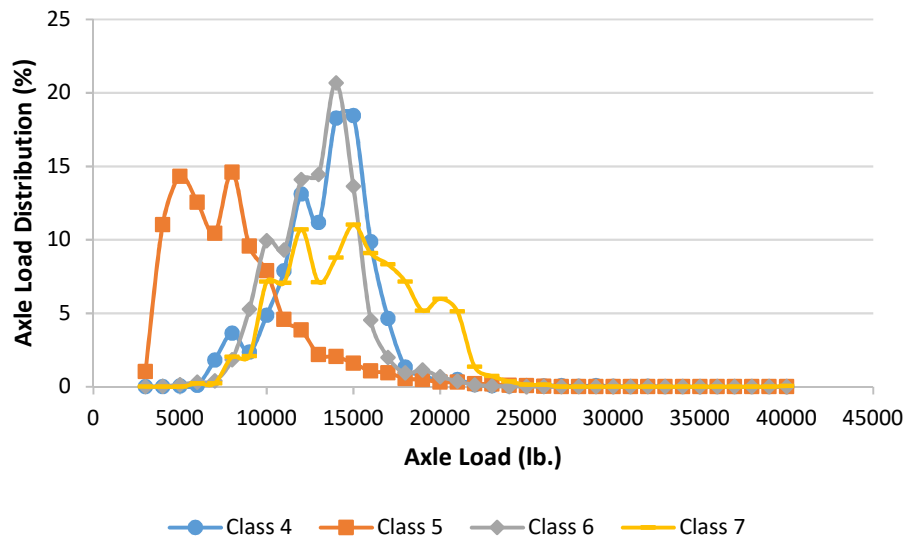


Figure 5.3 Single Axle Load Distribution for Category One

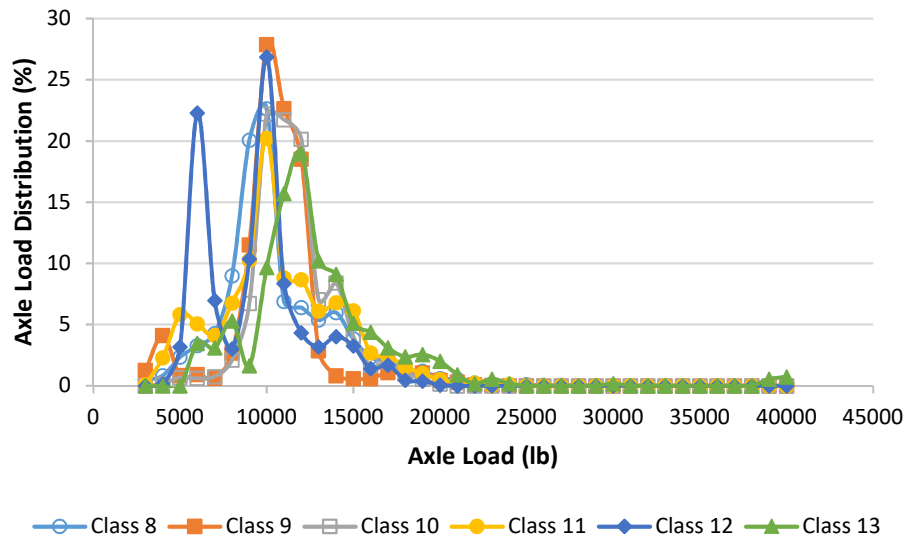


Figure 5.4 Single Axle Load Distribution for Category Two

As illustrated from Table 5.3, eight (No.1 to No. 8) vehicle categories are developed based on the vehicle class and axle type. For each axle type, there are two

categories based on the number of tires for each axle type. For the single axle, Category One ranges from vehicle class 4 to 7, Category Two is from vehicle classes 8 to 13. For each of the tandem, tridem and quadrem axles, vehicle classes 4 and 5 form one category and vehicle classes 6 to 13 form another category. Categories One, Three, Five and Seven are grouped for the single tire loading, and Categories Two, Four, Six and Eight are developed for the dual tires loading. The axle load cumulative distribution for the eight categories are then determined, which are used to calculate the actual number of loads in distribution of each category.

Table 5.3 Categories of Vehicle Classes

Vehicle Class	Single Axle	Tandem Axle	Tridem Axle	Quad Axle
4	No.1	No. 3	No. 5	No. 7
5				
6		No.2	No. 4	No. 6
7				
8				
9				
10				
11				
12				
13				

NOTE: Single Tire- No.1, 3, 5 and 7; Dual Tire-No. 2, 4, 6 and 8.

In order to save the computation time, the tire-pavement contact area is assumed to be a rectangular shape and the contact tire width is assumed to be constant. Therefore, only the contact tire length varies from one loading level to another. For example, the single axle load ranges from 3,000 to 40,000 lb. with 1,000 lb. interval. The number of loads in each interval of each axle is known, as shown in Table 5.2. For each interval of eight traffic categories, the tire length can be calculated using Equation 5.1.

$$l = \frac{P_L}{P_f \times w} \quad (5.1)$$

Table 5.4 shows the loading characteristics for different axle load types, including the tire width, tire type, tire pressure and axle load interval for each load category (Lytton et al. 2010). Meanwhile, for each category and axle load interval, there is a corresponding tire length. Based on the information in Table 5.4, the tire length is calculated for each load interval.

Table 5.4 Load Interval of Traffic loading Types

Category	Axle Type	Tires Type	Tire Width (in.)	Tire Pressure (PSI)	Axle Load Interval (lb.)
1	Single	Single	7.874	40 (≤ 6000 lb.)	3000-40000 lb. at 1000 lb. interval
2		Dual	8.740	120 (> 6000 lb.)	
3	Tandem	Single	7.874	120	6000-80000 lb. at 2000 lb. interval
4		Dual	8.740	120	
5	Tridem	Single	7.874	120	12000-102000 lb. at 2000 lb. interval
6		Dual	8.740	120	

Table 5.4 Continued

Category	Axle Type	Tires Type	Tire Width (in.)	Tire Pressure (PSI)	Axle Load Interval (lb.)
7	Quadrem	Single	7.874	120	12000-102000 lb.
8		Dual	8.740		at 3000 lb. interval

Table 5.5 presents the results of calculated tire lengths for different load categories. It should be noted that for each tire patch length, there may be more than one type of combinations of axle load, tire pressure and tire width. Tire patch length of 161 mm (6.350 inches) is taken as an example. It is calculated from both of the axle loads of 4,000 lb. and 12,000 lb. of single tire loading. As a result, the numbers of the two loading types are added together as the total number of tire patch length of 161 mm. Equation 5.2 is employed to characterize the cumulative axle load distribution for each axle load.

$$C(L_i)_j = e^{-e^{(\alpha-\gamma L_{ij})}} \quad (5.2)$$

where $C(L_i)_j$ is the cumulative axle load distribution factor at the tire length L_{ij} ;

L_{ij} is the tire length, which is listed in Table 5.5;

β and γ are the width parameter and slope parameter of the cumulative distribution curve, respectively.

An example is presented in Figure 5.5 using the traffic data of LTPP section 09-0960 for traffic loading of category one and two. Using Equation 5.2, α and γ are 2.623 and 0.533 for loading category one, respectively. In a similar way, α and γ are

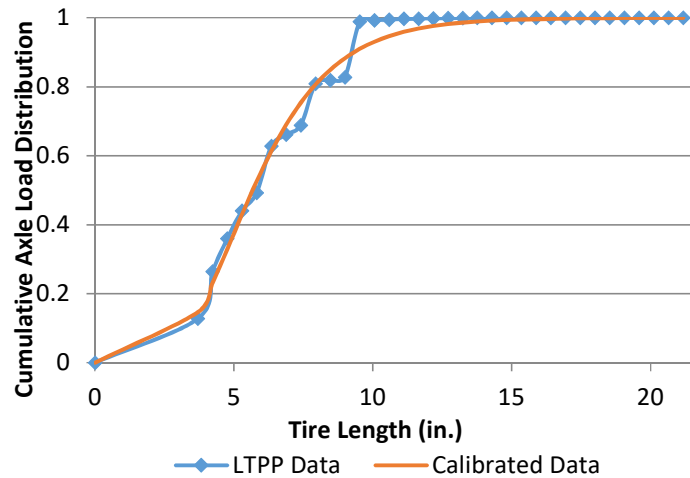
determined to be 8.367 and 1.460 for loading category two, respectively. Based on this method, α and γ can be calculated for the traffic loading of eight categories of each pavement section. As detailed in Chapter 4, the ANN models are developed for different tire lengths and tire types, and the cumulative axle load distribution will be used to predict traffic load distribution and load effect on the propagation of TDC with the interpolation method.

Table 5.5 Tire Lengths for Each Traffic Category

No. (<i>i</i>)	Category (<i>j</i>)							
	1	2	3	4	5	6	7	8
1	3.704	1.669	1.588	0.715	2.117	0.953	1.588	0.715
2	4.233	1.907	2.117	0.953	2.646	1.192	1.984	0.894
3	4.763	2.145	2.646	1.192	3.175	1.430	2.381	1.073
4	5.292	2.384	3.175	1.430	3.704	1.669	2.778	1.251
5	5.821	2.622	3.704	1.669	4.233	1.907	3.175	1.430
6	6.350	2.860	4.233	1.907	4.763	2.145	3.572	1.609
7	6.879	3.099	4.763	2.145	5.292	2.384	3.969	1.788
8	7.408	3.337	5.292	2.384	5.821	2.622	4.366	1.967
9	7.938	3.576	5.821	2.622	6.350	2.860	4.763	2.145
10	8.467	3.814	6.350	2.860	6.879	3.099	5.159	2.324
11	8.996	4.052	6.879	3.099	7.408	3.337	5.556	2.503
12	9.525	4.291	7.408	3.337	7.938	3.576	5.953	2.682
13	10.054	4.529	7.938	3.576	8.467	3.814	6.350	2.860
14	10.583	4.767	8.467	3.814	8.996	4.052	6.747	3.039
15	11.113	5.006	8.996	4.052	9.525	4.291	7.144	3.218
16	11.642	5.244	9.525	4.291	10.054	4.529	7.541	3.397
17	12.171	5.482	10.054	4.529	10.583	4.767	7.938	3.576
18	12.700	5.721	10.583	4.767	11.113	5.006	8.334	3.754
19	13.229	5.959	11.113	5.006	11.642	5.244	8.731	3.933
20	13.758	6.198	11.642	5.244	12.171	5.482	9.128	4.112
21	14.288	6.436	12.171	5.482	12.700	5.721	9.525	4.291
22	14.817	6.674	12.700	5.721	13.229	5.959	9.922	4.469
23	15.346	6.913	13.229	5.959	13.758	6.198	10.319	4.648
24	15.875	7.151	13.758	6.198	14.288	6.436	10.716	4.827
25	16.404	7.389	14.288	6.436	14.817	6.674	11.113	5.006
26	16.933	7.628	14.817	6.674	15.346	6.913	11.509	5.184

Table 5.5 Continued

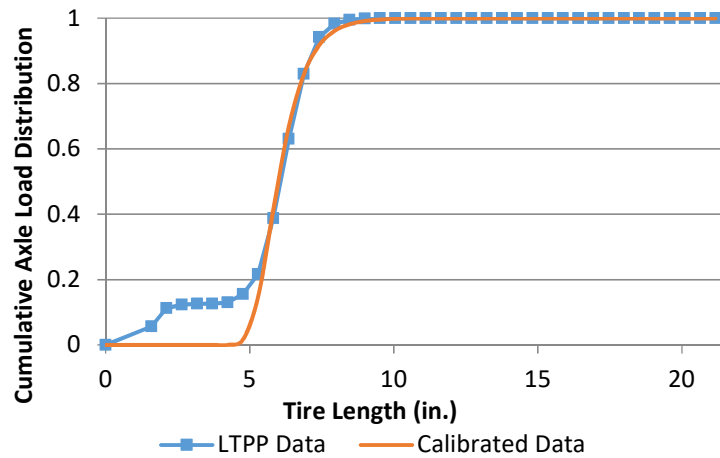
No. (<i>i</i>)	Category (<i>j</i>)							
	1	2	3	4	5	6	7	8
27	17.463	7.866	15.346	6.913	15.875	7.151	11.906	5.363
28	17.992	8.105	15.875	7.151	16.404	7.389	12.303	5.542
29	18.521	8.343	16.404	7.389	16.933	7.628	12.700	5.721
30	19.050	8.581	16.933	7.628	17.463	7.866	13.097	5.900
31	19.579	8.820	17.463	7.866	17.992	8.105	13.494	6.078
32	20.108	9.058	17.992	8.105	18.521	8.343	13.891	6.257
33	20.638	9.296	18.521	8.343	19.050	8.581	14.288	6.436
34	21.167	9.535	19.050	8.581	19.579	8.820	14.684	6.615
35	-	-	19.579	8.820	20.108	9.058	15.081	6.793
36	-	-	20.108	9.058	20.638	9.296	15.478	6.972
37	-	-	20.638	9.296	21.167	9.535	15.875	7.151
38	-	-	21.167	9.535	-	-	-	-



(a)

Figure 5.5 Cumulative Axle Load Distribution vs Tire Length: (a) Category

One, (b) Category Two



(b)

Figure 5.5 Continued

It is noted that for some pavement sections in which the WIM data is not available or incomplete, the AADTT data needs to be used to predict the traffic load distribution as the level two. The default distribution of major multi-trailer truck route determined in the MEPDG manual in Table 5.6 is adopted to calculate the number of vehicles in each truck class distribution. The default number of axles per truck is presented in Table 5.7.

Table 5.6 Distribution of Vehicle Classes

Vehicle Class	Distribution Percentage (%)	Vehicle Class	Distribution Percentage (%)
4	1.8	9	31.3
5	24.6	10	9.8
6	7.6	11	0.8
7	0.5	12	3.3
8	5.0	13	15.3

Table 5.7 Average Number of Axle for Each Vehicle Class

Vehicle Class	Single Axle	Tandem Axle	Tridem Axle	Quadrem Axle
4	1.62	0.39	0.00	0.00
5	2.00	0.00	0.00	0.00
6	1.02	0.99	0.00	0.00
7	1.00	0.26	0.83	0.00
8	2.38	0.67	0.00	0.00
9	1.13	1.93	0.00	0.00
10	1.19	1.09	0.89	0.00
11	4.29	0.26	0.06	0.00
12	3.52	1.14	0.06	0.00
13	2.15	2.13	0.35	0.00

5.2.3 Characterization of Field Distress Data

As mentioned previously, TDC is defined as the longitudinal crack parallel to the traffic direction in the pavement wheelpath. Based on this definition, the corresponding LTPP historical distress data are collected for each LTPP section for a long period of service time. Based on the definition by the LTPP manual (Miller and Bellinger 2003), there are three longitudinal cracking levels: low, medium and high. For the longitudinal cracking in the wheelpath, the low severity level is defined as a crack with a mean crack width less than 6 mm, the medium severity level is defined as a crack with a mean crack width greater than 6 mm but less than 19 mm, and the high severity level is named as a crack with a mean crack width greater than 19 mm. The length of longitudinal cracking is collected from the database and it versus the service time normally follows an S-shape curve. In this section, the longitudinal crack initiation time, distress shape parameter β

and distress scale parameter ρ are obtained for each pavement section. Equation 5.3 is used to describe the distress curve for the three severity levels. Since the length of a typical LTPP section is 150 m, the maximum longitudinal crack length is selected as 300 m for each pavement section.

$$l(t) = l_0 e^{-\left(\frac{\rho}{t-t_0}\right)^\beta} \quad (5.3)$$

where l_0 is the maximum longitudinal crack length (i.e., 300 m);

ρ and β are the scale parameter and shape parameter of the distress curve, respectively;

t_0 is the crack initiation time (days);

t is the pavement service time (days).

As the level of the distress is determined as the range of crack width, and the depth of the TDC is used in the FEM and ANN models as one input to calculate the J -integral, it is necessary to develop an empirical relationship between the TDC crack width and crack depth. In this study, the data extracted from (Kumara et al. 2004) is utilized to develop the empirical crack width versus crack depth model, as shown in Table 5.8. The best fitting function for the data in Table 5.8 is as follows:

$$\frac{w}{d_c} = 1.461 \times d_c^{-0.487} - 0.049 \quad (5.4)$$

where w is the width of the crack in mm; and d_c is the depth of the crack in mm. Equation 5.4 can be used to predict the depth of the crack according to the surface width of the same crack.

Table 5.8 Crack Width to Crack Depth Ratio (Kumara et al. 2004)

Crack Depth (mm)	w/d Ratio
0.5	2
5	0.6
17.1	0.32
90	0.115
100	0.106

As indicated in Table 5.8, the maximum crack depth is 100 mm, and the corresponding crack width is 10.6 mm. In the calculation of crack propagation, the critical crack depth is selected as 100 mm and it is within the medium level based on the LTPP severity definition. Using Equation 5.4, the critical crack depth between the low and medium severity levels is calculated as 21.5 mm. Observation from the LTPP distress data shows that most of the data points for the longitudinal crack in the wheelpath are located in the low and medium severity levels. It is also shown that most field cores exhibiting TDC have shallow crack depths, and the corresponding depths are in the low and medium LTPP severity levels. In the study, the distress data points of the low, medium and high levels are combined, since it is not practical and may not be accurate to plot the distress curve using few points in the high severity level. A typical example is shown in Figure 5.6 using the longitudinal cracking distress data from LTPP section 4-0117. As seen from Figure 5.6, the maximum length of observed distress is less than 120 m in about 10 years. Meanwhile, a calibrated distress curve is plotted using Equation 5.3 to obtain the parameters ρ , β and crack initiation time t_0 with the sum of squared errors (SSE)

technique. The parameters ρ and β , and crack initiation time t_0 are determined as 1832, 1.1 and 1820 (approximately 5 years), respectively.

The historical distress data for more than 200 pavement sections are collected to cover four different climate zones and five different pavement structures. Using the similar method, the parameters of the distress curve and crack initiation time are determined for each pavement section, which are used in the model development and calibration for the TDC initiation and propagation phases.

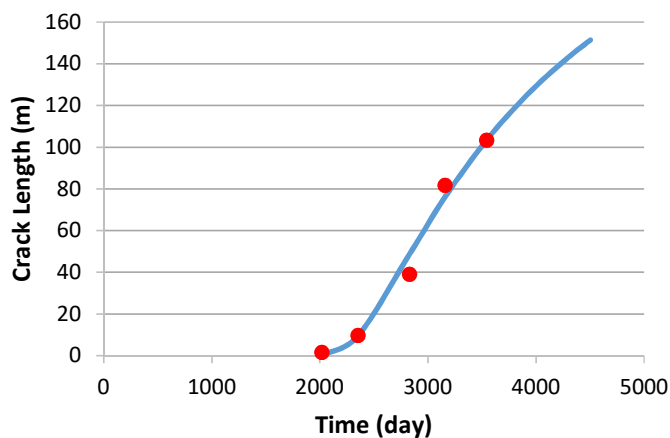


Figure 5.6 Example of Crack Length versus Service Time

5.3 Materials Properties of Pavement Layers

5.3.1 Asphalt Layer

The unaged dynamic modulus of asphalt layer is predicted based on the unaged binder properties and volumetric properties, and the information can be obtained from the LTPP database. It should be mentioned that for some sections the dynamic modulus

documented in the LTPP database is not the unaged modulus, in fact it was measured using the collected field cores at some time after construction, which is actually the aged dynamic modulus. It is not accurate to use those dynamic modulus data from the LTPP database. Therefore, the ANN model is developed to estimate the unaged dynamic modulus using the binder and aggregate properties. Once the unaged dynamic modulus is predicted, the aged dynamic modulus can be predicted based on the aging shift functions, which are detailed in Chapter 3.

It is well-known that the air void distribution in the asphalt layer affects the material properties such as the modulus and fracture resistance of the asphalt mixtures at different depths. Specifically, the air void content is not uniformly distributed within the pavement depth. An example of air void distribution measured from X-ray CT by cutting field core into slices is given in Figure 5.7. As seen from Figure 5.7, the distribution usually follows a C-shape curve, which indicates the highest air void contents are identified at the surface and bottom of asphalt layer. The higher air void content at the surface of pavement means more possibilities of cracks initiating at the surface then form more micro-cracks. This also indicates that the binder oxidative aging is severer at the surface of the pavement due to the high oxygen availability and solar radiation. The air void distribution is considered as one of the main causes for the initiation of TDC.

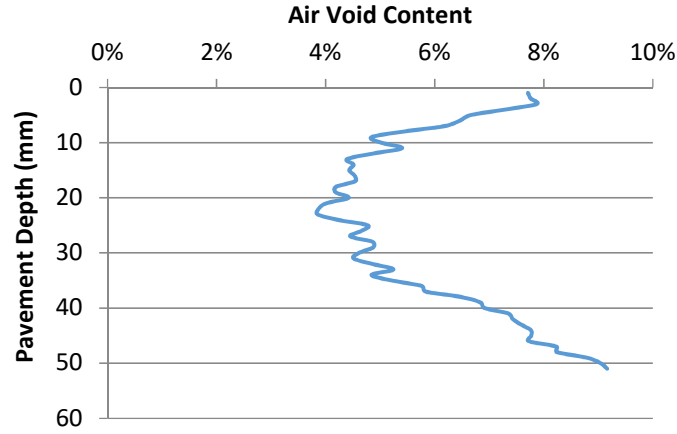


Figure 5.7 Air Void Distribution in Pavement Depth

The air void content in pavement depth for an asphalt layer is modeled as follows:

$$a(z) = a_{\min} + \frac{a_{\max} - a_{\min}}{h^2} (h - 2z)^2 \quad (5.5)$$

where $a(z)$ is the air void distribution at pavement depth z ; a_{\max} is the maximum air void content; a_{\min} is the minimum air void content; and h is the thickness of the asphalt layer.

The average air void content \bar{a} , which is an mixture design parameter and readily available in the LTPP database, is calculated as

$$\bar{a} = \frac{1}{h} \int_{z=0}^{z=h} a(z) dz = \frac{1}{h} \int_{z=0}^{z=h} \left[a_{\min} + \frac{a_{\max} - a_{\min}}{h^2} (h - 2z)^2 \right] dz = \frac{2}{3} a_{\min} + \frac{1}{3} a_{\max} \quad (5.6)$$

Based on the X-ray CT measurement, a_{\max} is about two times as a_{\min} , the following relationship can be achieved:

$$a_{\min} = \frac{3}{4} \bar{a}, \quad a_{\max} = \frac{3}{2} \bar{a} \quad (5.7)$$

Therefore, once the average air void content is known from the pavement mixtures design, the air void distribution can be predicted using Equation 5.7.

Once the shape of air voids distribution is predicted, the unaged modulus within the pavement depth is determined, which shows an inverse C-shape curve. It indicates that lowest moduli is at the surface and bottom of an unaged asphalt layer. However, with the long-term oxidative aging process, the modulus gradient is developed and it becomes more curved as aging time increases, as illustrated in Figure 5.8. The detailed derivations of determining the modulus gradient of asphalt layer is documented in Chapter 2.

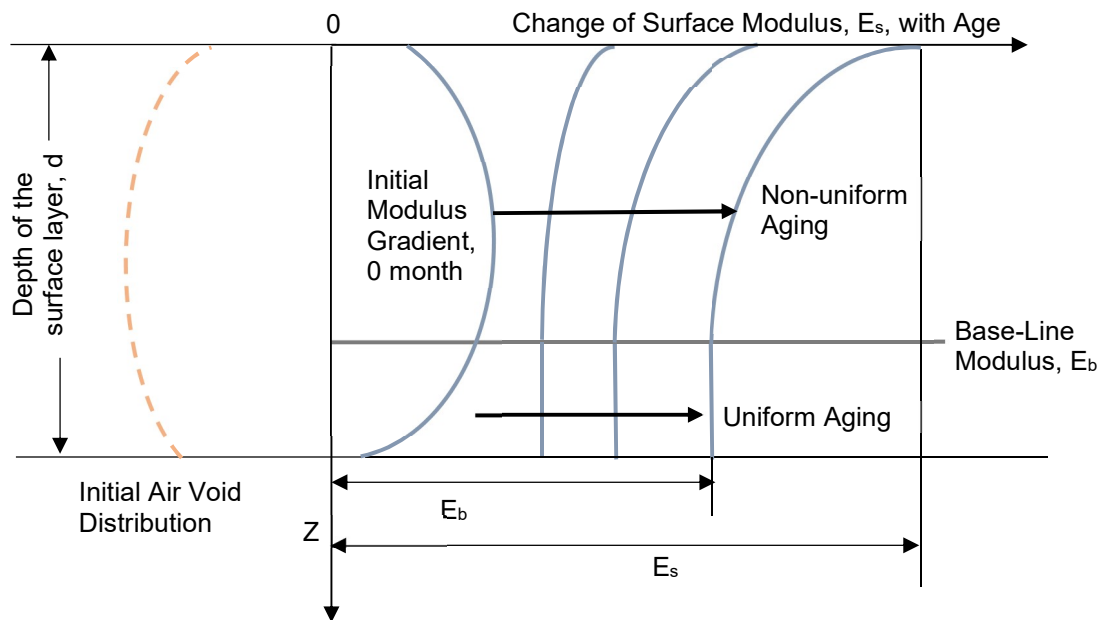


Figure 5.8 Evolution of Modulus Gradient in Asphalt Layer

5.3.2 Base and Subgrade Layers

For the purpose of simplicity, the base and subgrade layers are assumed to be elastic and isotropic, since these two layers have much less effect compared to the asphalt

layer for the initiation and propagation of TDC. In this study, there are two input levels for properties of the base and subgrade layers, level one is for the resilient modulus that is adjustable for each month, due to the weather effect. Level two is two typical constant values of the moduli for the base and subgrade layers, respectively. The thickness of layers are collected or can be back-calculated from the FWD data from the LTPP.

It is noted that the pavement system may not be exactly a three layer system. In order to reduce the number of runs and computation time for FEM and ANN models, the Odemark's method of equivalent thickness is adopted to reduce the number of pavement layers (Odemark 1949 and Zhou et al. 2010).

$$H_1' = H_1 + \sum_{i=2}^n H_i \sqrt[3]{\frac{E_i}{E_1}} \quad (5.8)$$

where H_1' is the equivalent thickness;

H_n is the original thickness of layer n , respectively;

E_1 and E_n are the moduli of layer 1, and n , respectively.

5.4 Modeling of Crack Initiation and Propagation of TDC

5.4.1 TDC Initiation Model

A new TDC fatigue crack initiation model is proposed in the subsection. Crack initiation time (Figure 5.6) is defined as the number of days for the crack first appears at the pavement surface, indicating a macro-crack can be visually observed. For an asphalt pavement, the fatigue life is determined as follows:

$$N_f = N_i + N_p \quad (5.9)$$

where N_f is the number of loading cycles (fatigue life) of the pavement until failure;

N_i is the number of loading cycles for a macro-crack to initiate;

N_p is the number of loading cycles for a macro-crack to propagate.

It should be mentioned that the asphalt mixture suffers fatigue damage from the first loading cycle. The micro-cracks first initiate from the air voids which are induced by the repeated load applied at the surface of the pavement. The as-compacted air voids of an in place pavement are the initial damages, which cause the local stress concentration. Therefore, the cracks are already initiated at the time of construction, and these cracks are micro-cracks appearing in the “crack initiation” loading cycles. After a number of loading cycles, the number of micro-cracks is reduced and micro-cracks start to coalescent and form a macro-crack, which can be seen at the pavement surface. From a practical point of view, the number of loading cycles in this period of time is termed as the fatigue life of crack initiation, and the duration is the observed crack initiation time. After the crack initiation point, the macro-crack propagates from the surface downward. After a long service time when the macro-crack propagates, the width and length of the macro-crack become wider and longer respectively and the lengths of the corresponding three levels are recorded in the LTPP database. The time after crack initiation until failure or approaching the critical crack depth is called the crack propagation time.

The MEPDG and other widely used fatigue life prediction models such as the Shell oil model and Asphalt Institute model indicate that a general form of the fatigue models is as follows (AASHTO 2008b, Shell 1978 and Asphalt Institute 1982):

$$N_f = Ck_1 \left(\frac{1}{\varepsilon} \right)^{k_2} \left(\frac{1}{E} \right)^{k_3} \quad (5.10)$$

where k_1, k_2, k_3 are regression coefficients;

ε and E are the critical strain and modulus of asphalt layer;

C is the laboratory to field shift factor.

It is worth mentioning that this model is first developed for the crack initiation stage. In order to account for the crack propagation, a shift factor C is applied to estimate the fatigue life of the pavement including the both the crack initiation and propagation. Therefore, it is difficult to investigate the two stages separately using the transfer function. Due to the empirical nature of this equation, the fundamental fracture law - Paris' law and cumulative damage models are used instead to predict the micro-crack growth in the crack initiation period.

It is shown that the J -integral is calculated from the FEM in Chapter 4. Note that the results obtained from the FEM and ANN models are determined for a single macro-crack for characterizing the crack propagation phase (Ling et al. 2017b). In the crack initiation phase, there are multiple micro-cracks initiate first from the air voids and then coalesce into a visible macro-crack (Lytton et al. 1993). In this initiation phase, the damage density is used in Paris' law instead of a single crack. Damage density is the ratio of the lost area to the total cross-sectional area. Initially, the lost area is the percent air voids in

the asphalt mixture. The pseudo J -integral is determined in Equation 5.11 based on the definition.

$$J_R = \left[\frac{\left(\frac{dW_R}{dN} \right)}{\left(\frac{d(CSA)}{dN} \right)} \right] \quad (5.11)$$

where J_R is the load induced pseudo J -integral;

W_R is the load induced pseudo displacement work;

CSA is the crack surface area;

N is the number of loading cycles for a load level.

For an in-situ asphalt pavement, there are multiple traffic load levels (number of tires and axles), which are characterized using the load spectra model detailed in the previous section. Because of this, the pseudo-displacement work and pseudo J -integral are different for different load levels. For one cyclic loading of one moving traffic load, the pseudo-displacement work is determined as:

$$W_R = \frac{P^2}{2S} \sin(\varphi_{NVE} - \varphi_{VE}) \quad (5.12)$$

where P and S are the load and pseudo stiffness, respectively.

As the loading level increases, multiple distributed cracks increases in size, decrease in number, and coalesce. The pseudo displacement work for a continuous cyclic loading without rest period at load level i is determined as follows:

$$W_{Ri} = a_i N^b \quad (5.13)$$

where a_i and b_i are the fitting parameters of the pseudo displacement work. They are functions of load levels:

$$a_i = a_0 \left(\frac{P_i}{P_0} \right)^2 \quad (5.14)$$

$$b_i = b_0 \quad (5.15)$$

The crack surface area (CSA) is termed as the cracked area in the cross-section of the asphalt layer. It can be determined as a function of damage density and cross-sectional area, as shown in Equation 5.16. The damage density is a function of loading cycles and used in the Paris's law to replace the crack length in Equation 5.17 (Paris and Sih 1965):

$$CSA = 2\phi S_0 \quad (5.16)$$

$$\frac{d\phi}{dN} = A' \left[\frac{d(W_R)}{d(CSA)} \right]^{n'} = A' \left(\frac{a_i b_i N^{b_i-1}}{2S_0 \frac{d\phi}{dN}} \right)^{n'} \quad (5.17)$$

where ϕ is damage density of the cross-sectional area;

A' and n' are the Paris' law coefficients.

Integrating Equation 5.17 produces the number of cycles for crack initiation at loading level i in Equation 5.18:

$$N_i = \left[\frac{\phi_c - \phi_0}{A'^{\frac{1}{n'+1}} \left(\frac{a_i b_i}{2S} \right)^{\frac{n'}{n'+1}} \left(\frac{n+1}{b_i n' + 1} \right)} \right]^{\frac{n'+1}{b_i n' + 1}} \quad (5.18)$$

where N_i is the number of loading cycles for crack initiation for load level i ;

ϕ_0 is the initial damage density equal to the size of the air voids at the pavement surface;

ϕ_c is the critical damage density corresponding to the critical crack size at which multiple distributed cracks coalesce into a single crack (“crack initiation”) and the single crack then propagates (“crack propagation”).

For different loading levels, N_i values are different since the pseudo displacement work is related to the load level as indicated in Equation 5.12. The fracture parameters A' and n' are the same since they are material properties of the asphalt mixtures. The air void content of an in place asphalt mixture is the initial damage, indicating that it is from the air voids that the cracks begin to grow. The air void content at the surface layer is predicted using Equation 5.19, which is detailed in the previous section.

$$a_{\max} \approx \frac{3}{2} a \quad (5.19)$$

The Miner’s hypothesis is used to characterize the contribution of number of different loading cycles for different loading levels for the crack initiation and calculate the work parameters a and b of the pseudo displacement work.

$$T_0 \sum_{i=1}^{i=n} \frac{AADTT_i}{N_i} = 1 \quad (5.20)$$

The distribution of $AADTT$ is obtained from the load spectra when the WIM data is available (Level One), otherwise the default load spectra is used (Level Two). The work parameters a_0 is found to be a function of material properties (m value of relaxation modulus parameter and magnitude of modulus E_I), environmental factors including the

number of days above 32°C and number of days below 0°C for the aging and thermal effects, pavement structures including the thickness of asphalt layer and thickness of the pavement system, and AADTT. Because T_0 is determined by fitting field observations, the healing effect is included in the work parameter. Once the prediction equation for a_0 is determined, the TDC initiation time for an asphalt pavement can be estimated.

5.4.2 TDC Propagation Model

The TDC propagation phase is determined using the Paris' law. A similar approach is applied to calculate the daily thermal crack growth due to the temperature drop or thermal loading cycles and associated thermal stress, which is discussed in the next section. The aging properties such as modulus gradient of asphalt layer are included in the model.

Based on the Paris's law, the total daily crack growth can be computed as follows:

$$\Delta c_{TR} = \sum_{i=1}^{i=n} dc_i = \sum_{i=1}^{i=n} A' [J_{TRi}]^{n'} N_i \quad (5.21)$$

$$\Delta c_{TH} = \sum_{i=1}^{i=n} dc_i = \sum_{i=1}^{i=n} A' [J_{TH}]^{n'} N_i \quad (5.22)$$

where Δc_{TR} and Δc_{TH} are the daily crack growth due to traffic or thermal loading, J_{TR} and J_{TH} are the traffic loading and thermal loading induced J -integral, respectively.

There are three levels for predicting the Paris' law fracture coefficients A' and n' . Level one is the values of A' and n' directly measured from fatigue or fracture test of the asphalt mixtures, such as the repeated direct tension test and overlay test. Level two is

based on the empirical equations to predict the values of A' and n' with known material properties shown in Equations 5.23 and 5.24 (Luo et al. 2016). Level three is used to estimate A' and n' , on the basis of the fracture properties database from previous tests if the material properties are unknown.

$$n' = -16.05 + 0.13AV\% + 6.50\ln(AB\%) + 8.15\psi + 5.51\frac{1}{m} - 81.515\left(\frac{1}{E_1}\right)^m \quad (5.23)$$

$$A' = 10^{-(1.246n' + 3.615)} \quad (5.24)$$

where $AV\%$ is the air void content in %, $AB\%$ is the asphalt binder content in %; ψ is the aggregate shape parameter; and E_1 and m are relaxation modulus parameters, E_1 in MPa. The parameters for the material properties of asphalt mixtures in Equations 5.23 and 5.24 are available from LTPP database.

Once the daily crack growths of traffic loading and thermal loading are determined, the number of days due to traffic loading and thermal loading to reach the 100 mm crack depth can be calculated. The number of days to reach this criteria for the traffic loading includes the longitudinal, transverse, and vertical contact stresses. The number of days for the thermal loading is the duration to reach the 100 mm crack depth by thermal drops and loading cycles.

5.4.3 Thermal-induced Damage Model

Significant thermal stress in asphalt pavements normally occurs at low temperature climate zones. As the temperature drops, the asphalt pavement shrinks and builds up the thermal tensile stress. Once the thermal stress exceeds the tensile strength of the asphalt

pavement, the crack initiates from the surface. The thermal-induced damage can be formed within one severe thermal drop or multiple thermal cycles. It is noted that as the modulus increases due to oxidative aging, the thermal-induced damage becomes more obvious. The transverse thermal stress is of interest and calculated in this study rather than the longitudinal thermal stress because of the direction of longitudinal cracking, and it is smaller than the longitudinal thermal stress for thermal cracking due to different boundary conditions. Compared to the traffic loading, thermal loading cycle can take hours even days to apply on the asphalt pavements. Therefore, it is necessary to use the viscoelastic constitutive equation to calculate the thermal stress (also the far field stress at the same crack depth).

$$\sigma(\xi) = \int_0^{\xi} E(\xi - \xi') \frac{d\varepsilon}{d\xi'} d\xi' \quad (5.25)$$

where $\sigma(\xi)$ is the thermal stress at reduced time ξ ;

$E(\xi - \xi')$ is the relaxation modulus at reduced time ξ ;

ε is the strain at reduced time ξ .

The strain is calculated based on the relationship between the coefficients of thermal contraction and change of temperatures, which is shown in Equation 5.26:

$$\varepsilon = \alpha_{mix} [T(\xi') - T_0] \quad (5.26)$$

where α_{mix} is the coefficient of thermal contraction of the asphalt mixture;

$T(\xi')$ is the pavement temperature at reduced time ξ ;

T_0 is the stress-free pavement temperature.

It is noted that α_{mix} is affected by the coefficients of thermal contraction of asphalt binder, aggregates and air voids. In this study, there are three different values of α_{mix} to cover its possible range (i.e., 1E-5, 2E-5 and 4E-5) in the FEM and ANN models. The relaxation modulus $E(t)$ is calculated from the storage modulus $E'(\omega)$ of dynamic modulus using the Prony series, which is shown in Equations 5.27 and 5.28:

$$E'(\omega) = E_e + \sum_{i=1}^{i=m} \frac{\omega^2 \rho_i^2 E_i}{\omega^2 \rho_i^2 + 1} \quad (5.27)$$

$$E(t) = E_e + \sum_{i=1}^{i=m} E_i e^{-\frac{t}{\rho_i}} \quad (5.28)$$

where E_e is the equilibrium modulus;

ρ_i is the relaxation time.

The schematic plot of the thermal cracking in the asphalt layer is presented in Figure 5.9. The modulus gradient and long-term oxidative aging are also included in the thermal cracking calculation. After obtaining the viscoelastic thermal stress, the thermal J -integral is determined based on the FEM analysis and ANN models.

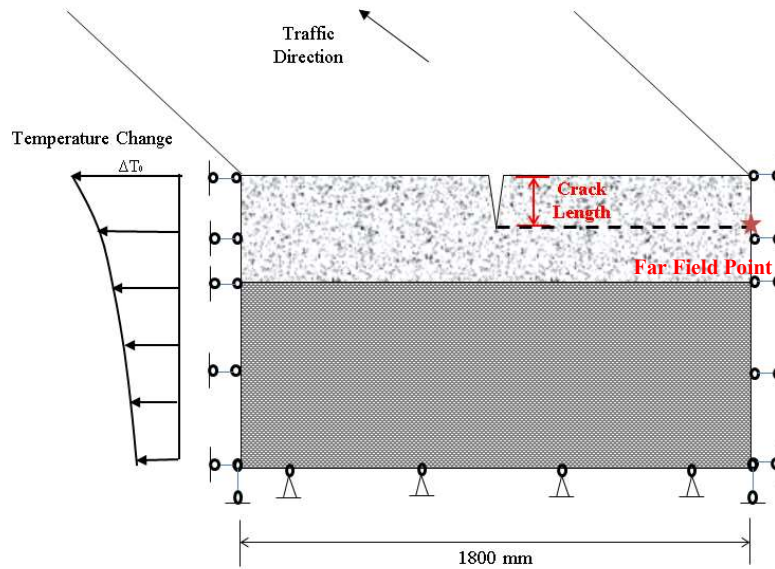


Figure 5.9 Schematic Plot of Thermal Cracking in FEM

5.4.4 Calibration and Validation of TDC Propagation Model

As discussed previously, there are three severity levels L, M and H for asphalt pavements, and they are combined together to form a single distress curve. For each pavement section, there is a pair of ρ and β obtained from plotting the distress data points of the three combined severity levels. Equations 5.29 and 5.30 are used to predict the calibration coefficients, which are similar with those in Lytton et al. (2000).

$$\rho = N_{TR} \left(\alpha_0 - \alpha_1 \frac{N_{TR}}{N_{TH}} \right) \quad (5.29)$$

$$\beta = \frac{1}{N_{TR}} \left(\gamma_0 + \gamma_1 \frac{N_{TH}}{N_{TR}} \right) \quad (5.30)$$

where N_{TR} and N_{TH} are the number of days for traffic loading and thermal loading to reach the critical crack depth of 100 mm, respectively. α_0 , α_1 , γ_0 , and γ_1 are calibration coefficients. A total of 80% of collected LTPP sections are used to cover different climatic zones and pavement structures in the calibration process.

A total of 20% of the overall LTPP pavement sections are used for validation purposes, which are not used in the calibration process. This is used to validate the calibrated model and improve the accuracy of the model.

5.5 Endurance Limit Prediction of Asphalt Pavement Layers

The concept of endurance limit for asphalt pavement layers is defined as the maximum strain or stress level that the no fatigue cracking occurs or can be healed during the rest period or unloading time. If the strain/stress is kept below the endurance limit, the pavement is assumed to have an infinite fatigue life (Monismith and McLean 1972; Witczak et al. 2013). It has been shown that the endurance limit does exist from several comprehensive studies primary from the three point bending beam fatigue test. Determining the endurance limit is important to the construction of a perpetual pavement. Specifically, once the endurance limit for a specific asphalt mixture is accurately determined, it becomes convenient to calculate the minimum thickness of an asphalt layer, which is significantly beneficial to the pavement design and helps reduce the maintenance cost. Figure 5.10 shows the fatigue endurance limit of an asphalt mixture, which indicates that as the strain decreases below a specific strain level (endurance limit), the number of load repetitions becomes infinite and the asphalt mixture has a long fatigue life.

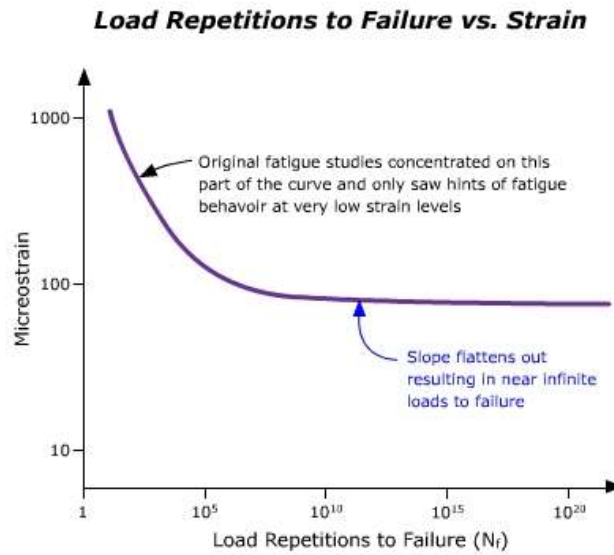


Figure 5.10 Concept of Endurance Limit (after Pavement Interactive 2012)

As indicated earlier, healing is a counterpart of fatigue cracking, especially during the crack initiation period (Little et al. 2001; Dinegdae et al. 2015; Souliman 2012). For a specific test temperature, loading frequency and level, healing can be empirically related to the duration of the rest period between two adjacent loading cycles. It is known that healing also occurs in the unloading part. The healing effect on fatigue cracking is highly desired (Carpenter et al. 2003; Zeiada 2012; Souliman 2012). Since the healing effect on the endurance limit and fatigue life is well studied, currently no rest period is applied in the experimental part of this study.

In this study, the endurance limit of asphalt mixtures is determined using repeated direct tension test based on a mechanical analysis. Repeated direct tension test is a strain-controlled cyclic load test, which allows to increase the strain level starting from linear viscoelastic stage to non-linear viscoelastic stage then to damage stage (e.g., from 20

micro-strain to 200 micro-strain with a 10 micro-strain interval). A typical stress and strain versus time, and stress-strain curve of one loading cycle for this test is shown in Figures 5.11 and 5.12, respectively.

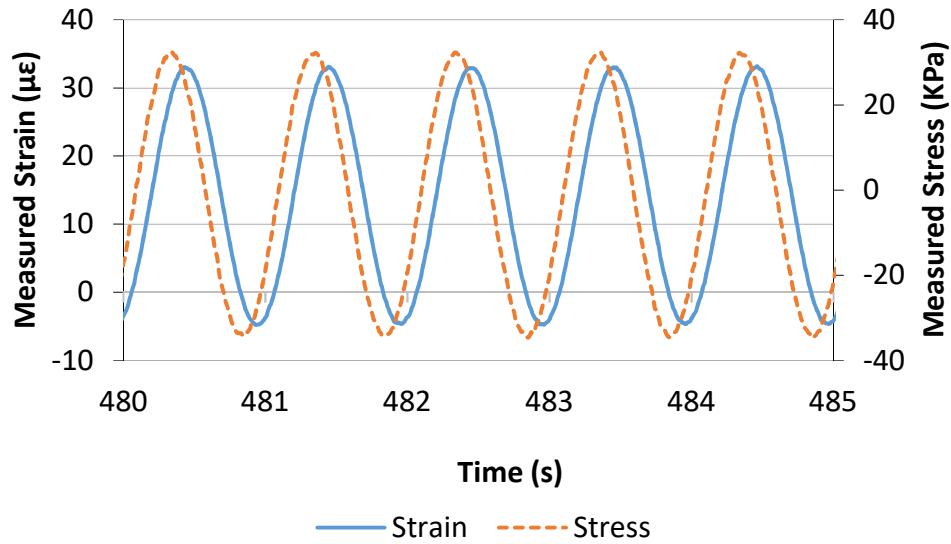


Figure 5.11 Stress and Strain versus Time

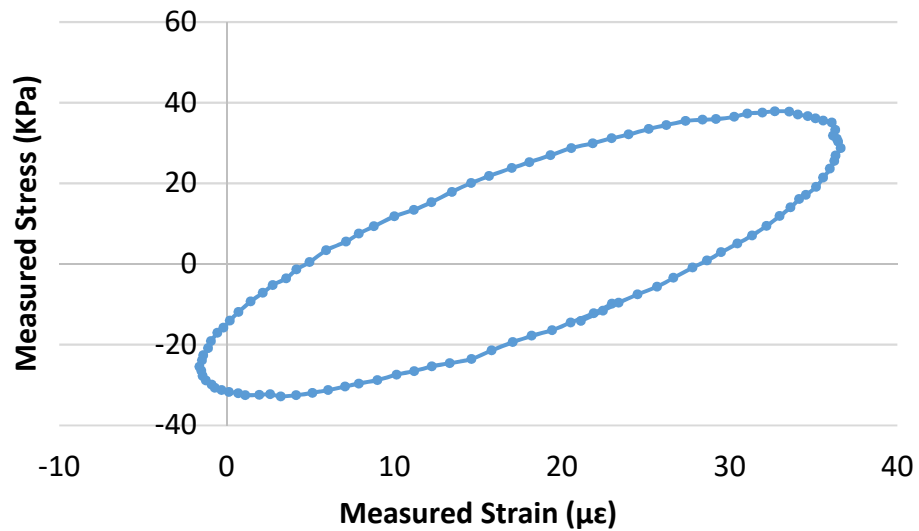


Figure 5.12 Stress-Strain Curve

The pseudo strain and stress curve is shown in Figure 5.13. The pseudo strain is utilized to remove the viscoelastic effect. For a viscoelastic material under cyclic loading, some of the energy obtained from the external cyclic loading is used to overcome the viscous effect of the material. Specifically, in the linear viscoelastic stage, the energy is consumed to overcome the viscous effect only. In the non-linear viscoelastic stage, the energy is used for the viscous effect and non-linear effect at the plastic zones. In the damage stage, the obtained energy is used for the viscous effect, non-linear effect and damage effect such as cracking and plastic deformation. Therefore, using the concept of pseudo strain, the viscoelastic effect is removed, and the calculated pseudo energy is consumed only for non-linear effect and damage for these two stages, respectively. The pseudo strain is calculated using Equation 5.31:

$$\varepsilon_R = \frac{\sigma_{VE}(t)}{E_R} = \frac{\int_0^t E(t) \frac{\partial \varepsilon(\tau)}{\partial \tau} d\tau}{E_R} \quad (5.31)$$

where $\sigma_{VE}(t)$ is the viscoelastic stress, $E(t)$ is the relaxation modulus, $\varepsilon(\tau)$ is the strain history, ε_R is the pseudo strain, E_R is the reference modulus, which is the dynamic modulus for the test temperature and frequency.

The criteria of exceeding the endurance limit of the asphalt mixtures is that when the dissipated pseudo strain energy density begins to increase with increasing number of loading cycles at the critical strain level. This pseudo strain energy density is calculated as shown in Equation 5.32, which is the area of the hypothesis loop in Figure 5.13.

$$DPSE = \int_{t_1}^{t_2} \sigma(t) \frac{d\varepsilon_R(t)}{dt} dt \quad (5.32)$$

where W_R is the pseudo strain energy density produced from t_1 to t_2 , $\sigma(t)$ is the measured stress, $\varepsilon_R(t)$ is the pseudo strain.

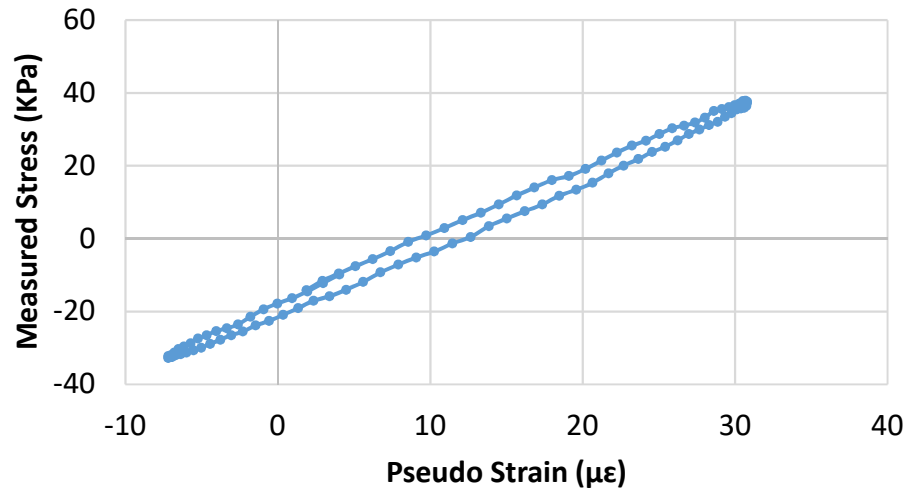


Figure 5.13 Measured Stress versus Pseudo Strain

A crack initiation equation for asphalt mixtures is proposed, which is based on the Griffith crack criteria. As mentioned before, the initial cracks are the air voids, and it is reasonable to assume an embedded penny-shaped shape for the initial cracks, not the through crack type. There are three energy density components in the crack initiation energy balance equation of asphalt mixtures, as shown in Equations 5.33, 5.34 and 5.35, which indicates that enough potential pseudo strain energy is needed to overcome the surface energy of the two newly developed cracks and the viscoplastic energy at the non-linear zones at the crack tips for the cracks to grow.

$$w \approx 2 \times \frac{\sigma^2}{2E_R} \quad (5.33)$$

$$s = 2\Delta G \quad (5.34)$$

$$g_p = DPSE \quad (5.35)$$

where w is the released pseudo strain energy density, s is the surface energy of the two new cracks per unit area, g_p is the pseudo strain energy density that is needed to overcome the plastic effect in the non-linear viscoelastic stage, c_0 is the mean air void radius. The volume of the released energy zone are shown in Figure 5.14, they are assumed to be approximately two triangles above and below the two dimensional and through crack. For an embedded penny-shape crack, the energy released volume is approximately two cones above and below the crack. The plastic zones at the crack tip are assumed to be approximately a circular shape for two dimensional and the through crack shown in Figure 5.15, and for the volume of a penny-shaped crack in the three dimensional space, it is appropriate to assume a ball shape at two crack tips. The closed form solution for stress intensity factor K_I is calculated as $K_I = \frac{2}{\pi} \sigma \sqrt{\pi c_0}$, and the radius of plastic zone is

computed as $r_y = \frac{1}{2\pi} \left(\frac{K_I}{\sigma_{YS}} \right)^2$ (Anderson 2005).

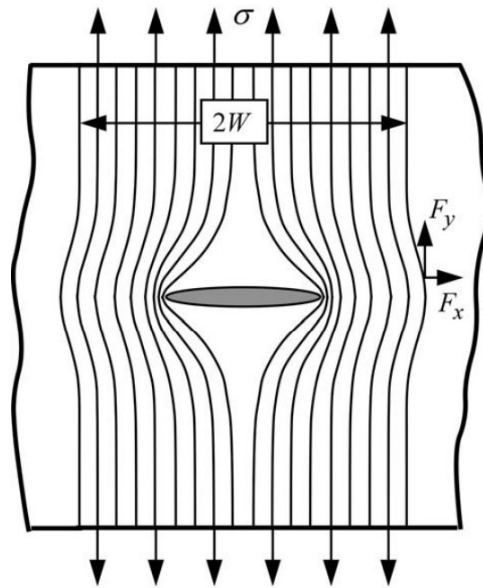


Figure 5.14 Energy Released Zone in Infinite Plate (after Anderson 2005)

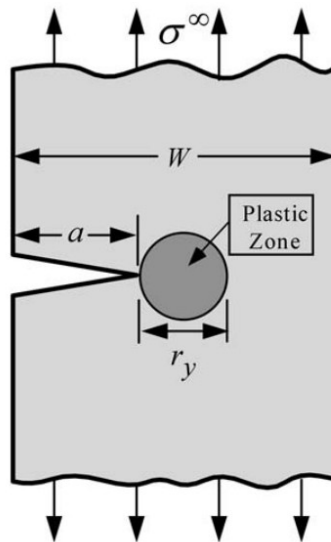


Figure 5.15 Plastic Zone at the Crack Tip (after Anderson 2005)

Equations 5.36 is employed to determine the critical point that the crack initiates after multiplying the associated volumes to the three energy density components, and it can be further modified to relate to the pseudo strain from Equation 5.37:

$$\frac{d(W - S - G_p)}{dc_0} = 0 \quad (5.36)$$

$$\varepsilon_{cR}^E \approx \sqrt{\frac{(\Delta G_c + 0.04DPSE \times c_0)}{2E_R \pi c_0}} \quad (5.37)$$

where ε_{cR}^E is the pseudo strain endurance limit for cohesive fracture.

It is noted that Equation 5.37 is for the cohesive fracture only. Cohesive fracture and adhesive fracture normally occur within the asphalt mastic and at asphalt-aggregate interface, respectively, which is based on the asphalt film thickness. Using the similar method, the pseudo endurance limit for adhesive fracture is determined as:

$$\varepsilon_{aR}^E \approx \sqrt{\frac{(\Delta G_a + 0.04DPSE \times c_0) \times E_f}{\left(1 + \frac{E_f}{E_s}\right) c_0 \pi E_R^2}} \quad (5.38)$$

where E_f is the modulus of fluid (asphalt binder), E_s is the modulus of solid (aggregates). It is shown that the endurance limit increases as the DPSE and bond energy increase, and decreases as the air void content and modulus increase. This matches the observations from the literatures (Epps and Monismith 1972; Harvey and Tsai 1996; Norouzi et al. 2016). For an asphalt mixture with a higher binder content, which is corresponding to thicker film thickness, the endurance limit also increases. As aging time increases, the bond energy decreases as reported in literature which indicates that the fracture resistance becomes weaker, the modulus also increases with aging, which causes the endurance limit decreases.

5.6 Black Space Diagram for Asphalt Mixtures

The black space diagram is a simple but effective schematic plot which includes both of the dynamic modulus and corresponding phase angle. The viscoelastic properties is illustrated in this diagram, which can also be used to track the properties change due to environmental effects such as aging and temperature. It was investigated that the ductility of binders is highly related to the pavement surface cracking (Kandhal 1977). The author showed that when the ductility at 60°F reaches 10 cm, it shows that the pavement losses some surface fines; when the ductility drops below 5 cm, the surface cracking initiates; and when the ductility is below 3 cm, a serious pavement cracking is observed. Glover et al. (2005) developed a cracking parameter $G' / \left(\frac{\eta'}{G'} \right)$ based on the binder ductility, then Rowe (2011) proposed a simplified parameter $G' \omega / \tan \delta$ (Glover-Rowe Parameter) to predict the surface cracking. In both of the parameters, the frequency and temperature are fixed (0.005 rad/s and 15°C) and the limiting value is 900 Pa/sec. The damage onset of cracking and significant cracking are determined as 180 KPa and 450 KPa, respectively.

One example of the black space diagram with the Glover-Rowe parameter is presented in Figure 5.16. It is shown that as the aging level increases, the asphalt mixtures are shifted from the right bottom corner to the left top corner of this diagram, so the mixtures move from the “pass” region to the “fail” region.

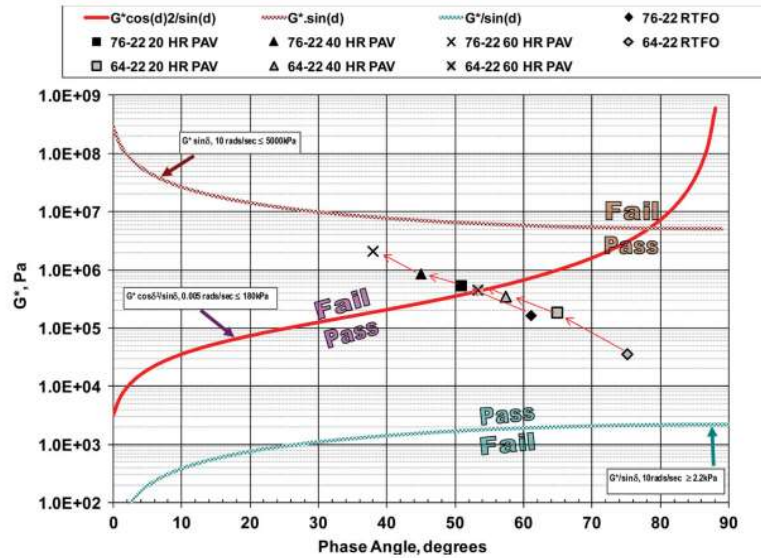


Figure 5.16 Example of Black Space diagram with Glover-Rowe Parameter (after Bennert 2014)

Another example of utilizing the black space diagram is by using the rheological index R . It is the parameter in the CAM model which can be used to characterize the aging of asphalt binders. The discussion of the determination of the rheological index R of asphalt mixtures is detailed in Chapter 3. As seen from Figure 5.17, as aging time increases, the asphalt mixture is more prone to cracking, and the R value also increases.

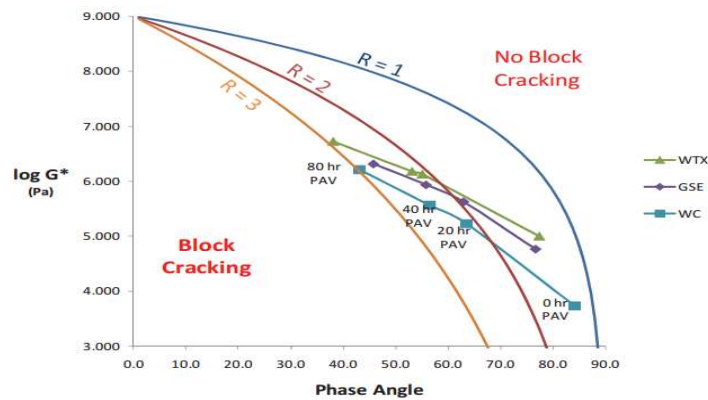


Figure 5.17 Example of Black Space Diagram with R Curves (after King et al. 2012)

As indicated above, the black space diagram is an efficient tool to illustrate the change of the viscoelastic properties especially for aging. In this study, a new failure line is developed based on the endurance limit and linear viscoelasticity. An example of dynamic modulus versus phase angle for unaged and short-term aged asphalt mixtures is illustrated in Figure 5. 18. As can be seen, the phase angle decreases and modulus increases with increasing aging of asphalt mixtures and the points move from bottom right corner to the top right corner.

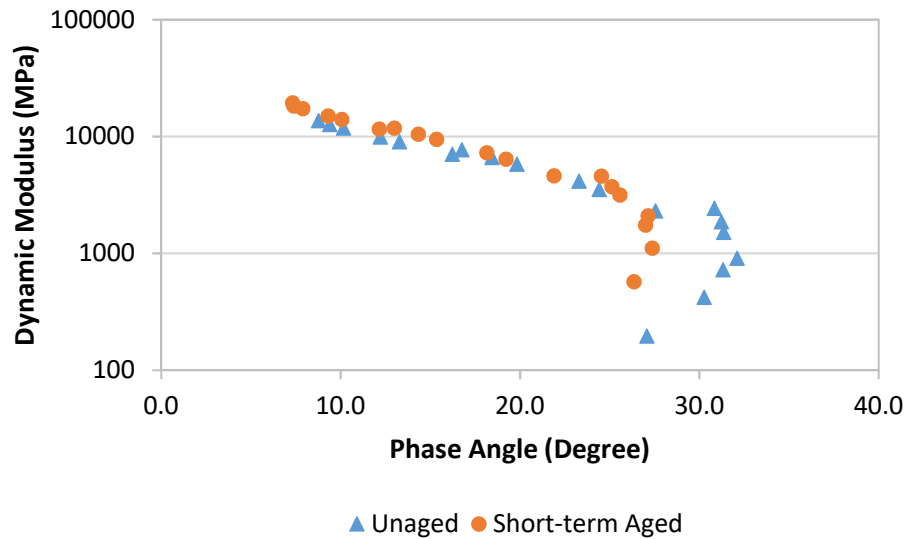


Figure 5.18 Mixture Aging Viscoelastic Properties in Black Space Diagram

The dynamic modulus master curve is constructed using the CAM model (Equation 5.39). The phase angle master curve is developed using β model (Zhang et al. 2014), which is shown in Equation 5.40. The β model is a non-symmetrical model that can fit the measured data of phase angle accurately.

$$|E^*(\omega)| = \frac{E_g}{\left[1 + \left(\frac{\omega_{cE}}{\omega a_T}\right)^{\frac{\log 2}{R_E}}\right]^{\frac{R_E}{\log 2}}} \quad (5.39)$$

$$\delta(\omega) = \frac{\delta_{\max}}{\text{Exp}\left\{\left(\frac{\beta+1}{\beta}\right)\left[\left(\frac{k\omega_{cE}}{\omega a_T}\right)^\beta - 1\right]\right\}\left(\frac{\omega a_T}{\omega_R}\right)^{\beta+1}} \quad (5.40)$$

where δ_{\max} is the maximum phase angle in degree; ω_{cE} is the reduced frequency, rad/s; k is the ratio between the frequency at the phase angle δ_{\max} to the ω_{cE} ; a_T is the time-temperature shift factor; ω is the frequency for a single test; β is the fitting parameter.

The dynamic modulus $|E^*(\omega)|$ can be related to the corresponding phase angle $\delta(\omega)$, as shown in Equations 5.41 and 5.42.

$$\delta(\omega) = \frac{\delta_{\max}}{\text{Exp}\left\{\left(\frac{\beta+1}{\beta}\right)\left[(kx)^\beta - 1\right]\right\}\left(\frac{1}{x}\right)^{\beta+1}} \quad (5.41)$$

$$\text{where } x = \frac{\omega_R}{\omega \cdot a_T} = \left\{\left[\frac{E_g}{E^*(\omega)}\right]^\gamma - 1\right\}^{\frac{1}{\gamma}}, \quad \gamma = \frac{\log 2}{R}. \quad (5.42)$$

The dynamic modulus and phase angle at different temperatures and frequencies are first measured and the master curves are constructed using the CAM model and the β model, respectively. The parameters E_g , k , R_E , ω_{cE} , δ_{\max} and β are obtained after constructing the master curves for dynamic modulus and phase angle. With the known

phase angles at different temperatures and frequencies, the endurance limit can be back-calculated using the Equations 5.37, 5.38, 5.41 and 5.42.

Using the above method, an example of the black space diagram is presented in Figure 5.19 with different air void contents. As air void content increases from 4% to 7%, the asphalt material is less resistant to cracking. It is shown that for the low phase angle part in the “no cracking zone”, the modulus also should be low, which indicates that a mixture with a high modulus and a low phase angle is more prone to crack. It is expected that such a mixture can be either long-term aged which becomes brittle, or a mixture placed at a very low temperature and susceptible to thermal cracking. It is known that an asphalt material becomes brittle and loses the stress relaxation ability after long-term aging. Meanwhile, for the mixture at a very low temperature, if the thermal stress exceeds the tensile strength, a thermal crack initiates at the surface of the pavement. As phase angle increases, the “no cracking” zone also increases, it indicates that the modulus of the material can have a wider range with a higher phase angle than that with a lower phase angle shown in the “no cracking zone”. The bond energy is also another important effect on the endurance limit. Based on Equations 5.41 and 5.42, it is expected that as the bond energy increases, the failure line also moves to above to allow a larger “no cracking” area. The increases of glassy modulus also causes the endurance limit decrease, which indicates the aging effect could reduce the fracture resistance.

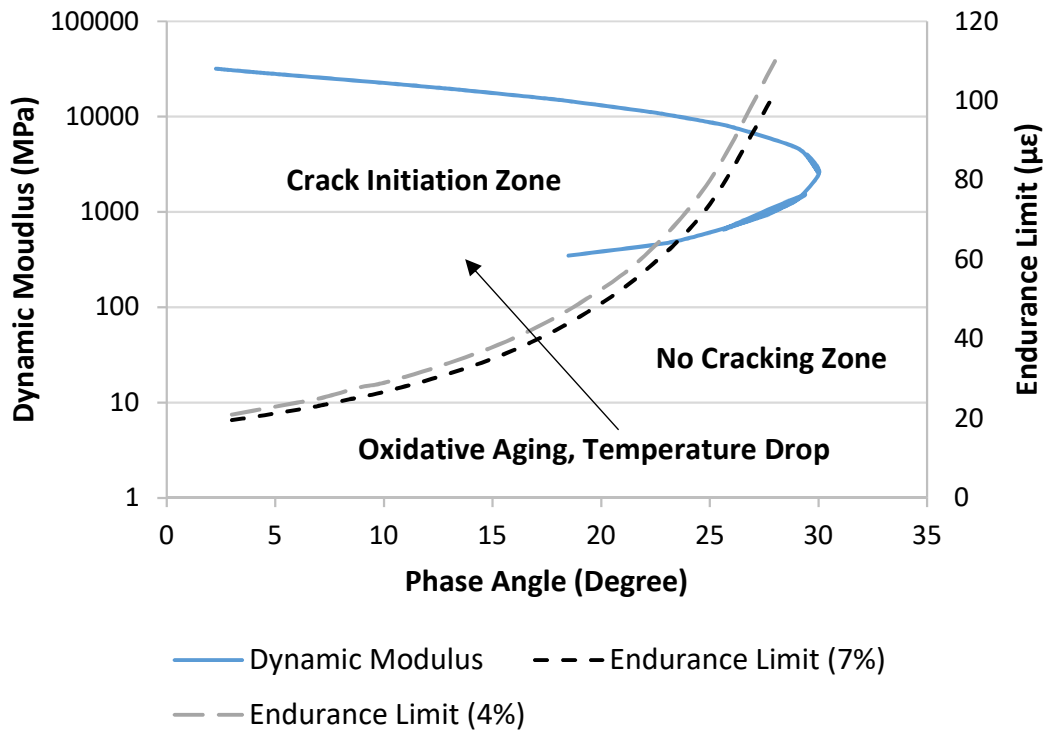


Figure 5.19 Black Space Diagram for Cracking Initiation

It should be noted that the dynamic modulus in Figure 5.19 is measured with compressive loading in accordance with AASHTO T 342-11. In fact, based on the concept of the endurance limit, the crack initiates under tensile stress, however, the tensile modulus and compressive modulus for the same mixture are different in both the magnitude and phase angle due to the isotropic and anisotropic properties. Figure 5.20 shows the tensile and compressive moduli of the same asphalt mixture. It is obvious that if the similar “crack initiation line” is drawn in figure 5.19, the area of “no cracking” zone for the tensile modulus is much larger than which for the compressive modulus.

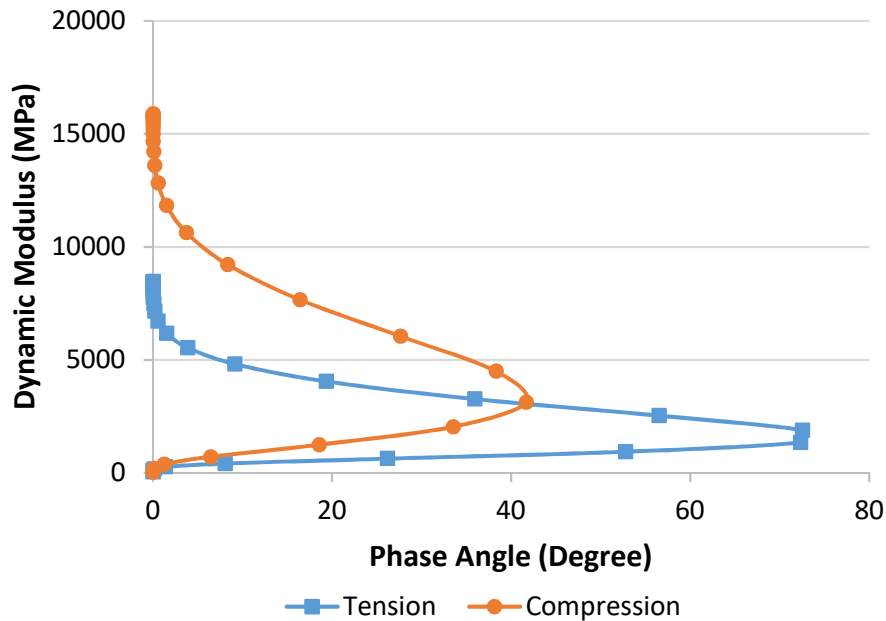


Figure 5.20 Tensile and Compressive Dynamic Modulus

Figures 5.19 and 5.20 can be used as an effective pavement design tool, which helps determine the durability of the asphalt materials and rank the fracture resistance for aging-induced cracking and thermal-induced cracking. It also provides highway agencies a direct guide to choose the desired asphalt mixtures for the long lasting or perpetual pavement design.

5.7 Development of C# Computer-Aided Program for TDC

A computer-aided program using the C# language in Microsoft Visual Studio is developed to calculate the number of days to reach the critical crack depth for both the traffic loading and thermal loading, which are used in the calibration and validation process. Specifically, the ANN models used to calculate the thermal and traffic induced

J -integral are coded in this computer program as well as all of the required inputs for TDC pavement design. The interface for the calibration program is shown in Figure 5.21. It includes three main parts: 1) general information; 2) Inputs (Traffic, Climate, and Structure & Material Properties); 3) Results.

User can save a new project or open and read an existing project from this interface. When user finishes one part, the red bottom becomes green, which means this part is finished. The change of color is helpful to remind user that this part is finished or unfinished, especially for some input parts which have much more information needed to be entered such as the asphalt layer properties and cannot be left as blank.

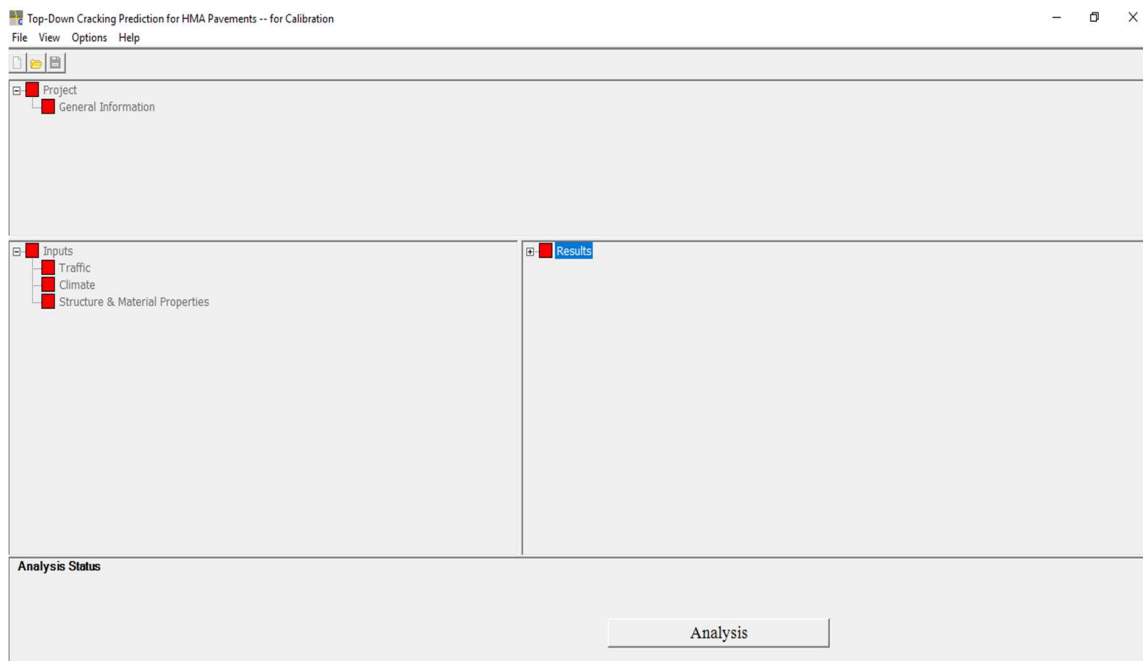


Figure 5.21 Interface of Computer Program

The interface of general information is illustrated in Figure 5.22. It includes the design life and construction time (also the traffic open time). The design life is the number

of days from the construction time to the time when the crack reaches 100 mm deep. The construction time is necessary since it is important to know the weather and temperature at the construction time and from the construction time to the end of the design pavement life.

The image shows a software dialog box titled "General Information". It contains several input fields and controls:

- Project Name:** A text box containing "Project1".
- Type of Pavement Structure:** A section with a radio button selected for "AC/BASE/SUBGRADE".
- Design Life (years):** A spin box set to "20".
- Construction Information:** A sub-section containing:
 - Asphalt layer construction month:** A dropdown menu set to "May".
 - Year:** A dropdown menu set to "2017".
- Buttons:** "OK" and "Cancel" buttons at the bottom.

Figure 5.22 Interface of General Information

The interface of traffic is shown in Figures 5.23(a) and (b) for the two input levels, respectively. As detailed previously, the traffic has eight categories based on the vehicle class, number of tires, and number of axles. There are two levels for the traffic input, one is the AADTT which is used for the sections without the WIM information (Figure 5.23(a)). Another one is using the load spectra model (Figure 5.23(b)), if user has a knowledge of the number of vehicles in each of the eight traffic categories. The vehicle speed is used to take into account the time-dependent nature of the asphalt materials such as the dynamic modulus and the healing effect. The annual traffic increase rate is also a

user's input to consider the change of the annual traffic number, which has an influence on the calculations of TDC fatigue life.

Vehicle Class	Single Axle	Tandem Axle	Tridem Axle	Quad Axle
4	No. 1	No. 3	No. 5	No. 7
5				
6	No. 2	No. 4	No. 6	No. 8
7				
8				
9				
10				
11				
12	Dual Tires			
13				

Traffic Input Mode

Annual Average Daily Truck Traffic (AADTT)
 Annual Number of Axles (ANA) for each category

AADTT:

Operation Speed (mph)
Yearly ANA Growth (%)

(a)

Figure 5.23 Interface of Traffic Load: (a) AADTT Input, (b) Load Spectra Input

Traffic Load Input

Vehicle Class	Single Axle	Tandem Axle	Tridem Axle	Quad Axle			
4	No. 1	No. 3 Single Tire No. 5		No. 7			
5		Dual Tires					
6							
7							
8							
9							
10	No. 2				No. 4	No. 6	No. 8
11							
12							
13							

Traffic Input Mode

Annual Average Daily Truck Traffic (AADTT)
 Annual Number of Axles (ANA) for each category

Category No.1	263778	Category No.3	2562	Category No.5	0	Category No.7	0
Category No.2	346655	Category No.4	433087	Category No.6	53794	Category No.8	0

Operation Speed (mph)
 Yearly ANA Growth (%)

(b)

Figure 5.23 Continued

The climate data input is shown in Figure 5.24. User can either load the existing climate data file that was previous developed or create a new climate data file by choosing the climate data from weather stations in different climatic zones in the United States. The weather data can either be rolled from the construction year to the year at the end of design life or only be a specific year as a default one, based on the user's need and availability of the weather station historical data.

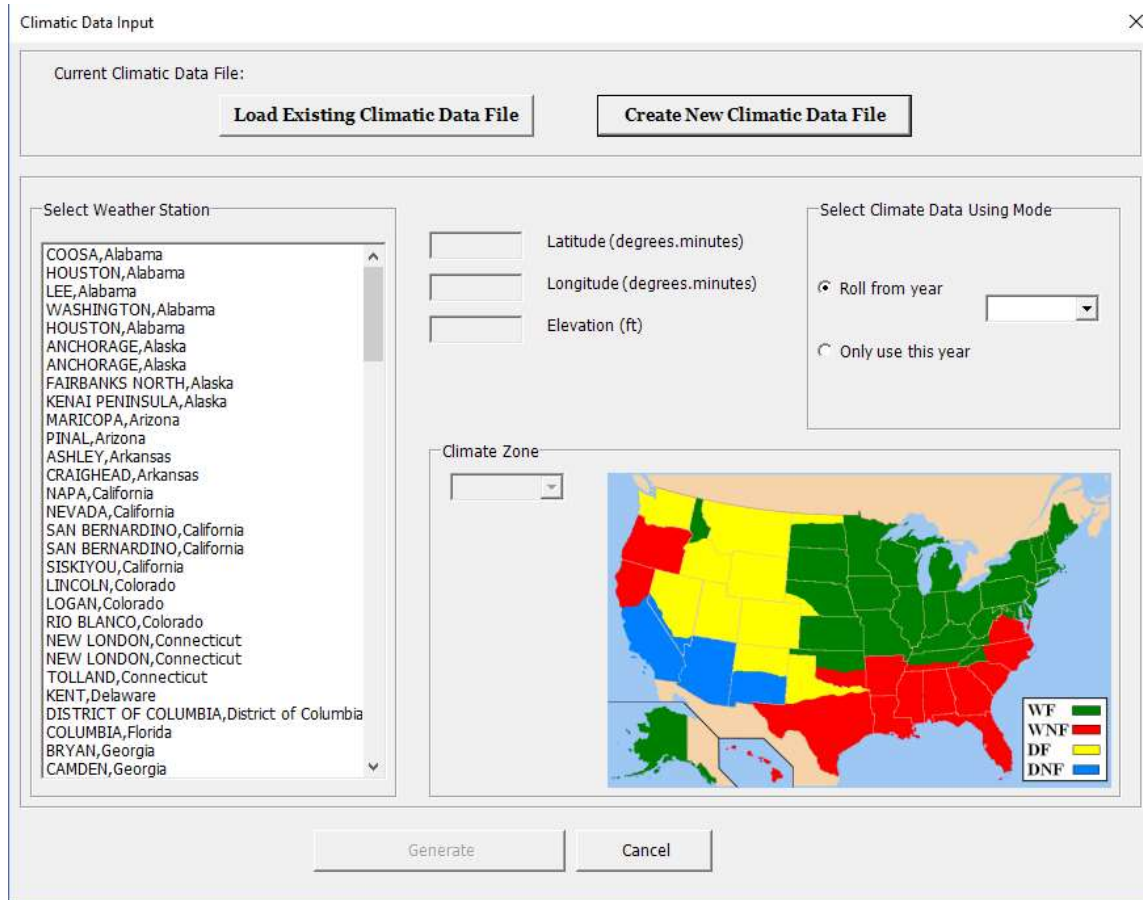


Figure 5.24 Interface of Weather Station Selection

The pavement structure and material properties is shown in Figure 5.25. This is a typical three layer pavement system including an asphalt layer, a base layer and a subgrade layer. As discussed previously, the method of equivalent thickness is used to reduce the number of layers.

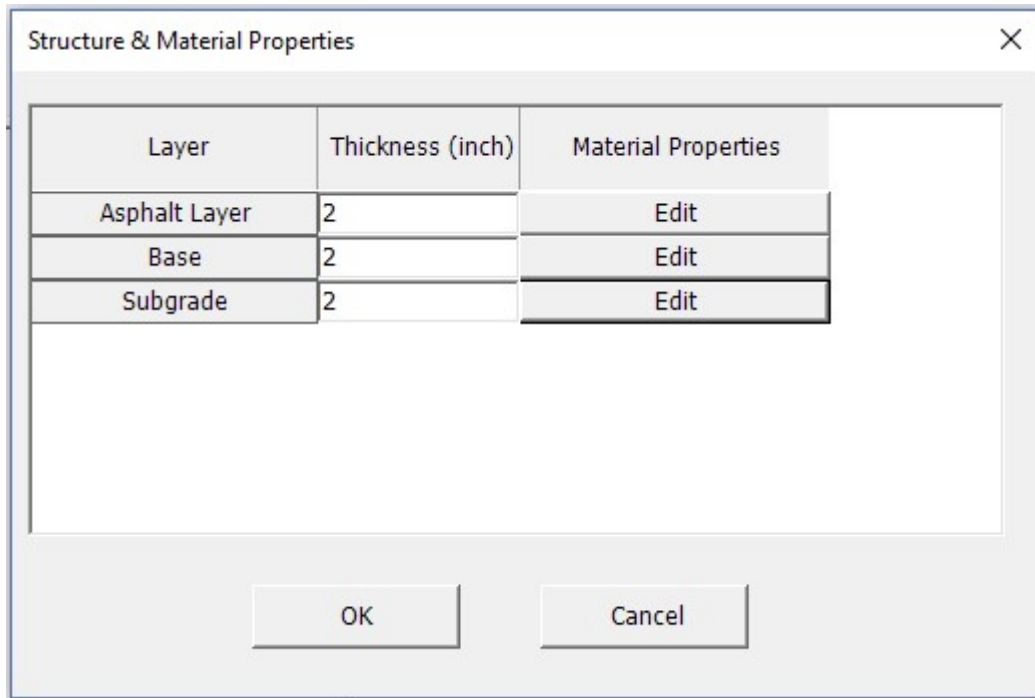


Figure 5.25 Interface of Structure and Material Properties

The asphalt material properties is illustrated in Figure 5.26. The thermal contraction coefficient is used to calculate the thermal strain with the temperature change. The binder property, aggregate gradation, air voids content and binder content are utilized to predict the unaged dynamic modulus using either the NCHRP 1-37A Viscosity based model or the NCHRP 1-40D G^* based model. The aging shift functions are used to predict the aged dynamic modulus. The relaxation properties with the aggregate gradation are utilized to predict the fracture properties (A' and n') based on the material properties when the fatigue test result is not available.

Asphalt Material Properties ×

Thickness (inch): Thermal Contraction Coefficient (1e-6 in/in/F):

HMA E* Predictive Model

NCHRP 1-37A Viscosity based model (1999) NCHRP 1-40D G* based model (2006)

FWD Data

FWD Modulus (ksi): FWD Test Temperature (F):

Binder Property

Level 3 | Level 2 | Level 1

CAM Model Parameters:

Gg (GPa): Wm (rad/s): R:

C1: C2: Td (C):

Fracture Property

Level 3 | Level 2 | Level 1

A: n':

Aggregate Gradation

% Retained 3/4 inch Sieve:

% Retained 3/8 inch Sieve:

% Retained #4 Sieve:

% Passing #200 Sieve:

Volumetric properties

Air Void ()

VBE (%):

Relaxation properties

E1

m:

Mixture Aging Properties

Aging Parameters:

n: As: Ab: An:

k: Eas: Eab: Ean:

OK Cancel

Figure 5.26 Interface of Asphalt Material Properties

The base and subgrade layers have similar input forms, as shown in Figures 5.27 and 5.28. In general, the moduli of the two layers can vary with monthly values as the level one input. The level two input is a constant typical modulus value for the base and subgrade layers when the monthly modulus data is not available or beyond user's knowledge.

Thickness (inch):

Poisson Ratio:

Modulus Input

Level 2: Typical Value Level 1: Monthly Value

Month	Modulus (ksi)
Jan.	200
Feb.	200
Mar.	200
Apr.	200
May	200
June	200
July	200
Aug.	200
Sep.	200
Oct.	200
Nov.	200
Dec.	200

Figure 5.27 Monthly Modulus Values for Level One

Unbound Material ×

Thickness (inch): Poisson Ratio:

Modulus Input

Level 2: Typical Value Level 1: Monthly Value

Typical Modulus (ksi):

Figure 5.28 Typical Modulus Value for Level Two

6. SUMMARIES, CONCLUSIONS AND RECOMMENDATIONS

Top-down cracking (TDC) is one of the major distress modes in asphalt pavements, which has drawn tremendous attention worldwide. The aim of this study is to develop of a calibrated and validated mechanistic-empirical model to predict the initiation and propagation of TDC in asphalt pavements. Such a model could contribute greatly to the understanding of TDC and associated pavement design.

6.1 Summaries and Conclusions

In this study, a systematic mechanistic-empirical TDC model is developed based on the aging viscoelastic properties and viscoelastic fracture mechanics. After several sub-models are proposed relevant to the factors of materials, structure, traffic and climate, the generated model is then calibrated and validated using the field data for over 200 pavement sections across four different climatic zones in the United States. This model consists of several mechanical, empirical, numerical and ANN models to predict the TDC initiation time and fatigue lives of an asphalt pavement due to traffic and thermal loads. After all of the mechanical and FEM models are ready, multiple ANN models are developed to calculate the fracture parameter J -Integral for predicting the daily crack growth due to different traffic load levels and thermal loading at different temperature drops or cycles. After the model is calibrated and validated, a computer program is developed to compute the distress parameters ρ and β for each climatic zone, and the TDC performance can be evaluated with the corresponding parameters. These results are based on the three-layered system, so the concept of equivalent thickness is used if additional pavement layers such

as a subbase layer is actually constructed. The calibration coefficients α_0 , α_1 , γ_0 , and γ_1 can also be obtained and utilized for highway agencies to develop a regional or local version of the TDC performance analysis and design by following the similar procedure proposed in this study. This model is then coded in the C# language and expected to run as a stand-alone program or a subroutine of the AASHTOware Pavement ME Design.

In this dissertation, Chapter 2 presents the characterization of complex modulus gradient of the field-aged asphalt mixtures based on the linear viscoelastic theory, correspondence principle, pseudo strain, and bending beam theory. Direct tension test is conducted on the field core specimens to measure the strains at three different locations (top, center and bottom). With the aid of the correspondence principle, bending beam theory, and pseudo strain, the complex modulus at each side of the specimen can be calculated. The test results indicate that the modulus gradient is developed during the long-term field aging process, which is a unique feature of field-aged asphalt mixtures. This property becomes extremely important for the TDC analysis since as the surface layer becomes highly aged, it is more susceptible to surface distress.

In Chapter 3, the dynamic modulus master curves of laboratory-aged and field-aged asphalt mixtures are constructed using the modified version of CAM model. Rheological index and glassy modulus are identified to be functions of aging time, and they are shape factor and magnitude factor of the master curve, respectively. Two aging shift functions are developed in this chapter: long-term aging shift function and depth shift function. The long-term aging shift function is a function of aging time, aging acceleration parameter, aging temperature and activation energy. This aging function is an effective

tool to predict the dynamic modulus master curve after long-term aging, and it is applicable to both types of asphalt mixtures aged in the laboratory or in the field. The depth shift function is developed to characterize the non-uniform aging that is exclusive for field-aged asphalt mixtures and is a function of pavement depth. Once the moduli at three different depths and aging times is known from the method in Chapter 2, the modulus at any other depths and aging times can be predicted using the depth shift function and long-term aging shift function. The linear viscoelastic properties of field-aged asphalt mixtures after long-term field aging can be characterized using this method.

Chapter 4 details the procedures of the development of FEM and ANN models, which are utilized to calculate the fracture parameter J -integral. Both of the two models include the effects of modulus gradient, long-term aging, non-uniform tire pavement contact stresses, different pavement structures and material properties. An UMAT is developed in FORTRAN to model the modulus gradient due to aging and temperature effects. It is seen that the J -integral is not uniformly distributed within pavement depth from the FEM model. The ANN models are developed in MATLAB based on the database generated from the FEM models, and both of the ANN model and FEM model have the same inputs and output. The calculated J -integral from ANN model is used to determine the daily crack growth due to traffic loading and thermal loading for each LTPP pavement section.

The calibrated and validated TDC model is presented in Chapter 5. LTPP data for four climatic zones within the United States is collected including the traffic data, temperature data, pavement structure data, distress data and material property data. Each

of them is characterized by a specific sub-model. TDC initiation and propagation models are developed based on the fracture mechanics and cumulative damage models, which are then calibrated and validated using the LTPP data. The fracture endurance limit is also calculated using the repeated direct tension test, and it varies with temperature, frequency, air void content, binder content and bond energy. The determined endurance limit is also used in the black space diagram to show the “no cracking” zone and “crack initiation” zone to evaluate the aging resistance and thermal resistance of the asphalt mixtures. The diagram can be used as a pavement design tool to rank the fracture resistances. Finally, a C# language computer program is developed in Microsoft Visual Studio to calculate the number of days to reach the 100 mm crack depth by traffic loading and thermal loading, respectively. The distress parameters ρ and β and the calibration coefficients α_0 , α_1 , γ_0 , and γ_1 for each climate zone are then determined, and they can be utilized for the TDC pavement design in a given climatic zone.

6.2 Recommendations

A mechanistic-empirical TDC model is developed in this dissertation. The field aging effect on viscoelastic properties of asphalt mixtures is well determined by conducting tests on field-aged cores. The aged dynamic modulus of asphalt mixtures can be predicted using the two aging shift functions. FEM and ANN models are constructed to calculate the fracture parameter J -integral. The calculation results are used in the Paris' law to determine the daily crack growth for each pavement section, which are calibrated and validated using LTPP data. An endurance limit prediction model is also proposed

using fracture mechanics and then plotted in the black space diagram for better illustration and materials comparison. In addition, some recommendations are proposed as follows based on the author's understanding:

- Some mechanical models have numerous equations, which may be time-consuming for practitioners. It is suggested to make a simplification but without decreasing the acceptable accuracy.
- The viscoelastic property is not taken into account for the asphalt layer in the FEM and ANN. It is preferred to develop another UMAT to consider the viscoelastic non-uniform aging effect for the asphalt layer and the actual traffic speed, although it will undoubtedly reduce the calculation speed in both of the FEM and ANN models.
- For the endurance limit prediction model, a large number of replicates with different bond energies and air void contents is preferred, which are tested at different temperatures and frequencies in order to determine the precision of the model. A rest period is suggested between loading cycles to account for the healing effect and make this model more robust.

REFERENCES

- AASHTO (2006). *Standard specification for mixture conditioning of hot mix asphalt (HMA)*. AASHTO R30-02. American Association of State Highway and Transportation Officials: Washington, D.C.
- AASHTO (2008a). *Determining Dynamic Modulus of Hot-Mix Asphalt Concrete Mixtures*. AASHTO TP 62. Standard Specifications for Transportation and Methods of Sampling and Testing, 28th Edition, and Provisional Standards. American Association of State Highway and Transportation Officials: Washington, D.C.
- AASHTO (2008b). *Mechanistic-empirical pavement design guide. A manual of practice, interim edition*. American Association of State Highway and Transportation Officials: Washington, D.C.
- Abu Al-Rub, R.K., Darabi, M.K., Kim, S.M., Little, D.N., Glover, C.J. (2013). “Mechanistic-based constitutive modeling of oxidative aging in aging-susceptible materials and its effect on the damage potential of asphalt concrete.” *Construction and Building Materials*, No.41, 439–454.
- Anderson, T. L. (2005). *Fracture Mechanics: Fundamentals and Applications*. CRC Press.
- Archilla, A.R. (2015). “Top-Down Fatigue Cracking in High-Temperature Environments.” *Transportation Research Record: Journal of the Transportation Research Board*, No. 2507, pp. 128–137.
- Baladi, G.Y., Schorsch, M., and Svasdisant, T. (2003). *Determining the Causes of Top-Down Cracks in Bituminous Pavements*. Michigan State University, East Lansing.
- Bell, C.A. (1989). *SHRP-A-305: Summary Report on Aging of Asphalt-Aggregate Systems*. National Research Council, Washington, D.C.
- Bennert, T. (2014). *Rejuvenating agents with RAP in HMA – quarterly meeting presentation*. Trenton, NJ: Department of Transportation.
- Buttlar, W.G., Paulino, G.H., and Song, S.H. (2006). “Application of graded finite elements for asphalt pavements.” *Journal of engineering mechanics*, 132(3), 240-249.
- Carpenter, S. H., Ghuzlan, K. A., and Shen, S. (2003). “Fatigue Endurance Limit for Highway and Airport Pavements.” *Transportation Research Record: Journal of the Transportation Research Board*, No. 1832, Transportation Research Board of the National Academies, Washington, D.C., pp. 131–138.

Daniel, J., Kim, Y., and Lee, H. J. (1998). "Effects of aging on viscoelastic properties of asphalt-aggregate mixtures." *Transportation Research Record: Journal of the Transportation Research Board*, No.1630, 21-27.

De Beer, M., Fisher, C., and Jooste, F.J. (1997). "Determination of Pneumatic Tyre/Pavement Interface Contact Stresses Under Moving Loads and Some Effects on Pavements with Thin Asphalt Surfacing Layers." *In Proceedings of the 8th International Conference on Asphalt Pavements*, pp. 10–14.

Dinegdae, Y. H., Onifade, I., Jelagin, D., and Birgisson, B. (2015). "Mechanics-based top-down fatigue cracking initiation prediction framework for asphalt pavements." *Road Materials and Pavement Design*, 16(4), 907-927.

Epps, J. A., and Monismith, C. L. (1972) "Fatigue of Asphalt Concrete Mixtures—Summary of Existing Information in Fatigue of compacted bituminous aggregate mixtures." *ASTM International*.

Farrar, M., Harnsberger, P., Thomas, K., Wiser, W. (2006) "Evaluation of oxidation in asphalt pavements test sections after four year of service." *International Conference on Perpetual Pavement*, Western Research Institute.

Findley, W.N., Lai, J.S., and Onaran, K. (1989). *Creep and relaxation of nonlinear viscoelastic materials: with an introduction to linear viscoelasticity*. Dover Publications, New York.

Gerritsen, A.H., Van Gorp, C., Van der Heide, J., Molenaar, A., and Pronk, A. (1987). "Prediction and Prevention of Surface Cracking in Asphaltic Pavements." *In Proceedings of the 6th International Conference, Structural Design of Asphalt Pavements*, Vol. 1, University of Michigan, Ann Arbor, July 13–14, pp. 378–391.

Glover, C. J., Davison, R. R., Domke, C. H., Ruan, Y., Juristyarini, P., Knorr, D. B., and Jung, S. H. (2005). *Development of a new method for assessing asphalt binder durability with field validation: Technical Report*. Publication FHWA/TX-05/1872-2. Texas A&M Transportation Institute, College Station.

Glover, C.J., Liu G, Rose, A.A., Tong, Y., Gu, F., Ling, M., Arambula, E., Estakhri, C., and Lytton, R.L. (2014). *Evaluation of binder aging and its influence in aging of hot mix asphalt concrete: Technical Report*. Publication FHWA/TX-14/0- 6613-1. Texas A&M Transportation Institute, College Station.

Harmelink, D., Shuler, S., and Aschenbrener, T. (2008). "Top-down cracking in asphalt pavements: causes, effects, and cures." *Journal of Transportation Engineering*, 134(1), 1-6.

- Harvey, J. T., and Tsai, B.-W. (1996). "Effects of Asphalt Content and Air Void Content on Mix Fatigue and Stiffness." *Transportation Research Record: Journal of the Transportation Research Board*, No.1543, 38–45.
- Hu, S., Hu, X., Zhou, F., and Walubita, L. (2008). "SA-CrackPro: New finite element analysis tool for pavement crack propagation." *Transportation Research Record: Journal of the Transportation Research Board*, No. 2068, 10-19.
- Kandhal, P.S. (1977). "Low-Temperature Ductility in Relation to Pavement Performance." In ASTM STP 628: Low-Temperature Properties of Bituminous Materials and Compacted Bituminous Paving Mixtures, C.R. Marek (Ed.), *American Society for Testing and Materials*, Philadelphia, PA, pp. 95-106.
- King, G., Anderson, M., Hanson, D., and Blankenship, P. (2012). "Using black space diagrams to predict age-induced cracking." In *7th RILEM International Conference on Cracking in Pavements*, pp. 453-463. Springer Netherlands.
- Kuai, H., Lee, H., Zi, G., and Mun, S. (2009). "Application of generalized j-integral to crack propagation modeling of asphalt concrete under repeated loading." *Transportation Research Record: Journal of the Transportation Research Board*, No.2127, 72-81.
- Kumara, M. W., Gunaratne, M., Lu, J. J., and Dietrich, B. (2004). "Methodology for random surface-initiated crack growth prediction in asphalt pavements." *Journal of materials in civil engineering*, 16(2), 175-185.
- Kutay, M., Gibson, N., Youtcheff, J., and Dongré, R. (2009). "Use of small samples to predict fatigue lives of field cores: Newly developed formulation based on viscoelastic continuum damage theory." *Transportation Research Record: Journal of the Transportation Research Board*, No.2127, 90-97.
- Levenberg, E., and Uzan, J. (2004). "Triaxial small-strain viscoelastic-viscoplastic modeling of asphalt aggregate mixes." *Mechanics of Time-Dependent Materials*, 8(4), 365-384.
- Ling, M., Luo, X., Gu, F., and Lytton, R. L. (2017a). An inverse approach to determine complex modulus gradient of field-aged asphalt mixtures. *Materials and Structures*, 50(2), 138.
- Ling, M., Luo, X., Hu, S., Gu, F., and Lytton, R. L. (2017b). "Numerical Modeling and Artificial Neural Network for Predicting J-Integral of Top-Down Cracking in Asphalt Pavement." *Transportation Research Record: Journal of the Transportation Research Board*, No. 2631, 83-95.

- Little, D.N., Lytton, R.L., Williams, D., and Chen, C.W. (2001). *Microdamage Healing in Asphalt and Asphalt Concrete, Volume I: Microdamage and Microdamage Healing Project Summary Report*. FHWA-RD-98-141. U.S. Department of Transportation.
- Lolly, R. (2013). Evaluation of short term aging effect of hot mix asphalt due to elevated temperatures and extended aging time. Arizona State University.
- Luo, R., and Lytton, R. L. (2010). “Characterization of the tensile viscoelastic properties of an undamaged asphalt mixture.” *Journal of Transportation Engineering*, 136(3), 173-180
- Luo, X., Luo, R., and Lytton, R. L. (2013). “Characterization of fatigue damage in asphalt mixtures using pseudostrain energy.” *Journal of Materials in Civil Engineering*, 25(2), 208-218.
- Luo, X., Zhang, Y., and Lytton, R.L. (2016). “Implementation of pseudo J-integral based Paris’ law for fatigue cracking in asphalt mixtures and pavements.” *Material and Structures* 49(9):3713–3732.
- Lytton, R.L., J. Uzan, Fernando, E.G., Roque, R., Hiltunen, D., and Stoffels, S. M. (1993). *Development and Validation of Performance Prediction Models and Specifications for Asphalt Binders and Paving Mixes. Report SHRPA-357*. Strategic Highway Research Program, National Research Council, Washington, D.C.
- Lytton, R. L., Tsai, F. L., Lee, S. I., Luo, R., Hu, S., and Zhou, F. (2010). *Models for predicting reflection cracking of hot-mix asphalt overlays*. NCHRP 1-41: National cooperative highway research program, transportation research board, National Research Council, Washington, D.C.
- Lytton, R. L., Gu, F., Zhang, Y., and Luo, X. (2017). “Characteristics of undamaged asphalt mixtures in tension and compression.” *International Journal of Pavement Engineering*, 1-13.
- Mirza, M.W. and Witczak, M.W. (1995). “Development of a global aging system for short and long term aging of asphalt cements.” *J. Assoc. Asphalt Paving Technol.* No.64, 393–418.
- Marasteanu, M. O., and Anderson, D. A. (1999). “Improved model for bitumen rheological characterization.” *Eurobitume Workshop on Performance Related Properties for Bituminous Binders*, Luxembourg, Paper No. 133.
- Masad, E., Huang, C.W., Airey, G., Muliana, A. (2008). “Nonlinear viscoelastic analysis of unaged and aged asphalt binders.” *Construction and Building Materials*. 22 (11). 2170–2179.

Matsuno, S., and Nishizawa, T. (1992). “Mechanism of Longitudinal Surface Cracking in Asphalt Pavement.” *In Proceedings of the 7th International Conference on Asphalt Pavements*, Nottingham, United Kingdom, pp. 277–291.

Miller, J. S. and Bellinger, W. Y. (2003). *Distress identification manual for the long-term pavement performance program*. No. FHWA-RD-03-031.

Monismith, C. L., and McLean, D. B. (1972). “Structural design considerations.” *Proc. Assoc. Asphalt Paving Tech.*, 41, 258–304.

Myers, L.A., Roque R., and Ruth, B.E. (1998). “Mechanisms of Surface Initiated Longitudinal Wheel Path Cracks in High-Type Bituminous Pavements.” *Electronic Journal of the Association of Asphalt Paving Technologists*, Vol. 67, 1998, pp. 401–432.

NCHRP 1-37A (2004). *Guide for mechanistic-empirical design of new and rehabilitated pavement structures*. National Cooperative Highway Research Program, Transportation Research Board, National Research Council, Washington, D.C.

NF EN 12697-26 (2004). *Bituminous mixtures: test methods for hot mix asphalt—Part 26: Stiffness*.

Norouzi, A., Sabouri, M., and Kim, Y.R (2016). “Fatigue life and endurance limit prediction of asphalt mixtures using energy-based failure criterion.” *International Journal of Pavement Engineering*, 1-14.

Odemark, N. (1949). *Investigations as to the Elastic Properties of Soils and Design of Pavements According to the Theory of Elasticity*, vol. 77. Statens Vaginstutete: Meddelande, Stockholm, Sweden.

Ozer, H., Al-Qadi, I.L., and Duarte, C.A. (2011). “Effects of Nonuniform and Three-Dimensional Contact Stresses on Near-Surface Cracking.” *Transportation Research Record: Journal of the Transportation Research Board*, No. 2210, pp. 97–105.

Paris, P. C. and Sih, G. C. (1965). “Stress Analysis of Cracks.” *Fracture Toughness Testing and Its Applications: A Symposium Presented at the Sixty-Seventh Annual Meeting*, American Society for Testing and Materials, Chicago, III, June 21-26.

Park, H. and Kim, Y.R. (2013). “Investigation into top-down cracking of asphalt pavements in North Carolina.” *Transportation Research Record: Journal of the Transportation Research Board*, No. 2368, pp. 45–55.

Pavementinteractive 2012 (1). <http://www.pavementinteractive.org/top-down-cracking/>

Pavementinteractive 2012 (2). <http://www.pavementinteractive.org/flexural-fatigue/>

- Pellinen, T., Rowe, G., and Biswas, K. (2004). *Evaluation of Surface (Top Down) Longitudinal Wheel Path Cracking*. Publication FHWA/IN/JTRP-2004/06. Joint Transportation Research Program, Indiana Department of Transportation and Purdue University, West Lafayette.
- Roque, R., Birgisson, B., Drakos, C., and Dietrich B. (2004). “Development and field evaluation of energy-based criteria for top-down cracking performance of hot mix asphalt (with discussion).” *J. Assoc. Asphalt Paving Technol.* 73.
- Roque, R., Zou, J., Kim, Y.R., Baek, C., Thirunavukkarasu, S., Underwood, B.S., and Guddati, M.N. (2010). *NCHRP Web-Only Document 162: Top-Down Cracking of Hot-Mix Asphalt Layers: Models for Initiation and Propagation*. Transportation Research Board of the National Academies, Washington, D.C.
- Rowe, G. (2011). Prepared discussion to Anderson, R. M., King, G. N., Hanson, D. I., and Blankenship, P. B. “Evaluation of the relationship between asphalt binder properties and non-load related cracking.” *J. of the Assoc. of Asphalt Paving Technologists*, 80, 615-663.
- Schapery, R.A. (1961). “Two simple approximate methods of Laplace transform inversion for viscoelastic stress analysis.” Guggenheim Aeronautical Laboratory, California Institute of Technology, Pasadena.
- Schapery, R.A. (1984). “Correspondence principle and a generated J integral for large deformation and fracture analysis of viscoelastic media.” *International Journal of Fracture* 25(3):195–223.
- Shell Pavement Design Manual. (1978). *Asphalt Pavements and Overlays for Road Traffic*. Shell International Petroleum Co., Ltd., London.
- Souliman, M. (2012). Integrated Predictive Model for Healing and Fatigue Endurance Limit for Asphalt Concrete. Arizona State University, Tempe.
- Svasdisant, T., Schorsch, M., Baladi, G.Y., and Pinyosunun, S. (2002). “Mechanistic Analysis of Top-Down Cracks in Asphalt Pavements.” *Transportation Research Record: Journal of the Transportation Research Board*, 1809, pp. 126–136.
- Asphalt Institute Thickness Design Manual. (1982). *Research Report 82-2*. Asphalt Institute, Lexington, KY.
- TxDOT (2004). *Standard specifications for construction and maintenance of highways, streets, and bridges*. Texas Department of Transportation, Austin, TX.

Uhlmeier, J.S., Willoughby, K., Pierce, L.M., and Mahoney, J.P. (2000). “Top-Down Cracking in Washington State Asphalt Concrete Wearing Courses.” *Transportation Research Record: Journal of the Transportation Research Board*, No. 1730, pp. 110–116.

Wang, H., Ozer, H., Al-Qadi, I.L., and Duarte, C.A. (2013). “Analysis of NearSurface Cracking under Critical Loading Conditions Using Uncracked and Cracked Pavement Models.” *Journal of Transportation Engineering*, Vol. 139, No. 10, pp. 992–1000.

Witczak, M., Mamlouk, M., Souliman, M., and Zeiada, W. (2013). *NCHRP Project 9-44A: Laboratory validation of an endurance limit for asphalt pavements*. National Cooperative Highway Research Program, Transportation Research Board, National Research Council, Washington, D.C.

Zeida, W.A. (2012). *Endurance Limit for HMA Based on Healing Phenomenon Using Viscoelastic Continuum Damage Analysis*. Arizona State University, Tempe.

Zhang, Y., Luo, R., and Lytton, R.L. (2012). “Characterizing permanent deformation and fracture of asphalt mixtures by using compressive dynamic modulus tests.” *Journal of Materials in Civil Engineering*, 24(7):898–906.

Zhang, Y., Luo, X., Luo, R., and Lytton, R.L. (2014). “Crack initiation in asphalt mixtures under external compressive loads.” *Construction and Building Materials*. 72 (72) 94–103.

Zhou, F., Hu, S., Hu, X., Scullion, T., Mikhail, M., and Walubita, L.F. (2010). “Development, Calibration, and Verification of a New Mechanistic-Empirical Reflective Cracking Model for HMA Overlay Thickness Design and Analysis.” *Journal of Transportation Engineering*, Vol. 136, No. 4, pp. 35.

APPENDIX A

Aggregate Gradation of Field Specimens:

AGREGATE BIN FRACTIONS										
	Bin No.1		Bin No.2		Bin No.3		Bin No.4		Bin No.5	
Source	Limestone		Limestone		Limestone		Limestone		Gravel	
Sample ID	Type C		Type D		Type F		Mfg. Sand		Field Sand	
Individual Bin (%)	25	%	20	%	22	%	24	%	9	%
Sieve Size	Cum. % Passing	Wt d Cu m. %	Cum. % Passing	Wt d Cu m. %	Cum. % Passing	Wt d Cu m. %	Cum. % Passing	Wt d Cu m. %	Cum. % Passing	Wt d Cu m. %
1"	100	25	100	20	100	22	100	24	100	9
3/4"	100	25	100	20	100	22	100	24	100	9
3/8"	56.4	14.1	70.7	14.1	100	22	100	24	100	9
No.4	10.9	2.7	14.3	2.9	76.4	16.8	99.9	24	99.8	9
No.8	4.7	1.2	6.3	1.3	20.6	4.5	89.8	21.6	98.1	8.8
No.30	3.3	0.8	3.7	0.7	6.2	1.4	40.3	9.7	90.5	8.1
No.50	2.6	0.7	3.3	0.7	4.8	1.1	24.2	5.8	66.9	6
No.200	2.2	0.6	2.7	0.5	3.9	0.9	7.6	1.8	3.7	0.4



When the complex numbers n and k are used to derive the complex modulus, the expressions of A and B in Equation 2.27 become different, whereas C and D remain the same since n and k are not involved.

In the new expressions of A and B , the terms with n_0 and k_0 should be replaced by the corresponding forms in the Laplace domain shown in Equations 2.20 and 2.21; specifically there are two different terms with n_0 and k_0 in A and B that need to be replaced by the

complex numbers, which are $\frac{1}{2} + \frac{k_0 - 1}{n_0 + 2}$ and $\frac{1}{2} + \frac{k_0 - 1}{(n_0 + 1)(n_0 + 2)}$.

Therefore, the term of $\frac{1}{2} + \frac{k_0 - 1}{n_0 + 2}$ is determined shown in Equation A-1 with n and k are

complex numbers.

$$\frac{1}{2} + \frac{k^*(\omega) - 1}{n^*(\omega) + 2} = \frac{1}{2} + (F_1 + iF_2) \quad (\text{A-1})$$

$$\text{where } F_1 = \frac{A_1 A_3 + A_2 A_4}{A_3^2 + A_4^2}, \quad F_2 = \frac{A_1 A_4 - A_2 A_3}{A_3^2 + A_4^2}$$

$$A_1 = (\omega^2 + b_n^2)[\omega^2(k_0 - 1) - b_k^2]$$

$$A_2 = (\omega^2 + b_n^2)b_k k_0 \omega$$

$$A_3 = (\omega^2 + b_k^2)[\omega^2(n_0 + 2) + b_n^2]$$

$$A_4 = (\omega^2 + b_k^2)b_n n_0 \omega$$

Meanwhile, the term of $\frac{1}{2} + \frac{k_0 - 1}{(n_0 + 1)(n_0 + 2)}$ is determined in Equation A-2.

$$\frac{1}{2} + \frac{k^*(\omega) - 1}{[n^*(\omega) + 1][n^*(\omega) + 2]} = \frac{1}{2} + (G_1 + iG_2) \quad (\text{A-2})$$

$$\text{where } G_1 = \frac{A_5 A_7 + A_6 A_8}{A_7^2 + A_8^2}; \quad G_2 = \frac{A_5 A_8 - A_6 A_7}{A_7^2 + A_8^2}$$

$$A_5 = [\omega^2(k_0 - 1) - b_k^2](\omega^2 + b_n^2)^2$$

$$A_6 = b_k k_0 \omega (\omega^2 + b_n^2)^2$$

$$A_7 = (\omega^2 + b_k^2)[(\omega^2(n_0 + 1) + b_n^2)(\omega^2(n_0 + 2) + 2b_n^2) - b_n^2 n_0^2 \omega^2]$$

$$A_8 = b_n n_0 \omega [(\omega^2(n_0 + 1) + b_n^2) + (\omega^2(n_0 + 2) + 2b_n^2)]$$

Therefore, the new expressions of A and B are shown in Equations A-3 and A-4.

$$A = H_1 + iH_2 = [(\frac{1}{2} + F_1)a_0 b_0 + (\frac{1}{2} + G_1)a_d b_d] \omega^2 + [(\frac{1}{2} + F_1)a_0 b_0 b_p b_d + (\frac{1}{2} + G_1)a_d b_d b_p b_d] + i[(F_2 a_0 b_0 + a_2 a_d b_d) \omega^2 + (F_2 a_0 b_0 b_p b_d + G_2 a_d b_d b_p b_d)] \quad (\text{A-3})$$

$$B = J_1 + iJ_2 = [(\frac{1}{2} + F_1)a_0 b_0 (b_p + b_d) + (\frac{1}{2} + G_1)a_d b_d (b_p + b_0)] \omega + i[F_2 a_0 b_0 (b_p + b_d) + a_2 a_d b_d (b_p + b_d)] \omega \quad (\text{A-4})$$

After obtaining the expressions for A and B, Equation 2.27 for the modulus at the bottom is reformulated as follows:

$$E_d^*(\omega) = \frac{(L_1L_3 + L_2L_4) + i(L_2L_3 - L_1L_4)}{L_3^2 + L_4^2} = R_1 + iR_2 \quad (\text{A-5})$$

where $L_1 = CH_1 + DJ_1 - DH_2 + CJ_2$

$$L_2 = CH_2 + DJ_2 + DH_1 - CJ_1$$

$$L_3 = H_1^2 - H_2^2 + J_1^2 - J_2^2$$

$$L_4 = 2(H_1H_2 + J_1J_2)$$

Based on the elastic relation for top and bottom modulus shown in Equation 2.2, the complex modulus at the top is shown as

$$E_0^*(\omega) = k^*(\omega)E_d^*(\omega) \quad (\text{A-6})$$

The complex modulus at the top is determined as

$$E_0^*(\omega) = N_1 + iN_2 \quad (\text{A-7})$$

$$N_1 = \frac{k_0\omega^2}{\omega^2 + b_k^2} \left(\frac{L_1L_3 + L_2L_4}{L_3^2 + L_4^2} \right) + \frac{b_k k_0 \omega}{\omega^2 + b_k^2} \left(\frac{L_2L_3 - L_1L_4}{L_3^2 + L_4^2} \right)$$

$$N_2 = \frac{k_0\omega^2}{\omega^2 + b_k^2} \left(\frac{L_2L_3 - L_1L_4}{L_3^2 + L_4^2} \right) + \frac{b_k k_0 \omega}{\omega^2 + b_k^2} \left(\frac{L_1L_3 + L_2L_4}{L_3^2 + L_4^2} \right)$$

The elastic equation for the center modulus can be derived from Equation 2.1, which is shown as

$$E_c = \left(1 + \frac{k-1}{2^n} \right) E_d \quad (\text{A-8})$$

Thus, the complex modulus at the center is calculated as

$$E_c^*(\omega) = \left(1 + \frac{k^{*(\omega)} - 1}{2^{n^*(\omega)}} \right) E_d^*(\omega) \quad (\text{A-9})$$

Therefore, using the Laplace transforms for n and k in Equations 2.20 and 2.21 and the complex modulus at the bottom in Equation A-5, the complex modulus at the center is determined as

$$E_c^*(\omega) = (M_1R_1 - M_2R_2) + i(M_2R_1 + R_1R_2) \quad (\text{A-10})$$

$$\text{where } M_1 = \frac{2^f (\omega^2 + b_k^2) + p(k_0 \omega^2 - 1) + q(b_k k_0 \omega)}{2^f (\omega^2 + b_k^2)}$$

$$M_2 = \frac{q(k_0 \omega^2 - 1) - p(b_k k_0 \omega)}{2^f (\omega^2 + b_k^2)}$$

$$p = \cos[\ln(2)g]$$

$$q = -\sin[\ln(2)g]$$

$$f = \frac{n_0 \omega^2}{\omega^2 + b_n^2}$$

$$g = \frac{b_n n_0 \omega}{\omega^2 + b_n^2}$$

APPENDIX B

Two time-dependent Poisson's ratios are defined for field core specimens as follows:

$$\nu_0(t) = -\frac{\varepsilon_{01}(t)}{\varepsilon_{02}(t)} \quad (\text{B-1})$$

$$\nu_d(t) = -\frac{\varepsilon_{d1}(t)}{\varepsilon_{d2}(t)} \quad (\text{B-2})$$

where $\nu_0(t)$ and $\nu_d(t)$ are the Poisson's ratios at the top and bottom of a field core specimen, respectively; $\varepsilon_{01}(t)$ and $\varepsilon_{d1}(t)$ are the horizontal strain at the top and bottom respectively, which are negative values in the direct tension test; and $\varepsilon_{02}(t)$ and $\varepsilon_{d2}(t)$ are the vertical strain at the top and bottom, respectively. Since the viscoelastic Poisson's ratio is the material property, the integral form of the Boltzmann superposition principle can be used to calculate the horizontal strain, which is similar with the relationship between the stress, strain and relaxation modulus.

$$\varepsilon_1(t) = -\int_0^t \nu_0(t-\tau) \frac{d\varepsilon_2(\tau)}{d\tau} d\tau \quad (\text{B-3})$$

Take the Laplace transform of both sides of Equation B-3 and then rearrange, which yields

$$\overline{\nu_0}(s) = -\frac{\overline{\varepsilon_1}(s)}{s\overline{\varepsilon_2}(s)} \quad (\text{B-4})$$

where $\overline{\nu_0}(s)$ is the Poisson's ratio of a field core specimen in the Laplace domain, respectively; $\overline{\varepsilon_1}(s)$ is the horizontal strain in the Laplace domain, respectively; and $\overline{\varepsilon_2}(s)$ is the vertical strain in the Laplace domain, respectively.

Similar to the relationship between complex modulus and relaxation modulus, the complex Poisson's ratio can be expressed as:

$$\nu^*(\omega) = i\omega L \{ \nu(t) \}_{s=i\omega} = [s\bar{\nu}(s)]_{s=i\omega} \quad (\text{B-5})$$

$$s\bar{\nu}(s) = -\frac{\bar{\varepsilon}_1(s)}{\bar{\varepsilon}_2(s)} \quad (\text{B-6})$$

A complex Poisson's ratio for a viscoelastic material is usually expressed as:

$$\nu^*(\omega) = \nu' + i\nu'' \quad (\text{B-7})$$

in which $|\nu^*(\omega)| = \sqrt{\nu'^2 + \nu''^2}$

$$\varphi_v = \arctan\left(\frac{\nu''}{\nu'}\right)$$

where ν' is the real or storage component, ν'' is the imaginary or loss component, $|\nu^*(\omega)|$ is the magnitude of the complex Poisson's ratio; and φ_v is the phase angle of the complex Poisson's ratio.

Fit the horizontal and vertical strains measured from the direct tension test using the following two-term functions. Take the strains at the top of the field core specimen as an example.

$$\varepsilon_1(t) = a_1(1 - e^{-b_1 t}) + a_2(1 - e^{-b_2 t}) \quad (\text{B-8})$$

$$\varepsilon_2(t) = a_3(1 - e^{-b_3 t}) + a_4(1 - e^{-b_4 t}) \quad (\text{B-9})$$

$$\bar{\varepsilon}_1(s) = \frac{a_1 b_1 (s + b_2) + a_2 b_2 (s + b_1)}{s(s + b_1)(s + b_2)} \quad (\text{B-10})$$

$$\bar{\varepsilon}_2(s) = \frac{a_3 b_3 (s + b_4) + a_4 b_4 (s + b_3)}{s(s + b_3)(s + b_4)} \quad (\text{B-11})$$

$$\left[s\bar{v}(s) \right]_{s=i\omega} = \left[-\frac{x_1 y_2 y_3 y_4 + x_2 y_1 y_3 y_4}{x_3 y_1 y_2 y_4 + x_4 y_1 y_2 y_3} \right]_{s=i\omega} \quad (\text{B-12})$$

where

$$x_1 = a_1 b_1; \quad x_2 = a_2 b_2; \quad x_3 = a_3 b_3; \quad x_4 = a_4 b_4.$$

$$y_1 = s + b_1; \quad y_2 = s + b_2; \quad y_3 = s + b_3; \quad y_4 = s + b_4.$$

Therefore, the viscoelastic Poisson's ratio is determined as

$$v^*(\omega) = \left[s\bar{v}_0(s) \right]_{s=i\omega} = \left[-\frac{\bar{\varepsilon}_1(s)}{\bar{\varepsilon}_2(s)} \right]_{s=i\omega} = -\frac{PM + QN}{M^2 + N^2} + \left[-\frac{QM - PN}{M^2 + N^2} \right] i \quad (\text{B-13})$$

in which

$$P = -a_2 b_2 \omega^2 (b_1 + b_3 + b_4) + a_2 b_2 (b_1 b_3 b_4) - a_1 b_1 \omega^2 (b_2 + b_3 + b_4) + a_1 b_1 (b_2 b_3 b_4)$$

$$Q = \omega a_2 b_2 (b_1 b_3 + b_1 b_4 + b_3 b_4) + \omega a_1 b_1 (b_2 b_3 + b_2 b_4 + b_3 b_4) - \omega^3 a_1 b_1 - \omega^3 a_2 b_2$$

$$M = -a_4 b_4 \omega^2 (b_1 + b_2 + b_3) + a_4 b_4 (b_1 b_2 b_3) - a_3 b_3 \omega^2 (b_1 + b_2 + b_3) + a_3 b_3 (b_1 b_2 b_4)$$

$$N = \omega a_4 b_4 (b_1 b_2 + b_1 b_3 + b_2 b_3) + \omega a_3 b_3 (b_1 b_2 + b_1 b_4 + b_2 b_4) - \omega^3 a_3 b_3 - \omega^3 a_4 b_4$$

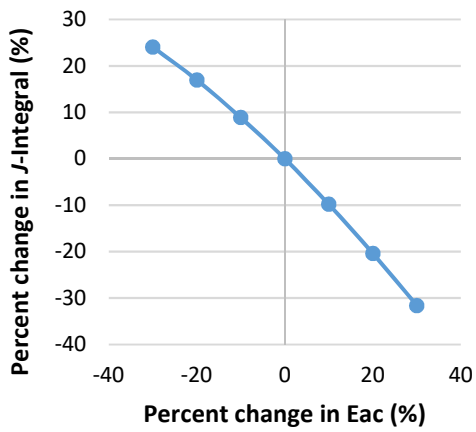
For the strains at the bottom of the specimen, there is another set of a_1, a_2, a_3, a_4 , and $b_1,$

b_2, b_3, b_4 .

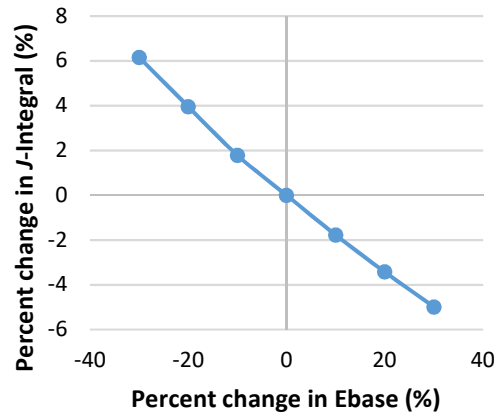
APPENDIX C

Figures C-1 through C-3 are given as the sensitivity analysis results for all the input variables in the dual tire loading case with the tire length of 19 mm, respectively. The crack depth, Moduli of asphalt layer, base layer and subgrade layer (E_a , E_{base} , $E_{subgrade}$), thickness of asphalt layer and base layer (H_a , H_{base}), modulus gradient parameters (n and k) are assumed to be 20 mm, 8000 MPa, 200 MPa, 50 MPa, 200 mm, 150 mm, 3 and 2, respectively. The value of each variable is adjusted from -30% to 30% of the original value. The effect of crack depth on the J -integral is already illustrated and discussed in Chapter 4, therefore, it is not repeated in the Appendix.

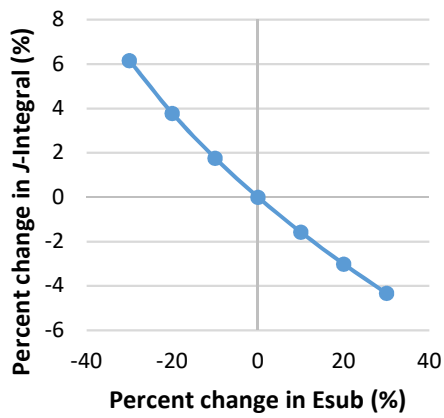
As shown in Figure C-1, the increase of modulus for all the layers of the pavement system decreases the J -Integral value, especially for the asphalt layer, so the increase of modulus helps reduce the propagation speed of the TDC. The moduli of base and subgrade layers seem to have the similar tiny effects on the J -Integral compared to which of the asphalt layer. This is expected since the location of TDC is relatively far from the base and subgrade layers, which is different from the BUC or reflective cracking. As shown from Figure C-2, the thickness of asphalt layer plays the most important role in the propagation of the TDC, the values of the J -Integral are changed from -42% to 92%, if the asphalt layer thickness is adjusted from -30% to 30%. Figure C-3 indicates that the J -Integral is also affected by the shape of the modulus gradient. For a sharper modulus gradient (i.e., a larger n value), the J -Integral is relatively larger. It is also reasonable that the increase of k has the similar effect as the increase of modulus of asphalt layer to decrease the J -integral.



(a)

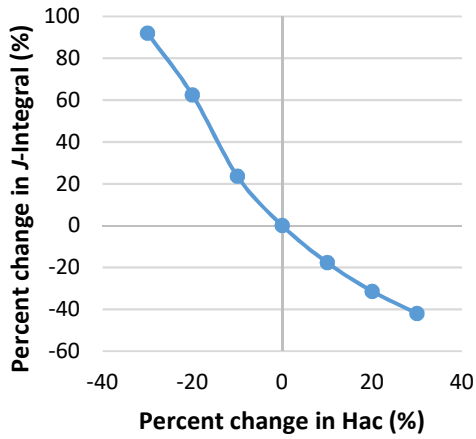


(b)

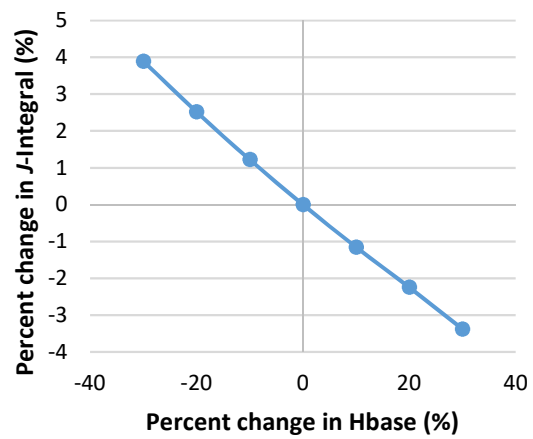


(c)

Figure C-1 Sensitivity Analysis for Moduli of Pavement Layers: (a) Asphalt Layer Modulus, (b) Base Layer Modulus, (c) Subgrade Layer Modulus

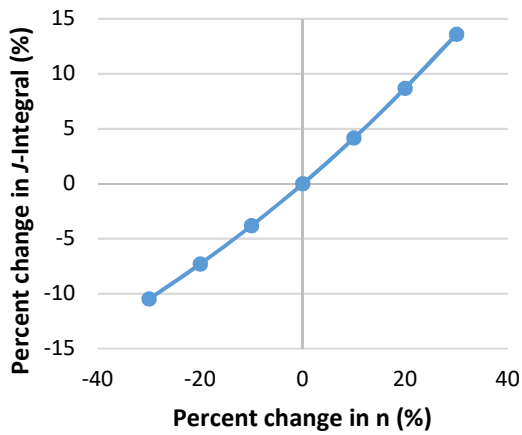


(a)

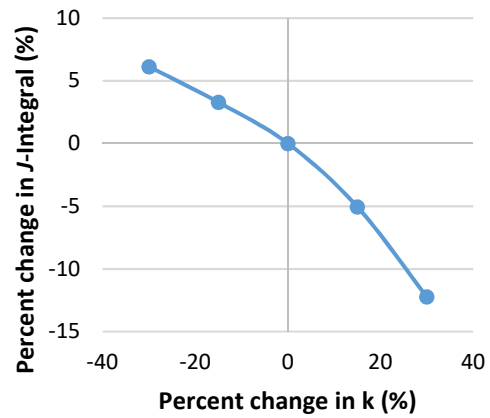


(b)

Figure C-2 Sensitivity Analysis of Thickness of Pavement Layers: (a) Asphalt Layer Thickness, (b) Base Layer Thickness



(a)



(b)

Figure C-3 Sensitivity Analysis of Modulus Gradient Parameters of Asphalt Layer: (a) Value of n, (b) Value of k